

**INTERPRETATION OF METEORIC <sup>10</sup>BE IN MARGINAL ICE-BOUND  
SEDIMENT OF THE GREENLAND ICE SHEET, WEST GREENLAND**

**A Thesis Presented**

**by**

**Joseph Graly**

**to**

**The Faculty of the Graduate College**

**of**

**The University of Vermont**

**In Partial Fulfillment of the Requirements  
for the Degree of Master of Science  
Specializing in Geology**

**January, 2011**

**Accepted by the Faculty of the Graduate College, The University of Vermont, in partial fulfillment of the requirements for the Degree of Master of Science, specializing in Geology.**

**Thesis Examination Committee:**

\_\_\_\_\_ **Advisor**  
**Paul Bierman, Ph.D.**

\_\_\_\_\_ **Tom Neumann, Ph.D.**

\_\_\_\_\_ **Andrea Lini, Ph.D.**

\_\_\_\_\_ **Chairperson**  
**George Pinder, Ph.D.**

\_\_\_\_\_ **Dean, Graduate College**  
**Domenico Grasso, Ph.D.**

**Date: September 1st, 2010**

## Abstract

Isotopic records of glacial ice volume indicate four brief periods during the Pleistocene where global ice volume was smaller than the present minimum, indicating temperatures warmer than present. Constraining the response of Earth's ice sheets to these past warm periods aids the prediction of ice sheet response to future warming. Mathematical models of ice sheet climate response suggest that melting of the Greenland Ice Sheet may have dominated sea level increase during these Pleistocene warming events.

To directly test whether the Greenland Ice Sheet has retreated beyond its present margin, the cosmogenic isotope meteoric  $^{10}\text{Be}$  was measured in ice-bound fine sediment collected from three West Greenland sites. Because meteoric  $^{10}\text{Be}$  is formed in the atmosphere and deposited on the ice sheet during glacial periods, any substantial meteoric  $^{10}\text{Be}$  inventory in ice-bound sediment originates from periods where the western Greenland Ice Sheet was smaller than present. The three sites varied by latitude from  $67^\circ\text{N}$  to  $72.5^\circ\text{N}$ , but are otherwise glaciologically similar. Meteoric  $^{10}\text{Be}$  concentrations between  $2 \cdot 10^6$  and  $2 \cdot 10^8$  atoms/g were found at the northern two sites. Significantly lower concentrations between  $2 \cdot 10^6$  and  $5 \cdot 10^7$  atoms/g were found at the southernmost site.

To understand the significance of these results, previous studies on meteoric  $^{10}\text{Be}$ 's distribution in soil were exhaustively compiled. The compilation demonstrates that meteoric  $^{10}\text{Be}$  is consistently retained in soil and that its distribution is unique and not exclusively controlled by any one soil property. This compilation also shows that meteoric  $^{10}\text{Be}$  distribution with depth is sufficiently consistent to allow for the modelling of its long-term evolution and the prediction of the total inventory of meteoric  $^{10}\text{Be}$  in a soil profile from the soil's maximum meteoric  $^{10}\text{Be}$  concentration.

To translate inferred soil meteoric  $^{10}\text{Be}$  inventories into soil ages, short and long-term meteoric  $^{10}\text{Be}$  deposition rates were likewise compiled from the literature. This study finds that while short term meteoric  $^{10}\text{Be}$  deposition rates are generally predictable by latitude and precipitation, changes in geomagnetic field, dust flux, and climate may cause long-term meteoric  $^{10}\text{Be}$  deposition rates to vary. Warm period meteoric  $^{10}\text{Be}$  deposition rates for Greenland are best predicted from mid-Holocene values.

Based on the compiled meteoric  $^{10}\text{Be}$  depth distribution data and the global ice volume record, a forward model of meteoric  $^{10}\text{Be}$  evolution under the Greenland Ice Sheet is constructed. This model shows that the high meteoric  $^{10}\text{Be}$  concentrations found at the northern two sites are best explained by the slow erosion of pre-glacial regolith. The meteoric  $^{10}\text{Be}$  concentrations at the southern site likely formed during Pleistocene interglacial periods, and indicate that the Southern Greenland Ice Sheet leads global ice volume in warm period retreat.

## Citations

Material from this thesis was submitted for publication to *Geochimica et Cosmochimica Acta* on April 9th, 2010 in the following form:

Graly, J.A., Bierman, P.R., Reusser, L.J., and Pavich, M.J.. Submitted, Meteoric  $^{10}\text{Be}$  in soil profiles – a global meta-analysis: *Geochimica et Cosmochimica Acta*.

Material from this thesis was submitted for publication to *Earth and Planetary Science Letters* on May 25th, 2010 in the following form:

Graly, J.A., Reusser, L.J., and Bierman, P.R.. Submitted, Making global and temporal sense of meteoric  $^{10}\text{Be}$  deposition rates: *Earth and Planetary Science Letters*.

Material from this thesis will be submitted for publication to *Nature* in the following form:

Graly, J.A., Corbett, L., Bierman, P.R., Neumann, T., and Rood, D., Lini, A.. Submitted, Meteoric  $^{10}\text{Be}$  evidence for past interglacial ice sheet retreat in western Greenland: *Nature*

## Table of Contents

Citations.....	ii
<b>Chapter 1: Introduction</b> .....	1
<b>Chapter 2: Background</b> .....	5
1. Past Interglacial Exposure .....	5
2. Glacial Erosion Rates .....	8
3. Sub-Glacial Sediment Entrainment .....	12
4. Basal sediment transport velocity.....	16
<b>Chapter 3: Meteoric <sup>10</sup>Be in soil profiles – a global meta-analysis</b> .....	19
1. INTRODUCTION.....	20
2. METHODS .....	22
3. RESULTS AND DISCUSSION .....	24
4. CONCLUSIONS AND IMPLICATIONS .....	41
<b>Chapter 3 Tables</b> .....	45
<b>Chapter 3 Figures</b> .....	48
<b>Chapter 4: Making global and temporal sense of meteoric <sup>10</sup>Be deposition rates</b> ....	60
1. INTRODUCTION.....	61
2. SHORT-TERM METEORIC <sup>10</sup> BE DELIVERY.....	64
3. LONG-TERM VARIATION IN METEORIC <sup>10</sup> BE DEPOSITION .....	71
4. LONG-TERM METEORIC <sup>10</sup> BE DEPOSITION RATES FROM TERRESTRIAL SOILS .....	77
5. CONCLUSIONS .....	82
<b>Chapter 4 Tables</b> .....	85
<b>Chapter 4 Figures</b> .....	86
<b>Chapter 5: Meteoric <sup>10</sup>Be evidence for past interglacial ice sheet retreat in western Greenland</b> .....	94
<b>Chapter 5 Figures</b> .....	101
<b>Chapter 6: Supplement from Meteoric <sup>10</sup>Be evidence for past interglacial ice sheet retreat in western Greenland</b> .....	105
<b>Supplement A: Accelerator Mass Spectrometry Measurements</b> .....	105
<b>Supplement B: Stable Isotope Results</b> .....	106
<b>Supplement C: Sediment Transport Model</b> .....	109
<b>Supplement D: Erosion/Exposure Model</b> .....	110
<b>Chapter 6 Tables</b> .....	113
<b>Chapter 6 Figures</b> .....	117
<b>Chapter 7: Conclusions</b> .....	122
<b>Cited References</b> .....	125

## Chapter 1: Introduction

Over recent decades, it has become apparent that human production of CO<sub>2</sub> and other greenhouse gasses is increasing global temperature on earth, and is likely to continue to do so (Solomon et al., 2007). However, the precise magnitude of this coming increase is still poorly constrained, in large part because there is no paleoclimatic analogy for a sudden doubling of atmospheric carbon (Hansen, 2005). Of the adverse effects of global warming, the melting of continental ice sheets and the consequent sea level rise have the potential to wreak significant havoc on human civilization (Solomon et al., 2007). Consequently, an understanding of the sensitivity of continental ice sheets to temperature changes will allow improved projections of coming environmental changes and therefore enable humanity to better prepare for them.

The rate at which ice sheets respond to temperature shifts has been a topic of considerable debate, with new evidence of fast flow regimes (such as surging outlet glaciers) challenging the traditional conception that significant change in mass balance would occur over thousands of years (e.g. Alley et al., 2005). The overall magnitude of expected glacial mass balance changes remains uncertain, as it depends on the magnitude of changes in atmospheric greenhouse gasses and the sensitivity of global temperature to those changes, as well as the sensitivity of continental ice masses to temperature and attendant precipitation change. Most research into past and future ice sheet volume is based on mathematical models that parameterize ice physics and present ice sheet conditions (Huybrechts, 2006). Such mathematical models use the ice core paleoclimate record to reconstruct past ice sheet conditions (e.g. Lhomme et al., 2005) or use

temperature projections to model possible future climate scenarios (e.g. Alley et al., 2005).

Various workers (e.g. Håkansson et al., 2007) are attempting to reconcile model results with moraine positions and exposure age estimates in Greenland and Antarctica to assess the extent of the ice sheets during the last glacial maximum. However, there have been few empirical studies directly examining ice extent during interglacial periods. As ice sheet behavior during warm periods is most crucial for predicting change in ice sheet mass balance from anthropogenic warming, empirical data constraining past interglacial period ice sheet extent is timely and important.

This thesis is part of the Greenland Cosmochronology Project, a broader study aimed at quantifying the Greenland Ice Sheet's response during past periods where Earth had warmer temperatures than present through the measurement of cosmogenic isotopes in glacial detrital material presently emerging from ice. The term *cosmogenic* refers to the generation of particles by the collision of high-energy galactic cosmic rays with Earth materials. Several of these particles are uniquely or predominately generated by this pathway and therefore trace processes occurring near the Earth's surface (Bierman, 1994). Such isotopes typically come in two species: a meteoric species generated from the interaction of galactic cosmic rays with Earth's atmosphere and their subsequent deposition on Earth's surface in precipitation systems; and an *in situ* species generated from the direct interaction of galactic cosmic rays with Earth materials. Because meteoric cosmogenic isotopes would be deposited on the surface of the Greenland Ice Sheet, and the ice is thick enough that cosmic rays cannot penetrate it, any substantial

cosmogenic isotope inventory in Greenland's glacial detrital material must have formed during periods when the extent of the Greenland Ice Sheet was smaller than it is presently.

A Greenland Cosmochronology Project team consisting of two UVM faculty (Bierman and Neumann – now at NASA), two masters students (Corbett and myself), and a collaborator from Lawrence Livermore National Laboratory (Finkel) traveled to western Greenland in the summer of 2008. To test whether results varied by latitude, three sites were visited: Kangerlussuaq (67.1° N), Ilulissat (69.4 ° N), and Upernavik (72.6° N). At each of the three sites, ~100 cobble-sized detrital clasts were collected, along with 10 to 20 sediment-rich ice samples. Minerals within the rock clasts potentially contain *in situ* cosmogenic isotopes, while the fine sediment in ice may have absorbed or incorporated meteoric cosmogenic isotopes.

The Greenland Cosmochronology Project has thus far focused on the cosmogenic radionuclide  $^{10}\text{Be}$ , measuring *in situ*  $^{10}\text{Be}$  in the clasts and meteoric  $^{10}\text{Be}$  in the ice-bound sediment.  $^{10}\text{Be}$  was chosen because Be chemistry allows for its long-term retention in rock and sediment,  $^{10}\text{Be}$ 's half-life of 1.39 My (Korshinek et al., 2010) is long enough to trace glacial processes over the entire Quaternary, and analytic techniques allow  $^{10}\text{Be}$  to be measured efficiently and precisely.

This thesis focuses on the meteoric  $^{10}\text{Be}$  measurements in the ice-bound fine sediment. (Corbett's thesis will focus on the *in situ* measurements.) The Greenland Cosmochronology Project is the first team to ever make measurements of meteoric  $^{10}\text{Be}$  in ice-bound sediment. A new framework for interpreting the significance of meteoric  $^{10}\text{Be}$  was therefore necessary. To better understand the isotope's behavior in soil, depth

distribution data from every meteoric  $^{10}\text{Be}$  soil profile in the published literature was compiled and analyzed as a group. The paper resulting from this analysis is Chapter 3 of this thesis. The long-term deposition rate of meteoric  $^{10}\text{Be}$  is also a subject of scientific debate and uncertainty. An meta-analysis of meteoric  $^{10}\text{Be}$  deposition rate data from precipitation and long-term ice and sediment records is presented in Chapter 4 of this thesis.

Given the detailed review of all aspects of the meteoric  $^{10}\text{Be}$  literature presented in Chapters 3 and 4, the background section (Chapter 2) does not discuss cosmogenic isotopes. It instead reviews the existing literature on past Greenland Ice Sheet extent, ice sheet erosivity, entrainment of sediment into basal ice, and basal ice velocity. The extensive glaciological and geochemical framework developed in Chapters 2-4 allows for the presentation and interpretation of the West Greenland meteoric  $^{10}\text{Be}$  data in chapters 5 and 6. Because these chapters were submitted as a letter to *Nature*, Chapter 5 is a concise summary of principle evidence and conclusions, while Chapter 6 provides supporting analytic and methodological details.

## Chapter 2: Background

### 1. Past Interglacial Exposure

The long-term record that best traces past variation in Earth's ice masses is the ratio of  $^{18}\text{O}$  to  $^{16}\text{O}$  in marine sediments. Because the lighter  $^{16}\text{O}$  is more likely to be evaporated and subsequently precipitated into glacial ice, the  $\delta^{18}\text{O}$  ‰ of ocean water is enriched during periods of greater global ice volume. The isotopic composition of ocean water will largely control the isotope ratios of benthic carbonate. A global ice volume record can therefore be constructed from benthic carbonate cores, providing a robust estimate of long-term global ice volume conditions (Lisiecki and Raymo, 2005). Benthic carbonate  $\delta^{18}\text{O}$  records have been collected from diverse parts of Earth's oceans, and the comparison of multiple records as a globally-averaged stack permits the construction of a single  $\delta^{18}\text{O}$  record that averages out local variation (Lisiecki and Raymo, 2005). Such records have been extended over 5 million years into the past, covering the entire period of major Northern Hemisphere glaciation.

The benthic  $\delta^{18}\text{O}$  record shows global ice volume first exceeding modern volumes for a substantial length of time  $\sim 2.7$  Ma before present, corresponding with the major onset of Northern Hemisphere glaciation (Bitanjan and van de Wal, 2008). From the period between 2.7 and 2.1 Ma before present, glaciation was relatively frequently interrupted, with 14% of the period exhibiting lower global ice volumes than present. After 2.1 Ma before present, greater than modern global ice volumes are only briefly and infrequently interrupted. These interruptions occur during oxygen isotope stage (OIS) 31,

1072-1066 ka before present, OIS 11, 410-399 ka before present, OIS 9, 329-323 ka before present and OIS 5, 125-118 ka before present (Bitanja and van de Wal, 2008).

Of these, OIS-5, also known as the Eemian interglacial, has received the most study. Biologic paleoclimate evidence robustly demonstrates substantial Eemian Northern Hemisphere warming, with pollen in Northern Europe showing plant assemblages indicative of conditions several degrees warmer than present (Aalbersberg and Litt, 1998). In southern Greenland, plant macrofossils also show biotic assemblages indicative of 5 degrees warmer than today (Bennike and Bocher, 1994).

Less evidence has been collected for earlier interglacial periods. Cosmogenic  $^{10}\text{Be}/^{26}\text{Al}$  data taken from a rock core beneath the GISP2 ice core shows burial ages of  $0.5 \pm 0.2$  million years (Nishiizumi et al., 1996). As the GISP2 core was taken at Summit Station on the ice divide in central Greenland, this would indicate a total or near-total melt of the Greenland Ice Sheet consistent with OIS-11. However, a shifting ice divide may allow for some portion of the Greenland Ice Sheet to have remained (Marshall and Cuffey, 2000).

Modelling efforts have focused on OIS-5 ice sheet geometry reconstruction; as this is the last interglacial period, it is easiest to reconstruct from present conditions and ice core records. The earliest efforts at modelling this period show some reduction, though not complete melting, in the Greenland Ice Sheet's Southern Dome, consistent with 1-2 meters of sea level increase (Letreguilly et al., 1991). As sedimentary records indicate an Eemian sea-level highstand of at least 5-6 meters (Vezina et al., 1999), this result implies that substantial melting would have had to occur in the southern

hemisphere to make up the difference. These early models were working with only the Dye-3 and Camp Century Greenland ice core records and made the crucial error of assuming that  $\delta^{18}\text{O}$  variation in the ice core corresponds with temperature variation analogously with present conditions. Cuffey et al. (1995) used temperature measurements from the GISP2 borehole to calibrate the relationship between  $\delta^{18}\text{O}$  and temperature through the last glacial cycle. Once these corrections are made, models show a much-reduced Greenland Ice Sheet, lacking most to all of the Southern Dome and substantial retreat from the northern margin (Cuffey and Marshall, 2000), contributing as much as 5.5 meters to sea level rise (Huybrechts, 2002).

However, substantial controversies still exist about how to best model the Greenland Ice Sheet during the Eemian period. Cuffey et al.'s borehole temperature method does not decisively determine the  $\delta^{18}\text{O}$  / temperature sensitivity for the Eemian period, as geothermal heat flux has affected borehole temperatures in Eemian ice (Cuffey and Clow, 1997; 1995). Most models assume a uniform geothermal gradient beneath Greenland, which is certainly not the case (Braun et al., 2007; Greve, 2005). Modelling efforts that include geothermal gradient variability result in a somewhat larger Eemian ice sheet (Tarasov and Peltier, 2003). The pressure of the gas trapped in Eemian ice indicates substantial ice thickness at Summit during Eemian time (Raynaud et al., 1997). This along with other ice stratigraphic considerations from the NGRIP and Camp Century cores led Lhomme et al. (2005) to model only minor retreat from the Greenland Ice Sheet's northern margin during Eemian time, though they still model a complete melt of the Southern Dome. Given the uncertainties in temperature reconstruction methods,

Otto-Bliesner et al. (2006) instead base their temperature reconstructions (as well as precipitation-driven mass balance changes) on the Community Climate System Model. Their ice model shows little retreat in the Main Dome of the Greenland Ice Sheet, and substantial but not complete melting of the southern dome, producing only 3.4 m of sea level rise.

Table 1. Modeled distance of Eemian Greenland Ice Sheet retreat

Location	Flowline Length (km)	Modeled Eemian Flowline Retreat (km)					Otto-Bleisner
		Lhomme	Tarasov	Cuffey	Huybrechts		
Upernavik 73.6°N	337	95	41.5	129	41.5	20	
Ilulissat 69.4°N	545	120	111	267	458	0	
Kangerlussuaq 67.1°N	340	340	340	340	340	192	

Despite the substantial differences in model results, these models uniformly predict substantially more response to warming in the Southern Greenland Ice Sheet than in northern Main Dome. However, it is unclear whether this difference can be detected through the measurement of cosmogenic isotopes in detrital sediment. Because retreat is still modelled at the higher latitude sites (Table 1), rock and sediment sourced from areas near the present ice margin would still develop cosmogenic isotope inventories during even minor retreats. Furthermore, differences in cosmogenic isotope inventories can arise from causes other than exposure length. Erosion rate differences, if substantial, are particularly significant.

## 2. Glacial Erosion Rates

The erosion rates under the Greenland Ice Sheet during Pleistocene and Holocene times cannot be directly observed or calculated. Pleistocene erosion rates of then

glaciated areas have been estimated by measuring offshore sediment volumes and back calculating the thickness of sediment eroded over a constrained period of time. Erosion rates can also be estimated by analyzing cosmogenic isotope inventories in exposed glacial surfaces. If the measured concentration of cosmogenic isotopes exceeds a post-glacial exposure time, then inheritance of isotopes from a previous interglacial period can be inferred. These inheritance concentrations, together with the length of glacial periods can be used to estimate erosion rate.

Estimates of modern glacial erosion rates vary globally from  $\sim 10$  m/Ma to greater than 10,000 m/Ma, with the highest values found in tectonically-active alpine glaciers (Hallet et al., 1996). Andrews and others (1994) estimate Holocene erosion in East Greenland to be between 10 and 40 m/Ma based on the sediment volumes in three fjords. Similar comparatively low erosion rates are inferred from the offshore sediments of the cold-based glaciers of Svalbard, while the polythermal glaciers of Svalbard show rates an order of magnitude larger (Eleverhøi et al., 1998).

Offshore sediments have also been used to measure the Quaternary erosion rates of former continental ice sheets. Atlantic sediment volumes suggest that at least 120-200 meters were stripped off the Laurentide ice sheet during the past 3 million years (Bell and Laine, 1985; Laine, 1980), suggesting an erosion rate of  $\sim 50-90$  m/Ma (when chemical erosion is also considered). However, these authors do not distinguish between glacier and fluvial processes in their estimates and may have overestimated the Laurentide contribution to Gulf of Mexico sediments (Hay et al., 1989). These estimates provide an average for large continental regions and are unlikely to represent uniform erosion over

those regions. The deep offshore troughs in the Atlantic Ocean suggest areas of greater than 300 meters of erosion in glacial distributary tongues (White, 1988). Kaszycki and Shilts (1987) estimate under 10 meters of Quaternary erosion in the craton of the Canadian Shield. They also suggest that most large scale erosion happened during the early stages of the quaternary, where soils and unlithified sediments could be easily stripped. While continental-scale, sediment-based estimates of erosion of Greenland have not been performed, quaternary sediments off the east coast of Greenland average around 100 meters depth, suggesting erosion volumes of 10s of meters for the period of the Quaternary (Vogt et al., 1981).

Glasser and Hall (1997) combine offshore sediment studies with onshore geomorphic reconstruction to conclude that Quaternary glacial erosion rates were highly variable across a transect in northeast Scotland, with estimates of total quaternary erosion varying between 10 and 150 meters depending on the landform in question (glacial fluvial deepening of valleys is not considered). The authors also found a sharp increase in erosion rates inferred from sediment volumes in the middle Quaternary, when the British Ice Sheet expanded to its greatest extent. During this peak erosive episode, rates increased to 130 m/Ma from their Quaternary average of 85 m/Ma. This mid-quaternary spike is also found by Dowdeswell and others (2010) in sediment off Norway, spiking to 430 m/My with an average of 190 m/My.

Studies of glacial erosion rates using cosmogenic methods have often found erosion rates lower than those estimated from offshore sediments. Erosion rates calculated from cosmogenic isotope concentrations can be uncertain as the method is

dependent on assumptions regarding burial duration, pre-burial exposure age, and post-burial exposure duration, though burial duration can be constrained through the use of multiple cosmogenic isotopes (Bierman, 1994). Many of these studies focus on bedrock tors and other erosion resistant features of the landscape. Bierman and others (1999) found that in upland areas of Baffin Island and southeastern Minnesota, the erosion rate on Baffin Island did not exceed 1.1 m/My and was negligible in Minnesota. Significant inheritance and complex exposure/burial histories of up to a million years are found at similar latitudes in northern Finland and Sweden (Darmondy et al., 2008; Fabel et al., 2002), indicating that relict surfaces and erosion-resistant tors experienced little to no erosion in portions of the northern Fennoscandian ice sheet. Studies of tors in Scotland have also found evidence that these features resisted erosion for several glacial cycles and eroded at rates of less than 10 m/My (Phillips et al., 2006).

Some studies of erosion-resistant bedrock surfaces found higher rates of glacial erosion. Briner and Swanson (1998) find erosion rates of up to 350 m/My in the Puget Sound region, but such high rates are calculated by assuming the surface was eroded exclusively during a three-thousand year readvance of the Cordilleran ice sheet. This assumption is not tested through multiple cosmogenic isotopes. Rates between 10 and 250 m/My are found in central Wisconsin, assuming a 10,000 year period of erosion by the ice sheet (Colgan et al., 2002).

The cosmogenic isotope evidence for extremely low rates of erosion in glacial uplands does not necessarily imply uniformly low rates of erosion. Briner and others (2006) contrast the weathering and inheritance in the uplands, fjords, and transitional

zones of Baffin Island and find significantly less inheritance in the freshly eroded fjords. However, they still find inheritance in a few of the samples, indicating the erosion may have not been more than a couple of meters since the previous interglacial period. Studies of outlet fjord terrains in northern Sweden similarly find that a few samples have inherited cosmogenic nuclides (Stroeven et al., 2002). The authors here argue that this also implies relatively low erosion rates even in the ice stream/outlet fjord regions of the northern Fennoscandian ice sheet.

Though the Quaternary erosion rates of Greenland have not been calculated with any certainty, review of the estimates of quaternary erosion rates at similar latitudes calculated by different methods suggests that the rate is likely lower than 100 m/My and may be closer to 10 m/My. While the erosion rates on the order of 1 m/My and below found in some upland areas of former ice sheets may be correct for similar areas under the Greenland Ice Sheet, the volume of sediment produced from such surfaces is so low that the majority of detrital sediment samples are likely sourced from areas of higher erosion.

### **3. Sub-Glacial Sediment Entrainment**

Processes of sub-glacial sediment entrainment are fundamentally different where ice is flowing over a bedrock surface and where sediment is present between the ice and the bedrock. Hard-bedded glaciers primarily erode the bedrock beneath through quarrying, abrasion, and chemical dissolution (Drewry, 1986). Quarrying processes are likely the source of the cobble-sized ice-bound clasts sampled by the Greenland Cosmochronology Project. Quarrying processes must occur prior to abrasion processes,

as entrained rock material is the primary abrader of the glacial bed (Drewry, 1986).

Abrasion can potentially produce sand and silt-sized material as glacially entrained sediment. Due to its source from rock, such material would not contain meteoric  $^{10}\text{Be}$ .

Quarrying, or plucking, is the process by which the stress applied to ledges on a rough bed causes micro-fractures to expand in the rock, ultimately causing rock to break off and the ledge to propagate up glacier (Hallet, 1996). The rate of crack growth depends on rock material properties, basal sliding velocity, and basal effective pressure (Hallet, 1996). Quarrying is most effective in cases of fast basal sliding and low basal effective pressures, which induce extensive bed-ice separation and high stresses where the ice contacts the bed (Hallet, 1996). Fluctuations in water pressure are also significant, particularly as decreasing water pressure in cavities beneath the bed increases stress on the stoss surface and decreases stress on the lee surface of a bedrock irregularity (Iverson, 1991). Empirical studies beneath alpine glaciers suggest that fluctuation in water pressure may be the primary control on rock crack growth rate (Cohen et al., 2006).

In the case where a glacier flows over sediment (be it regolith or till), regelation is the dominate mechanism for sediment entrainment. Though sediment entrainment by regelation is classically conceived as occurring through the pressure melting of ice on the stoss side of an asperity or bump in a hard glacial bed and the re-freezing of this water on lee side (Weertman, 1957), hard-bed regelation processes can only produce regelation layers millimeters to centimeters thick (Lliboutry, 1993) and are not effective in entraining large quantities of debris (Hubbard and Sharp, 1993). However, regelation also occurs as ice melts and refreezes around individual sediment grains. Such small-

scale regelation is a major mechanism by which sediment is entrained in soft-bedded glaciers (Iverson and Semmens, 1995). Though pressure-melting induced regelation occurs only at ice temperatures greater than  $-4^{\circ}\text{C}$  (Iverson, 1993), basal sediment entrainment has been observed at temperatures as low as  $-17^{\circ}\text{C}$  (Cuffey et al., 2000). This is attributed to the formation of an interfacial film of water between the ice crystals and the sediment grains, which has been observed in laboratory settings to temperatures as low as  $-30^{\circ}\text{C}$  (Cuffey et al., 2000). This regelation process will often result in a multi-meter fringe of partial ice penetration into the sediment below, which effectively entrains a layer of debris (Rempel, 2008). The thickness of this fringe and the rate at which it expands or contracts are dependent on ice temperature (including basal heat flux), effective stress, and glacial sliding speed, such that as the driving stress increases, fringe growth slows (Rempel, 2008). Under sufficient driving stress, the basal ice layer of a glacier may contract, resulting in the deposition of entrained sediment (Rempel, 2008).

In the ablation zone of ice sheets, several processes resulting from the interactions of surface meltwater with basal material can affect the entrainment of sediment in ice. The process with the largest capacity to move basal material is fluvial transport by subglacial streams (Alley et al., 1997). Discharge in subglacial streams is often so large, that sediment availability (not discharge) is the limiting factor controlling sediment transport volumes (Alley et al., 1997). In soft-bedded glaciers, small discharge volumes can flow through till, but as discharge increases, the discharge is organized into channels that cut through the ice and canals that cut into the subglacial till (Ng, 2000; Walder and Fowler, 1994). This allows for erosion along these branching channels where subglacial

till is thick, and deposition in esker deposits over areas where the glacier is sliding over bedrock (Walder and Fowler, 1994).

Apart from sediment transport by subglacial streams, the basal freeze-on of supercooled water could be a significant basal debris entrainment process (Alley et al., 1998). Water, typically surface meltwater drained through crevasses, can become supercooled and freeze on to the base of a glacier when it flows into an overdeepening. Overdeepenings are adversely sloped to the downward slope of the glacier and need to be 50% percent steeper than the glacier slope to be effective at supercooling water (Alley et al., 1998). This process has the ability to entrain large quantities of basal sediment, as supercooled waters can freeze large layers of debris in single events (Lawson et al., 1998). Alley and others (2003) have suggested that the typical shape of these overdeepenings represents the equivalent of the long profile in a glacier or ice sheet flowline in that subglacial streams will erode sediment or bedrock to create overdeepenings of this typical slope and overly steep overdeepenings will clog stream flow paths causing sediment deposition. On this view, glaciohydraulic supercooling is a major geological process responsible for a significant portion of erosion by glaciers. Thus, many of the glacial features in the sedimentary record can possibly be attributed to this process (Larson et al., 2006). Some authors have contested this “grand theory of everything” approach to glaciohydraulic supercooling, contending that evidence for the pervasiveness of the processes is overstated (Cook et al., 2006; Knight and Cook, 2008). As active glaciohydraulic supercooling increases the erosion rate and the quantity of sediment

entrained in the ablation zone near the glacial margin, the outcome of this debate will affect understanding of glacial sediment transport processes.

Sediment can also be moved by glaciers without entrainment in basal ice, through the deformation of subglacial till and by “particle plowing”. The extent to which till deformation acts as a major process and the debris fluxes it produces are debated issues in the scientific literature, with till deformation possibly being significant in areas of fast glacial flow (i.e. ice streams) (Alley et al., 1997). Cuffey and Alley (1996) suggest that the dynamics of such till deformation may be similar to fault gouge processes. Tulaczyk and others (2001) suggest that plowing of rough elements in an irregular soft-bed may be the dominant mechanism of subglacial till deformation in Antarctic ice streams. Similar particle ploughing (where individual clasts are pushed by ice through a till substrate) has been observed under laboratory conditions (Thomson and Iverson, 2008). Greenland Cosmochronology Project samples of sediment entrained in ice and outwash are unlikely to have been recently transported through subglacial sediment deformation.

#### **4. Basal sediment transport velocity**

The speed at which entrained glacial sediment is transported to the ice sheet margin can be estimated from ice sheet geometry and geophysical data. Radio-echo sounding transects of ice sheets detect layered internal variations in ice density or composition that correspond to former ice sheet surfaces subsequently deformed by glacial flow (Harrison, 1973). Where these layers are traced to ice cores, the ice stratigraphy of the core provides an age for the deformed former ice sheet surface (e.g.

Fahnestock et al., 2001). Such dated layers, along with ice sheet geometry data (Bamber et al., 2001), can be used to calibrate models of the velocity of glacial ice flow (Wang et al., 2002).

Modeled ice velocities for a flowline terminating within 5 km of the Ilulissat site (69.4° N) were published by Wang and others (2002). Wang's model was constructed using directly measured surface velocity (Hoffmann, 1975), accumulation (Bensen, 1962), and temperature (Mock and Weeks, 1966) data, which was matched with the radio-echo sounding (Fahnestock et al., 2001) and ice sheet geometry data (Bamber et al., 2001). The model assumes enhanced flow of anisotropic ice when ice crystals are aligned with primary stress directions (Wang and Warner, 1999). These equations governing this flow have been determined experimentally in laboratory settings (Li et al., 1996), and tested against an isotropic ice composition assumption in matching modelled and observed radio-echo sounding layers (Wang et al., 2002).

As Wang's team at NASA has a constructed a complete model of the glacial flow of the Greenland Ice Sheet, she provided the Greenland Cosmochronology Project with flowline velocity models for the Kangerlussuaq (67.1° N) and Upernavik (73.6° N), in addition to the published flowline near Ilulissat. While this model can predict basal ice flow velocities very precisely, the uncertainties in its application to basal sediment transport are unclear. Particularly, there is no control on the extent to which basal sediment may move slower or faster than the ice sheet bottom as a whole. Processes such as particle plowing may act intermittently and regelation entrained sediment case fall out of the basal layer due to obstruction in the glacier bed or retraction of the freezing front.

Sediment transport of subglacial streams is likely orders of magnitude faster than transport by ice. But as such variability in sub-glacial processes cannot be quantified, Wang's basal ice velocities are used to approximate the transport of ice-bound sediment.

**Chapter 3: Meteoric  $^{10}\text{Be}$  in soil profiles – a global meta-analysis**  
(submitted as a separate paper to *Geochimica et Cosmochimica Acta*)

**ABSTRACT**

In order to assess current understanding of meteoric  $^{10}\text{Be}$  dynamics and distribution in terrestrial soils, we assembled a database of all published meteoric  $^{10}\text{Be}$  soil depth profiles, including 104 profiles from 27 studies in globally diverse locations, collectively containing 679 individual measurements. This allows for the systematic comparison of meteoric  $^{10}\text{Be}$  concentration to other soil characteristics and comparison of profile depth distributions between geologic settings. Percent clay,  $^9\text{Be}$ , and dithionite-citrate extracted Al positively correlate to meteoric  $^{10}\text{Be}$  in more than half of the soils where they were measured, but the lack of significant correlation in other soils suggests that no one soil factor controls meteoric  $^{10}\text{Be}$  distribution with depth. Dithionite-citrate extracted Fe and cation exchange capacity are only weakly correlated to meteoric  $^{10}\text{Be}$ . Percent organic carbon and pH are not significantly related to meteoric  $^{10}\text{Be}$  concentration when all data are compiled.

The compilation shows that meteoric  $^{10}\text{Be}$  concentration is seldom uniform with depth in a soil profile. In young or rapidly eroding soils, maximum meteoric  $^{10}\text{Be}$  concentrations are typically found in the uppermost 20 cm. In older, more slowly eroding soils, the highest meteoric  $^{10}\text{Be}$  concentrations are found at depth, usually between 50 and 200 cm. We find that the highest measured meteoric  $^{10}\text{Be}$  concentration in a soil profile is an important metric, as both the value and the depth of the maximum meteoric  $^{10}\text{Be}$  concentration correlate with the total measured meteoric  $^{10}\text{Be}$  inventory of the soil profile.

In order to refine the use of meteoric  $^{10}\text{Be}$  as an estimator of soil erosion rate, we compare near-surface meteoric  $^{10}\text{Be}$  concentrations to total meteoric  $^{10}\text{Be}$  soil inventories. These trends are used to calibrate models of meteoric  $^{10}\text{Be}$  loss by soil erosion. Erosion rates calculated using this method vary based on the assumed depth and timing of erosional events and on the reference data selected.

## 1. INTRODUCTION

Since the development of accelerator mass spectrometers more than thirty years ago, the meteoric  $^{10}\text{Be}$  content of soil profiles has been used to study soil histories (Elmore and Phillips, 1987; Klein et al., 1982). The total meteoric  $^{10}\text{Be}$  inventory of a soil profile has been used to constrain soil age (Pavich et al., 1986) or, alternatively, isotope residence time (Monaghan et al., 1983). Meteoric  $^{10}\text{Be}$  is also used to quantify erosion rates and trace hillslope processes (e.g. McKean et al., 1993) as well as estimate rates of soil transport (Jungers et al., 2009). Deposition of meteoric  $^{10}\text{Be}$  in ice (e.g. Finkel and Nishiizumi, 1997) and sediment archives (e.g. Frank et al., 1997) can provide dated records of variability in atmospheric  $^{10}\text{Be}$  production over time. The isotope has also been used to trace several other earth system processes (McHargue and Damon, 1991; Willenbring and von Blanckenburg, 2010).

Meteoritic  $^{10}\text{Be}$  is a cosmogenic radionuclide formed mainly by the spallation of oxygen or nitrogen in the atmosphere (Lal and Peters, 1967). The isotope has a half-life of 1.39 million years (Korschinek et al., 2010) and therefore is a potential tracer of processes operating over time scales of up to  $10^7$  years. This distinguishes the isotope

from a suite of other radioactive tracers, which either due to their short half-lives or anthropogenic source only trace recent Earth system events (e.g. Walling and He, 1999).  $^{10}\text{Be}$  formed in the atmosphere adheres to aerosols and is typically delivered to Earth's surface in rainfall (McHargue and Damon, 1991). Once on Earth's surface, this "meteoric"  $^{10}\text{Be}$  has a strong propensity to adhere to soils, with a partition coefficient of  $\sim 10^5$  (mL/g) at pH 6 and above (You et al., 1989). Sedimentary systems can therefore record both the long-term deposition of meteoric  $^{10}\text{Be}$  and the subsequent fate of the isotope due to chemical leaching, illuviation, erosion, or soil mixing.

Meteoritic  $^{10}\text{Be}$  is not the only Be isotope used to trace Earth system processes.  $^7\text{Be}$  is formed by a similar cosmogenic pathway and is widely used as an atmospheric tracer, but due to its short half-life (53.2 days), it does not accumulate appreciably in soils.  $^9\text{Be}$  is the common stable isotope found in trace amounts in most geochemical systems. Cosmogenic  $^{10}\text{Be}$  also forms *in situ* within the mineral lattices of near-surface rock and sediment (Lal, 1988). Although *in situ*  $^{10}\text{Be}$  production rates are two orders of magnitude lower than meteoric  $^{10}\text{Be}$  deposition rates, and the isotope's analysis is only possible in certain mineral phases (mostly quartz), measurement of *in situ*  $^{10}\text{Be}$  has been widely preferred to meteoric  $^{10}\text{Be}$ . This is primarily because *in situ*  $^{10}\text{Be}$  is locked within the mineral lattice and will trace the fate of its host mineral in a 'closed system'. In contrast, meteoric  $^{10}\text{Be}$  distribution in soil is an 'open system', where the isotope will move through the soil system.

An understanding of the dynamics of meteoric  $^{10}\text{Be}$  behavior in soils is therefore crucial to its utility as a geochronometer, erosion rate monitor, and tracer of other

geophysical processes. This paper compiles and critically evaluates as a group all measurements of meteoric  $^{10}\text{Be}$  made in terrestrial soil profiles, from the first published measurements (Monaghan et al., 1983) to the present (July, 2010). This evaluation allows for analysis of both the typical distribution of meteoric  $^{10}\text{Be}$  and the control of various physical and chemical soil factors on the isotope's distribution.

## 2. METHODS

In order to examine the behavior of meteoric  $^{10}\text{Be}$  in terrestrial soil profiles, we compared the results of 679 measurements from 104 soil profiles in 27 studies conducted in globally diverse locations (Figure 1, Table 1) - an attempt to compile all such soil profiles. Soil profiles of buried paleosols in loess sequences were not included in the study (e.g. Curry and Pavich, 1996; Graham et al., 2001; Gu et al., 1996; Muhs et al., 2003; Zhou et al., 2007).

In order to improve the understanding of meteoric  $^{10}\text{Be}$  dynamics in the soil system, we examined the concentrations of meteoric  $^{10}\text{Be}$  measured as a function of depth. The overall shape of a meteoric  $^{10}\text{Be}$  concentration profile can be characterized and compared between geographic settings. To enable direct comparison between measurements taken at different accelerator mass spectrometers and using different AMS standards, we normalized all reported  $^{10}\text{Be}$  concentration values to the 07KNSTD standard widely used at present (Nishiizumi et al., 2007). Empirical coefficients correcting for the differences between AMS standards are available for all but the earliest measurements (Balco et al., 2008). In several studies, pH, grain size distribution, percent

organic carbon, cation exchange capacity,  $^9\text{Be}$  concentration, and dithionite-citrate extractable Al and Fe were measured in the same samples used to quantify meteoric  $^{10}\text{Be}$  concentration. The correlations between these soil properties and meteoric  $^{10}\text{Be}$  were examined to constrain the physical and chemical controls on meteoric  $^{10}\text{Be}$  soil distribution. The statistical significance and strength of correlation of each of these factors were tested on three levels: within individual soil profiles, between soil profiles with each profile averaged, and between soil profiles with every measurement treated individually. The raw data from all these measurements are available in the paper's electronic annex (cite web address here).

## 2.1 $^{10}\text{Be}$ Inventory

The total meteoric  $^{10}\text{Be}$  inventory of the soil profile is useful in certain applications. This meteoric  $^{10}\text{Be}$  inventory (atoms/cm<sup>2</sup>) is calculated:

$$N = \sum n \cdot \rho_s \cdot l \quad (1)$$

where  $n$ ,  $\rho_s$ , and  $l$  are the meteoric  $^{10}\text{Be}$  concentration (atoms/g), the bulk soil density (g/cm<sup>3</sup>), and the sample length (cm), respectively, of each sample in the profile.

If the long-term average meteoric  $^{10}\text{Be}$  deposition rate is known, the time required for the meteoric  $^{10}\text{Be}$  inventory to accumulate ( $t$ ) can be calculated assuming complete retention of meteoric  $^{10}\text{Be}$ :

$$t = (-1/\lambda) \log_e(1 - \lambda N/q) \quad (2)$$

where  $t$  is measured in years,  $\lambda$  is the  $^{10}\text{Be}$  disintegration constant  $5.0 \cdot 10^{-7} \text{ (yr}^{-1}\text{)}$  (Korschinek et al., 2010), and  $q$  is the local annual flux of meteoric  $^{10}\text{Be}$  atoms into the soil profile ( $\text{atoms} \cdot \text{cm}^{-2} \cdot \text{yr}^{-1}$ ).

If the soil is assumed to have been steadily eroding, an erosion rate in cm per year,  $E$ , can be calculated:

$$E = (q - \lambda N / (1 - e^{-\lambda t})) / C_v \quad (3)$$

Where  $t$  is the time since initial soil exposure (years) and  $C_v$  is the measured concentration per volume ( $\text{atoms}/\text{cm}^3$ ) of meteoric  $^{10}\text{Be}$  in the eroding soil horizon (Pavich et al., 1986). An erosion rate in terms of soil mass may be calculated if the meteoric  $^{10}\text{Be}$  concentration per mass ( $\text{atoms}/\text{g}$ ) is used instead.

When equation (3) is applied, a soil age must be known in order to calculate an erosion rate and visa versa. If the meteoric  $^{10}\text{Be}$  inventory of the soil is in steady state, with the rate of meteoric  $^{10}\text{Be}$  lost to erosion and decay equal to the meteoric  $^{10}\text{Be}$  deposition rate, then erosion can be calculated independent of age (Brown et al., 1988):

$$E = (q - \lambda N) / C_v \quad (4)$$

Depending on how the eroding soil horizon is defined, the results from equations (3) and (4) may vary.  $C_v$  must either be calculated using the meteoric  $^{10}\text{Be}$  concentration ( $\text{atoms}/\text{cm}^3$ ) in the uppermost sample or an average of the top several samples. One approach is to consider the soil A horizon as an integrated source of eroding sediment and apply the averaged meteoric  $^{10}\text{Be}$  concentration therein. (Lal, 2001).

### 3. RESULTS AND DISCUSSION

Meteoric  $^{10}\text{Be}$  concentrations vary in the 104 soil profiles from  $<10^7$  atoms/g in the lower horizons of rapidly eroding soils to  $>2\cdot 10^9$  atoms/g in old, slowly eroding soils and in soils with high meteoric  $^{10}\text{Be}$  deposition rates (e.g. Maejima et al., 2005). In the 22 meteoric  $^{10}\text{Be}$  profiles where distinct A, B, and C soil horizons were identified (Barg et al., 1997; Egli et al., 2010; Harden et al., 2002; Maejima et al., 2004; Pavich et al., 1986; Pavich et al., 1984; Pavich and Vidic, 1993; Shen et al., 2004a; Stanford et al., 2000), the full range of values is found in both A and B soil horizons, with an average of  $4.5\cdot 10^8$  atoms/g (Electronic Annex). C horizons have significantly less meteoric  $^{10}\text{Be}$ . If two outliers are excluded, all C horizon samples have meteoric  $^{10}\text{Be}$  concentration less than  $3\cdot 10^8$  atoms/g, with an average of  $1.3\cdot 10^8$  atoms/g (Electronic Annex).

### **3.1 Correlations with Soil Properties**

Mobile meteoric  $^{10}\text{Be}$  is retained in the soil system either by adsorption to soil particles or by incorporation as a cation into clays, organic matter, or oxyhydroxide phases (Barg et al., 1997). Adsorption of Be can be strongly influenced by both soil pH and grain size effects (Shen et al., 2004b; You et al., 1989). The abundance and distribution of mineral phases requisite for cation exchange likewise potentially controls meteoric  $^{10}\text{Be}$  concentration. In order to determine the relationship between meteoric  $^{10}\text{Be}$  and these soil properties, we calculated the statistical significance of their correlation with meteoric  $^{10}\text{Be}$  concentration in all of the soil profiles where both were concurrently measured (Figure 2).

Clay,  $^9\text{Be}$ , and dithionite-citrate extracted Al ( $\text{Al}_d$ ) significantly correlate to meteoric  $^{10}\text{Be}$  in more than half the soil profiles where they were measured. Sand content is negatively significant in more than half the profiles. Dithionite-citrate extracted Fe ( $\text{Fe}_d$ ) and cation exchange capacity are positive correlates, but the relationships are more often statistically insignificant. Silt, organic matter, and pH are typically not significantly correlated to meteoric  $^{10}\text{Be}$ ; correlations that do occur are neither consistently positive nor negative.

### *3.1.1 Grain Size*

The control of grain size on meteoric  $^{10}\text{Be}$  concentration can be assessed by comparing the weight percentage of sand, silt, and clay to meteoric  $^{10}\text{Be}$  in samples where both are measured (Table 1). The grain size – meteoric  $^{10}\text{Be}$  correlation is, in principle, controlled by two factors. 1) Smaller particles have higher surface area per mass and therefore provide more adsorption sites. This is confirmed by an approximately 3-fold increase in meteoric  $^{10}\text{Be}$  concentration between the sand and finest silt fractions in loess deposits (Shen et al., 2004b). 2) As new clay minerals form as weathering products in a soil system, they can incorporate mobile Be into their mineral lattices. In a soil profile where mineral and adsorbed phases were analyzed separately, 42 to 92% of the meteoric  $^{10}\text{Be}$  inventory of lower B and C horizon samples is within authigenic clay minerals (Barg et al., 1997).

The pattern of positive correlation between meteoric  $^{10}\text{Be}$  and clay, negative correlation with sand, and statistically insignificant correlation with silt that is widely

found in individual soil profiles (Figure 2) is also found when profile averages and aggregated individual measurements are compared (Figure 3). These correlations are partially soil age controlled, as both the weathering of sand to clay and the accumulation of meteoric  $^{10}\text{Be}$  increase with time. Silt content's demonstrable effect on meteoric  $^{10}\text{Be}$  adsorption (Shen et al., 2004b) may be negated by the loss of silt to clay with soil development, rendering the effect of silt content statistically insignificant. The limited capacity of sand to adsorb meteoric  $^{10}\text{Be}$  particle appears to restrict meteoric  $^{10}\text{Be}$  concentration in sand-rich layers, with the highest bulk concentrations ( $>2 \cdot 10^9$  atoms/g) only found in soil layers with  $<40\%$  sand.

### *3.1.2 Soil Chemistry*

Comparison of meteoric  $^{10}\text{Be}$  concentration to the concentrations of several other geochemically-active tracers reveals relationships more striking in their weakness of correlation than in their statistical significance (Figure 4). Some of this lack of fit is due to the varying chemical properties of diverse soil parent materials. But the general weakness of correlation suggests that meteoric  $^{10}\text{Be}$  distribution in soils is geochemically unique, and not readily predictable from the distribution of another chemical species.

#### *3.1.2.1 Stable $^9\text{Be}$*

Correlation between meteoric  $^{10}\text{Be}$  and stable, terrestrially-sourced  $^9\text{Be}$  is expected, as both isotopes bond with or adsorb to similar chemical sites. However, because  $^9\text{Be}$  becomes mobile as a weathering product, it will bond to clays and

oxyhydroxides in weathering horizons, but will not necessarily be positioned to adsorb to near-surface particles as meteoric  $^{10}\text{Be}$  will during deposition. The only moderate correlation between the two isotopes suggests that while the two isotopes do indeed bond at similar sites, meteoric  $^{10}\text{Be}$ 's atmospheric origin is relevant to its subsequent distribution.

### *3.1.2.2 Oxyhydroxide Minerals*

The percentage of dithionite-citrate extractable Al and Fe corresponds to the quantity of oxyhydroxides in the soil (Birkeland, 1999). Correlation between meteoric  $^{10}\text{Be}$  concentration and oxyhydroxide abundance is expected because Be can be incorporated as a cation in oxyhydroxide complexes (Barg et al., 1997; Takahashi et al., 1999), and because other meteoric  $^{10}\text{Be}$  phases (such as clays) may be illuviated similarly in podzolized soils (Birkeland, 1999). Al has a charge-ionic radius ratio similar to that of Be and has been suggested as a geochemical analog for meteoric  $^{10}\text{Be}$  (Jungers et al., 2009). While  $\text{Al}_d$  is significantly correlated to meteoric  $^{10}\text{Be}$  in several profiles (Figure 2), average  $\text{Al}_d$  content appears to be uncorrelated to average meteoric  $^{10}\text{Be}$  concentration when multiple profiles are compared (Figure 4b). In contrast, the  $\text{Fe}_d$  correlation primarily results from greater Fe-bearing oxyhydroxide content in meteoric  $^{10}\text{Be}$ -rich (older, more stable) soils (Figure 4c), with fewer significant correlations within individual profiles (Figure 2).

### *3.1.2.3 Cation Exchange Capacity*

The potential of soil colloid materials to incorporate cations, such as Be, into their lattice structures can be quantified empirically as a cation exchange capacity (CEC), measured in milliequivalents (Birkeland, 1999). Because a significant portion of a soil's meteoric  $^{10}\text{Be}$  inventory is incorporated into organic matter, clays, or oxyhydroxides via this pathway (Barg et al., 1997), potential correlations between CEC and meteoric  $^{10}\text{Be}$  are explainable. Nevertheless, these correlations are weak (Figure 4d) and seldom significant in individual profiles (Figure 2). As soil with a CEC of 1 meq/100g can, in principle, absorb up to  $3 \cdot 10^{18}$  atoms/g of Be, CEC is only limits meteoric  $^{10}\text{Be}$  concentration inasmuch as other cations compete with  $^{10}\text{Be}$  for exchange sites. Maximal meteoric  $^{10}\text{Be}$  concentrations ( $>2 \cdot 10^9$  atoms/g) are found in soils with CEC as low as  $\sim 7$  meq/100g. Below this value, CEC may potentially limit meteoric  $^{10}\text{Be}$  concentration.

#### *3.1.2.4 Organic Carbon*

Organic phases have a high CEC and often can contain significant portions of the meteoric  $^{10}\text{Be}$  inventory in A horizon samples (Barg et al., 1997). However, substantial organic carbon concentrations are almost always limited to the soil A horizon. Thus, a correlation between organic carbon and meteoric  $^{10}\text{Be}$  is only found when the highest meteoric  $^{10}\text{Be}$  concentrations are also in the A horizon (e.g. Harden et al., 2002). When meteoric  $^{10}\text{Be}$  is depleted in the upper horizon and enriched below, an anti-correlation is found (e.g. Shen et al., 2004a).

#### *3.1.3 Soil pH*

There has been some controversy in the meteoric  $^{10}\text{Be}$  literature concerning the extent to which meteoric  $^{10}\text{Be}$  is leached from acidic soils (e.g. Monaghan et al., 1983; Pavich et al., 1986). As humid soil types tend to become increasingly acidic over time (Birkeland, 1999), meteoric  $^{10}\text{Be}$ 's effectiveness as a long-term geochemical tracer would be limited if low pH soils were unable to retain the isotope. However, no statistically significant effect of soil pH on meteoric  $^{10}\text{Be}$  concentration is found either within individual profiles (Figure 2) or when average pH and average meteoric  $^{10}\text{Be}$  concentrations are compared between profiles (Figure 4f). When individual measurements from multiple profiles are compared, the soil concentrations values below pH 3.9 are statistically separable by an equal-variance t-test ( $p < 0.0001$ ) from the samples at pH 3.9 and above. At pH 3.9 and above, the full range of meteoric  $^{10}\text{Be}$  concentrations (including values above  $2 \cdot 10^9$  atoms/g) is found at every pH value, suggesting that at soil pH 3.9 and above, acid leaching has no statistically significant effect on meteoric  $^{10}\text{Be}$  concentration. Below pH 3.9, acidity may inhibit the accumulation of meteoric  $^{10}\text{Be}$  concentration, but substantial inventories of the isotope can nevertheless develop (e.g. Pavich et al., 1986).

Laboratory observations suggest that  $\text{Be}^{2+}$  starts to become mobile around pH 5.2 and is completely mobile at  $\sim$ pH 4 (Valette-Silver et al., 1986), limiting the isotope's ability to adsorb to soil materials (You et al., 1989). However, in the presence of humic acid, Be binds to oxalate complexes, not becoming fully mobile until  $\sim$  pH 2 (Takahashi et al., 1999). Thus, as long as chemically-active clay and oxyhydroxide sites remain in a

sufficiently humic soil system, major leaching of meteoric  $^{10}\text{Be}$  should not occur in all but the most acidic environments.

### 3.2 Typical Profile Shape

Most meteoric  $^{10}\text{Be}$  concentration profiles in soil have one of two general shapes: One, where the peak meteoric  $^{10}\text{Be}$  concentration value occurs in clay-rich B-horizon layers and typically has a meteoric  $^{10}\text{Be}$  concentration 2 to 3 times greater than A-horizon values and then declines to below A-horizon levels in the C or lower B horizons (Figure 5), is classified as a “bulge” type (Table 1). Another, where the peak meteoric  $^{10}\text{Be}$  values are found at the top of the profile followed by a steady decline below (Figure 6), is classified as a “decline” type (Table 1). Some profiles have a small bulge at the top of the profile, followed by a declining profile shape. A few profiles have a quasi-uniform distribution, displaying little variation with depth.

A bulge profile shape is found in approximately half of the profiles, while the declining profile shape is found in over a quarter (Electronic Annex). The average meteoric  $^{10}\text{Be}$  inventory of the decline-shaped profiles is an order of magnitude lower than the average inventory of all profile-shapes (Electronic Annex). These low-inventory, decline-shaped soil profiles are typically either found on actively eroding hillslopes (Harden et al., 2002; Mackey et al., 2009; McKean et al., 1993; Reusser and Bierman, 2010) or on young deposits (Balco, 2004; Pavich and Vidic, 1993).

Due to this meteoric  $^{10}\text{Be}$  inventory and profile shape relationship, the depth of the maximum measured meteoric  $^{10}\text{Be}$  concentration linearly correlates ( $R^2 = 0.53$ ) with

meteoric  $^{10}\text{Be}$  inventory (Figure 7). Because this maximum meteoric  $^{10}\text{Be}$  concentration is often significantly larger than the profile's average (Electronic Annex), it represents a zone of enhanced isotope accumulation that is necessarily controlled by the soil's physical and chemical properties. In young and rapidly eroding soils, this zone of maximum accumulation likely results from the simple adsorption of meteoric  $^{10}\text{Be}$  to upper soil particles and insufficient time for any appreciable transport to depth. With the progressive development of clays and oxyhydroxides in older soils, weathering meteoric  $^{10}\text{Be}$ -bearing phases may dissolve and reform as lower horizon clays (Barg et al., 1997) or be transported by illuviation processes. Flocculation and pore space restriction create a physical limit to the downward transport of clay, typically producing a restricted zone of maximum clay accumulation (Birkeland, 1999). The downwardly migrating bulge of meteoric  $^{10}\text{Be}$  concentration may correspond to this limit of illuviation (Figure 5).

The meteoric  $^{10}\text{Be}$  concentration in this zone of maximum isotope accumulation, strongly correlates ( $R^2 = 0.92$ ) to the total meteoric  $^{10}\text{Be}$  inventory (Figure 8). This correlation is more strongly predictive for smaller meteoric  $^{10}\text{Be}$  inventories, with root mean square error of 1.41 ( $1\sigma$ ) when only maximum meteoric  $^{10}\text{Be}$  values below  $3 \cdot 10^8$  atoms/g are considered and root mean square error of 2.07 for values above  $3 \cdot 10^8$  atoms/g. Inasmuch as meteoric  $^{10}\text{Be}$  inventory can be predicted from either the concentration or depth of the profile's maximum value, the history of the subsurface meteoric  $^{10}\text{Be}$  concentration bulge may describe the environmental history of the entire soil profile.

### *3.2.1 Control by Grain Size*

In a recent review, Willenbring and von Blankenburg (2010) suggest that most meteoric  $^{10}\text{Be}$  soil profiles will display an exponentially declining depth distribution once corrected for the effect of grain size on absorption (Shen et al., 2004b). Published grain size distributions typically do not have enough detail to test this precisely, but a rough approximation can be made by assuming silt is 5 times and sand 10 times less absorptive than clay (per the paleosol measured in Shen et al., 2004b). None of the 29 bulge-type profiles for which grain size data are available acquire a declining shape when this correction is applied, though in some cases the magnitude of the bulge is reduced (Electronic Annex). Absorption grain size effects therefore appear to be secondary to other factors controlling meteoric  $^{10}\text{Be}$  distribution in soils.

### *3.2.2 Tropical Oxic Soils*

Deep bauxite and ferricrete cores taken from tropical and subtropical locations (Barg et al., 1997; You et al., 1988) have markedly different meteoric  $^{10}\text{Be}$  profile shapes than those described above. These soils are often more than 10 meters deep and tend to have more uniform meteoric  $^{10}\text{Be}$  concentration with depth. In otherwise relatively uniform profiles, increases in meteoric  $^{10}\text{Be}$  concentration can occur at several meters of depth (e.g. You et al., 1988). This may be because the meteoric  $^{10}\text{Be}$  in these soils is primarily in the oxyhydroxide fraction (Barg et al., 1997), allowing substantially more transport to depth than clay. Tropical oxic soils have received only limited study; data from the three deep profiles collected are shown in Figure 9.

### 3.3 Soil Age or Residence Time

Early workers interpreted the meteoric  $^{10}\text{Be}$  inventory of a soil profile as either a measure of soil age (Pavich et al., 1986) or meteoric  $^{10}\text{Be}$  residence time (Monaghan et al., 1983). The soil age paradigm assumes that all of the meteoric  $^{10}\text{Be}$  deposited during the history of the soil is in the current inventory. This value then indicates the total length of time from the formation of the soil to present. Due to potential loss either to erosion, chemical leaching, or incomplete sampling, this age is often treated as a minimum (Pavich and Vidic, 1993). Net horizontal transport of meteoric  $^{10}\text{Be}$  must also be negligible. In treating the meteoric  $^{10}\text{Be}$  inventory as an isotope residence time, inventory is divided by deposition rate, thereby predicting the average length of time a meteoric  $^{10}\text{Be}$  atom has remained in the soil. Erosion, isotope decay, and chemical leaching act to shorten the length of this residence time by removing meteoric  $^{10}\text{Be}$  from the soil profile.

The soil ages / residence times derived from meteoric  $^{10}\text{Be}$  vary from less than  $10^3$  years in actively failing hillslopes (Mackey et al., 2009) to greater than  $10^6$  years in old, stable fluvial terraces (Pavich et al., 1986), with most in the  $10^4$  and  $10^5$  range (Electronic Annex). Many of these measurements are subject to considerable uncertainty arising from issues of sampling depth, meteoric  $^{10}\text{Be}$  deposition rate, and meteoric  $^{10}\text{Be}$  inherited in the soil parent material.

In constraining either a soil age or a meteoric  $^{10}\text{Be}$  residence time, it is important that the entire soil profile be sampled. In older soils, the meteoric  $^{10}\text{Be}$  concentration bulge is often at a depth of 1 to 3 m in the profile. If only the first meter of a bulge-type

profile is sampled, a large percentage of the total inventory may be missed. For example, in fluvial terraces of the Merced River, California (Pavich et al., 1986), between 65 and 85% of the  $^{10}\text{Be}$  inventory is found below the first meter (Table 2). If complete sampling is not possible, the meteoric  $^{10}\text{Be}$  inventory of the upper sections of soil can be interpreted as the isotope residence time of those layers only.

Converting a meteoric  $^{10}\text{Be}$  inventory to a soil age or residence time requires knowledge of the local, long-term meteoric  $^{10}\text{Be}$  deposition rate (Eq. 2). This deposition rate can be determined theoretically, through general circulation modelling (e.g. Field et al., 2006), or directly, by measuring  $^{10}\text{Be}$  concentration in local precipitation (e.g. Heikkilä et al., 2008a). Long term variation in meteoric  $^{10}\text{Be}$  deposition can also be modelled (Heikkilä et al., 2009), or estimated directly from long term meteoric  $^{10}\text{Be}$  inventories in sediment (e.g. Zhou et al., 2007). Local variation in meteoric  $^{10}\text{Be}$  deposition rate is controlled primarily by latitude and precipitation (Monaghan et al., 1986). While a few authors have based their assumed deposition rates on direct measurements (e.g. Maejima et al., 2005), most have used global average estimates, corrected for precipitation. While these estimates may be reasonable, they are poorly constrained. The validity of extrapolating short-term delivery rates to long-term averages represents a significant uncertainty in the interpretation of meteoric  $^{10}\text{Be}$  derived soil ages.

During their formation, many soils inherit at least some meteoric  $^{10}\text{Be}$  from their parent material. Bedrock of sufficient geologic antiquity will contribute little meteoric  $^{10}\text{Be}$  to daughter soils, due to the decay of the isotope. But in sediment sourced from other terrestrial soils or subject to marine isotope scavenging processes, inheritance can

be substantial (Table 3). The meteoric  $^{10}\text{Be}$  concentration in the parent material can be determined by two possible methods: 1) Modern sediment can be analyzed and the modern meteoric  $^{10}\text{Be}$  concentration subtracted from the measured meteoric  $^{10}\text{Be}$  concentrations of older sediments (Pavich et al., 1986). The weakness to this approach is that the modern meteoric  $^{10}\text{Be}$  concentration may not necessarily reflect the initial meteoric  $^{10}\text{Be}$  concentration in sediment deposited previously. 2) Unaltered parent material can be directly sampled by extending the soil profile deeply enough that material containing no contemporary meteoric  $^{10}\text{Be}$  is analyzed. This parent material can be recognized in profiles where meteoric  $^{10}\text{Be}$  concentrations decrease to an approximately consistent minimum over several consecutive samples (e.g. Harden et al., 2002). The meteoric  $^{10}\text{Be}$  concentration in the parent material is subtracted from the other concentration measurements in the profile (c.f. Anderson et al., 1996). If an inheritance correction is neglected, the soil age or residence time calculated from a meteoric  $^{10}\text{Be}$  inventory will be overstated.

### **3.4 Erosion Rates**

Equations (3) and (4) only accurately estimate soil erosion in cases where the concentration of meteoric  $^{10}\text{Be}$  lost per volume of soil lost is constant over time. Using a database of meteoric  $^{10}\text{Be}$  concentration profiles containing a wide range of soil ages (such as the one we have compiled), soil erosion rates (i.e. the long-term rate of soil volume removal from a vertical soil column) can be effectively modeled in situations where this assumption is invalid. This is done by making a space-for-time substitution

and assuming that when a modern soil had a smaller or larger meteoric  $^{10}\text{Be}$  inventory in the past, the depth distribution of that inventory was similar to that of other modern soils with similarly-sized inventories.

There are several common situations in which the assumption of a temporally uniform meteoric  $^{10}\text{Be}$  concentration in eroding material is invalid: 1) If a soil has formed recently enough that the eroding layer is continuing to progressively increase in meteoric  $^{10}\text{Be}$  concentration, the modern meteoric  $^{10}\text{Be}$  concentration in eroding material underestimates long-term soil loss, as past erosion would have removed less meteoric  $^{10}\text{Be}$  per soil volume than modern erosion removes. 2) If landscape modification is dominated by deep erosion processes, such as arroyo incision or shallow landsliding, that episodically remove a substantial portion of the meteoric  $^{10}\text{Be}$  inventory, the modern meteoric  $^{10}\text{Be}$  inventory will largely reflect the time since the last erosion event and will not relate to the rate of erosion. 3) If the erosion rate has recently changed substantially, typically from human impacts, the two erosion rates – recent and long-term will both control the meteoric  $^{10}\text{Be}$  inventory. In all of these cases, an erosion rate may still be estimated from measured meteoric  $^{10}\text{Be}$  concentrations, but various models based on space-for-time substitutions in reference datasets will typically need to be employed.

#### *3.4.1 Eroding Young Soils*

To create a reference dataset that models the temporal evolution of meteoric  $^{10}\text{Be}$  concentration in upper soil layers, we selected 65 profiles from our database, all from temperate mid-latitude sites, where the soil profile was likely mostly complete and

inheritance was constrained (Electronic Annex). As with the  $C_v$  term in equations (3) and (4), the upper soil meteoric  $^{10}\text{Be}$  concentration is calculated to an assumed erosion depth. Depending on a landscape's dominant erosion process, the frequency and soil volume loss of erosive processes may vary considerably. Processes such as sheetwash remove micrometers to millimeters of soil from the topmost eroding soil layer on a geologically continuous basis. Other processes such as mass wasting, gully incision, or tree toppling remove decimeters to meters of soil in discrete events. To allow for the consideration of a diverse range of soil volume loss, we compare deposition-rate normalized meteoric  $^{10}\text{Be}$  inventories to deposition-rate normalized average meteoric  $^{10}\text{Be}$  concentrations in the top 30, 70, and 150 cm of the dataset soils. (Consideration of the inventory – concentration relationship above 30 cm depth was not possible, because the top measurement in most of the database soil profiles integrates 10 to 30 cm of vertical material.) This produces a series of tight power law correlations (Figure 10), the components of which ( $\alpha, \beta$ ) can be used to construct a forward model of meteoric  $^{10}\text{Be}$  evolution. Because this model considers erosion discretely, all erosive processes are treated as an episodic series of events that remove the meteoric  $^{10}\text{Be}$  from the soil column up to a fixed depth of erosion. These equations can still be applied to soil removal by small-scale processes that penetrate very shallowly on an annual or multi-annual basis (e.g. sheet wash) by specifying an appropriately shallow depth of erosion.

If both the erosion rate ( $E$ ) and depth of erosion ( $z$ ) are approximately constant over time, the recurrence interval for erosion events ( $I$ ) can be described:

$$I = z/E \tag{5}$$

Given a meteoric  $^{10}\text{Be}$  inventory ( $N$ ), the number of meteoric  $^{10}\text{Be}$  atoms lost to an erosion event ( $N_L$ ) can be estimated:

$$N_L = z \cdot \alpha \cdot N^\beta \quad (6)$$

where  $\alpha$  and  $\beta$  are the components of the power-law relation between meteoric  $^{10}\text{Be}$  concentration up to  $z$  depth and total soil meteoric  $^{10}\text{Be}$  inventory in the reference dataset.

From an initial zero meteoric  $^{10}\text{Be}$  inventory, the meteoric  $^{10}\text{Be}$  inventory prior to the  $n^{\text{th}}$  erosion event is:

$$N = (N_{n-1} - N_{n-1L}) e^{-\lambda t} + q(1 - e^{-\lambda t}) / \lambda \quad (7)$$

When using data normalized by meteoric  $^{10}\text{Be}$  deposition rate, drop the  $q$  term from this equation. This model can be used to calculate erosion rates numerically, given parameters for  $\alpha$ ,  $\beta$ , and  $z$ .

As an example illustrating how model parameter selection effects erosion estimates, we use this method to assess the long-term erosion of a Merced River terrace known as the Turlock Lake Formation (Pavich et al., 1986). The age of this terrace is well-constrained to approximately 600 ka by a K-Ar date, and two meteoric  $^{10}\text{Be}$  soil profiles from the terrace show similar meteoric  $^{10}\text{Be}$  inventories, both indicating substantial meteoric  $^{10}\text{Be}$  loss to erosion (Table 2 – T6, T11). Erosion rates can be calculated using the parameters for  $\alpha$  and  $\beta$  derived from the complete data set of deposition-rate-normalized data from temperate, mid-latitude soils (Figure 10). However, the case could be made that central California, with its distinctive semi-arid climate, has a meteoric  $^{10}\text{Be}$  depth distribution distinct from more humid mid-latitude climates. If only data from central California is included in the reference dataset (McKean et al., 1993;

Monaghan et al., 1992; Pavich et al., 1986), slightly different values of  $\alpha$  and  $\beta$  are applied. Depending on trend and erosion event depth selection, erosion estimates for the Turlock Lake Formation vary within a factor of 3, with a central tendency around 5.5 m/My (Figure 9D). Examples of the forward models of soil meteoric  $^{10}\text{Be}$  inventory evolution used in these estimates are shown in Figure 11.

### *3.4.2 Deep Episodic Erosion*

If a soil had a meteoric  $^{10}\text{Be}$  inventory history similar to that shown in Figure 11A, it would not be possible to estimate soil erosion rates from a single inventory measurement. The soil's meteoric  $^{10}\text{Be}$  inventory is instead primarily controlled by the length of time since the last deep erosion event. In essence, the meteoric  $^{10}\text{Be}$  clock is partially reset by major erosion events; between events, the meteoric  $^{10}\text{Be}$  inventory rebuilds. In some landscapes dominated by deep episodic erosion, it may be possible to estimate the erosion rate by analyzing the range of meteoric  $^{10}\text{Be}$  inventories in multiple soil profiles. Such work has yet to be done.

In shallower episodic erosion cases, such as that shown in Figure 11B, the length of time since the last erosion event causes small fluctuations in the apparent erosion rate calculated from measured soil meteoric  $^{10}\text{Be}$  inventories. If the average depth of erosion events is known, this fluctuation can be expressed as an uncertainty or range of expected values (i.e. Figure 11D).

### *3.4.3 Recent Increases in Erosion Rates*

In cases where the rate of soil erosion has substantially increased (often due to human land use impacts), the effect can be quantified if pre-impact conditions are well understood. Harden and others' (2002) work comparing cultivated and uncultivated soils in the loess hills of western Iowa demonstrates how the effects of agricultural-induced erosion can be quantified using meteoric  $^{10}\text{Be}$ . In both ridgetop profiles, a consistent meteoric  $^{10}\text{Be}$  concentration minimum is reached below 150 cm depth, allowing for the application of the second inheritance calculation method discussed in section 3.5 (Figure 12). After inheritance is subtracted from the meteoric  $^{10}\text{Be}$  inventories, the meteoric  $^{10}\text{Be}$  age (eq. 2) of the uncultivated ridgetop is concordant with its radiocarbon age of 13.0 ka. The difference between the cultivated and uncultivated meteoric  $^{10}\text{Be}$  inventories represents the erosional loss due to agriculture. The soil volume of this loss can be calculated when an average meteoric  $^{10}\text{Be}$  concentration in the eroding soil is estimated. In this case, the volume of soil loss is further confirmed by the near-perfect match of the cultivated meteoric  $^{10}\text{Be}$  depth profile with the equivalent section preserved in the uncultivated profile (Figure 12).

#### **4. CONCLUSIONS AND IMPLICATIONS**

Assembly of a large dataset of meteoric  $^{10}\text{Be}$  soil measurements allows for analysis of the relationship between meteoric  $^{10}\text{Be}$  depth distribution and several other physical and chemical properties of soil. Although this analysis shows that several factors are correlated to meteoric  $^{10}\text{Be}$  concentration when data from multiple profiles are compared, no single factor is significantly related to the distribution of meteoric  $^{10}\text{Be}$  for

individual soil profiles in more than ~50% of cases. This is consistent with the complex control of meteoric  $^{10}\text{Be}$  distribution by a range of factors, including grain size effects on adsorption, incorporation into clays and oxyhydroxides during weathering, soil transport of clays and oxyhydroxides through illuviation, and the isotope's initial atmospheric source. Weak control by soil clay content and non-sand content suggests a grain size effect, though perhaps not as strong as others have proposed (i.e. Willenbring and von Blanckenburg, 2010). The collective weakness of correlation between meteoric  $^{10}\text{Be}$  and related extractable ions ( $^9\text{Be}$ , Al, and Fe) suggests that no one chemical species completely mirrors the behavior of meteoric  $^{10}\text{Be}$  in soil. The absence of any significant effect of soil pH confirms laboratory work suggesting the continued retention of Be in the oxalate phase in humic acid-bearing low pH conditions (Takahashi et al., 1999). Future analyses of meteoric  $^{10}\text{Be}$  in concert with other soil properties will further elucidate these relationships. Analysis of the meteoric  $^{10}\text{Be}$  content of specific soil phases (e.g. Barg et al., 1997) has the potential to be useful.

Analysis of meteoric  $^{10}\text{Be}$  depth distribution in the dataset soil profiles reveals generally consistent patterns. In young soils and quickly eroding soils, maximum meteoric  $^{10}\text{Be}$  concentrations are found toward the top of the soil profile. In older and more slowly eroding soils, the maximum meteoric  $^{10}\text{Be}$  concentration is found at depth. This pattern is consistent with a zone of maximum meteoric  $^{10}\text{Be}$  accumulation whose concentration and depth increases with total isotope inventory. The correlation between maximum meteoric  $^{10}\text{Be}$  concentration and total meteoric  $^{10}\text{Be}$  inventory is strong enough that they predict each other with root mean square error as low as 1.41. This, along with

the tight correlations between upper soil meteoric  $^{10}\text{Be}$  concentration and total inventory, may allow for estimation of meteoric  $^{10}\text{Be}$  inventories in cases where the entire inventory cannot be sampled, such as in detrital studies.

In using meteoric  $^{10}\text{Be}$  to solve broader geologic problems, such as soil age or erosion rate, this compilation indicates the importance of completely sampling a soil to and below the depth of meteoric  $^{10}\text{Be}$  penetration. If the sampled profile does not reach bedrock or unaltered parent material, the resulting meteoric  $^{10}\text{Be}$  inventory will be too low and thus calculations will result in underestimated ages or overestimated erosion rates. Much of the existing work on meteoric  $^{10}\text{Be}$  in soils may understate soils' meteoric  $^{10}\text{Be}$  inventory. Of the 104 profiles compiled, 48 are a meter or shorter in length, and 56 of the 104 profiles do not reach the soil C horizon. An incompletely sampled profile can still provide a minimum age or a maximum erosion rate, if other uncertainties, such as long-term meteoric  $^{10}\text{Be}$  deposition rate, are constrained.

Accurate calculations also require that the concentration of meteoric  $^{10}\text{Be}$  in the soil parent material be considered. If this inherited meteoric  $^{10}\text{Be}$  concentration is neglected, the resulting meteoric  $^{10}\text{Be}$  inventory will overestimate soil age and underestimate erosion rate. The most effective way to assess inheritance is to sample unaltered parent material beneath the soil profile, also requiring that the soil profile be sampled deeply and thus entirely. Where soil is forming from bedrock and in steady-state situations, an inheritance calculation is not necessary.

Although meteoric  $^{10}\text{Be}$  will not typically provide a precise soil age, meteoric  $^{10}\text{Be}$  inventory data often bracket a soil age and are a useful proxy for a soil profile's

erosion and deposition history. In general, the more information that is known about the geologic context of the soil profile, the more information can be learned by measuring meteoric  $^{10}\text{Be}$ . The style of erosion and the meteoric  $^{10}\text{Be}$  concentration inherited from the parent material are particularly important parameters to characterize well. The possibility of loss to acid leaching should still be considered in shallow acidic soils where preferential flow paths are well developed. The presented global compilation of meteoric  $^{10}\text{Be}$  data both illustrates and begins to constrain many of the complexities in the soil meteoric  $^{10}\text{Be}$  system. As future work further constrains uncertainties and expands the method to new soil types, the measurement of meteoric  $^{10}\text{Be}$  in soils has the potential to become an increasingly robust monitor of  $10^3$  to  $10^6$  year timescale soil and earth system processes.

### **ACKNOWLEDGEMENTS**

Work supported by National Science Foundation grant ARC-0713956. Manuscript handled by associate editor G. Herzog, who along with A. Albrecht and two anonymous reviewers made helpful suggestions for improvement. Conversations with G. Pinder, A. Bacon, G. Druschel, G. Balco, and E. Portenga were beneficial..

## Chapter 3 Tables

Table 1: Summary of soil profile database

First Author	Year	# of profiles	Location	Approx. Lat. Long.	Soil Environment	Profile Types	Properties Measured[1]
Monaghan	1983	3	Mendocino, California	39°19'N 123°48'W	Coastal Terraces	Unknown[3]	OC
Monaghan	1983	2	Friant, California	37°00'N 119°42'W	Tabletop / Alluvial fan	Unknown[3]	OC
Pavich[2]	1984	6	Virginian Coastal Plain	~38°N 76°W	Alluvial Terraces	Mostly Bulge	GS, Al, Fe CEC, pH
Pavich	1985	1	Northern Virginia	38°58'N 77°16'W	Piedmont Saproliite	Bulge	Cl
Pavich[2]	1986	7	Merced River California	37°30'N 120°25'W	Fluvial Terraces	Bulge	GS, Fe CEC, OC, pH
You	1988	1	Northern Taiwan	25°11'N 121°30'E	Deep Bauxite Core	Quasi-uniform bulge at depth	
Brown, L	1988	1	Northern Virginia	Near Pavich85	Piedmont Saproliite	Decline	
Bouchard	1989	3	Gaspe, Quebec	48°50'N 65°50'W	Till - Saproliite Sequences	Various	GS
Brown, ET	1992	1	Parguanza, Venezuela	~6°N 67°W	Tropical	Quasi-uniform	
Monaghan	1992	2	Contra Costa, California	37°57'N 121°52'W	Hillslope	Bulge	OC
McKean	1993	3	Contra Costa, California	37°57'N 121°52'W	Hillslope	Decline	
Pavich[2]	1993	11	Slovenia	46°20'N 14°15'E	Glacial Fluvial Terraces	Mostly Bulge	GS, Al, Fe CEC, OC, pH
Barg	1997	3	Virginia, Ivory Coast, Mali	Various	Various	Various	<sup>9</sup> Be
Stanford	2000	1	New Jersey Piedmont	40°21' N 74°34'W	Piedmont Saproliite	Decline	
Graham	2002	1	Antarctica: Arena Valley	77°50'S 161E	Valley floor	Decline	
Harden	2002	6	Western Iowa	~41°N 95°W	Loess Deposits	Various	OC
Balco	2004	1	Minnesota	44°35'N 93°55'W	Glacial Till	Decline	
Shen	2004	1	Guangdong, China	22°41'N 112°54'E	Hillslope	Bulge	OC
Maejima	2004	6	Southern Japan	26-35°N 128-142°E	Red soils / Various	Mostly Bulge	Cl, pH
Maejima[2]	2005	6	Kikai Island, Japan	28°18' N 129°58' E	Coastal Terraces	Various/ Unknown[3]	GS, <sup>9</sup> Be, pH
Asano	2007	5	Mongolia	44-48°N 103-111°E	Various	Mostly Decline	
Tsai	2008	3	Taiwan	~24°N ~121°E	Fluvial Terraces	Bulge	GS, Fe, CEC, pH

Table 1, Continued.

First Author	Year	# of profiles	Location	Approx. Lat. Long.	Soil Environment	Profile Types	Properties Measured[1]
Schiller	2009	1	Antarctic Dry Valleys	77°30'S 162°22'E	Gravel lag on Paleosol	Bulge	
Mackey	2009	5	Eel River, California	40°7'N 123°30'W	Hillslope Earthflow	Mostly Decline	
Jungers[2]	2009	10	Smokey Mnts, Tennessee	35°33'N 83°11'W	Hillslope	Bulge(?) [3]	Cl, Al, Fe pH
Reusser	2010	2	Waipaoa, New Zealand	38°30'S 177°54'E	Hillslope / Fluvial Terrace	Decline	
Fifield	2010	5	Southeast Australia	35°36'S 149°16'E	Hillslope	Bulge	
Fifield	2010	1	Northwest Australia	17°20'S 128°54'E	Hillslope	Decline	
Elgi	2010	6	Swiss and Italian Alps	~46°30'N ~9°E	Glacial Moraines	Various	GS, Al, Fe OC, pH

[1]: GS = Grain Size Distribution, Cl = Clay Percent,  $^9\text{Be} = ^9\text{Be}$  in leachable soil phases, Al = Dithionite-extracted Al, Fe = Dithionite-extracted Fe, OC = Percent Organic Carbon, CEC = Cation Exchange Capacity

[2]: Some soil properties data is reported elsewhere (HARDEN, 1987; JUNGERS and BIERMAN, 2009; MARKEWICH et al., 1987; NAGATSUKA and MAEJIMA, 2001; PAVICH et al., 1989; VIDIC, 1994)

[3]: Monaghan and others [1983], Maejima and others [2005], and Jungers and others [2009] have profiles under 100 cm deep the ultimate shapes of which are difficult to assess.

Table 2: Topsoil  $^{10}\text{Be}$  inventories in Merced River terraces (Pavich et al., 1986)

Borehole	Geologic	$^{10}\text{Be}$	Percent of $^{10}\text{Be}$ Inventory contained in the top:					
	Age (ka)	Age (ka)*	50 cm	100 cm	150 cm	200 cm	250 cm	300 cm
M12	40	56	10.6%	24.7%	63.8%	93.6%	100.0%	100.0%
R9	140-260	218	9.6%	24.0%	45.2%	63.5%	74.0%	84.6%
R10	140-260	182	13.0%	34.8%	53.0%	66.2%	75.9%	84.8%
T6	600	245	5.5%	14.9%	40.1%	62.4%	73.4%	84.4%
T11	600	222	16.9%	35.9%	49.4%	62.7%	75.1%	84.4%
CH1	1800-3000	989	8.6%	22.9%	37.4%	49.1%	58.5%	63.1%
CH2	1800-3000	845	8.4%	28.7%	40.0%	48.4%	53.2%	58.2%

\*Age is calculated assuming zero erosion, meteoric  $^{10}\text{Be}$  inheritance of modern alluvium, and a meteoric  $^{10}\text{Be}$  deposition rate of  $0.52 \cdot 10^6$  atoms/(cm<sup>2</sup>·year). For the older profiles, the zero erosion assumption is not valid.

Table 3: Inherited meteoric  $^{10}\text{Be}$  concentrations in various sediments

Material	Location	Approximate Inherited $^{10}\text{Be}$ (atoms/g)	First Author	Year
Fluvial Sediment	Eastern US	$10^8$ to $10^9$	Brown, L	1988
Fluvial Sediment	Merced River, Ca	$10^8$	Pavich	1986
Fluvial Sediment	Amazon & Orinoco Rivers	$10^7$ to $6 \cdot 10^7$	Brown, ET	1992
Fluvial Sediment	Waipaoa, New Zealand	$3.3 \cdot 10^7$ <sup>[1]</sup>	Reusser	2010
Glacial Fluvial Sediment	Slovenia	$4.3 \cdot 10^7$ <sup>[1]</sup>	Pavich	1993
Glacial Till	Minnesota	$10^7$ to $3 \cdot 10^8$	Balco	2004
Glacial Loess	Iowa	$4.5 \cdot 10^7$ <sup>[1]</sup>	Harden	2002
Desert Loess	China	$10^8$	Gu	1996
Loess	New Zealand	$10^9$	Graham	2001
Coral	Ryukyu	$2.3 \cdot 10^8$ <sup>[2]</sup>	Maejima	2005

<sup>[1]</sup> Calculated from soil profile by assuming lower layers were unaffected by soil forming processes, based on uniform meteoric  $^{10}\text{Be}$  concentration.

<sup>[2]</sup> Calculated from 5.2 ka marine terrace's meteoric  $^{10}\text{Be}$  inventory, subtracting inventory expected from the contemporary meteoric  $^{10}\text{Be}$  deposition in precipitation.

### Chapter 3 Figures



Figure 1: World map with approximate locations of database soil profiles. Number indicates number of samples at location. At unnumbered locations, only one profile was sampled.

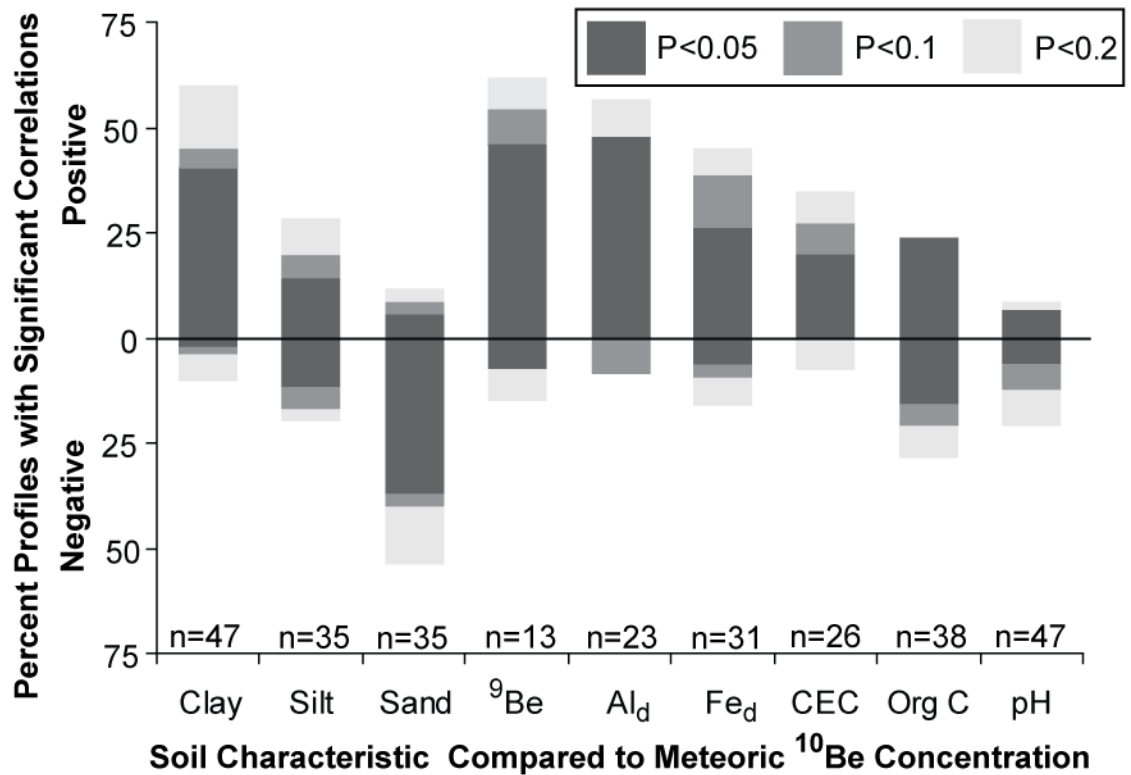


Figure 2: Percentage of soil profiles for which selected soil characteristics are significantly correlated to meteoric  $^{10}\text{Be}$  concentration. Percentage with positively and negatively significant correlations are plotted above and below the zero-valued line, respectively, for p values of 0.05, 0.1, and 0.2. Weight percentage clay, silt, sand, acid extracted  $^9\text{Be}$ , dithionite-citrate extracted Al and Fe, organic carbon, cation exchange capacity, and pH (KCl) are shown.

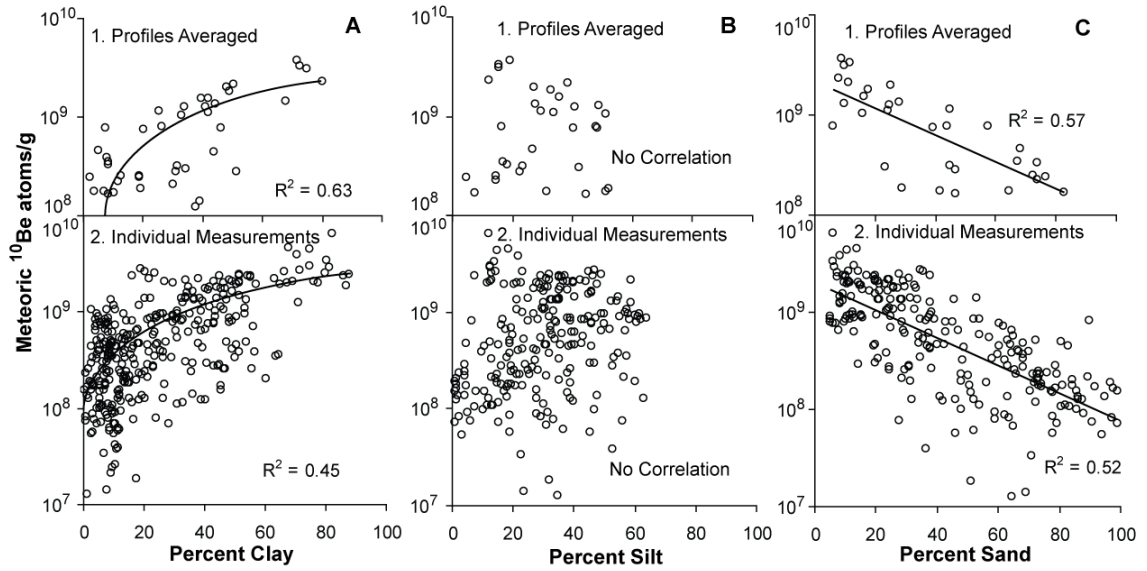


Figure 3: Relationship between meteoric <sup>10</sup>Be concentration and weight percent of clay (A), silt (B), and sand (C). Profile average values (1) and individual measurements (2) are compared. Linear or exponential correlations are plotted where the relationship is statistically significant.

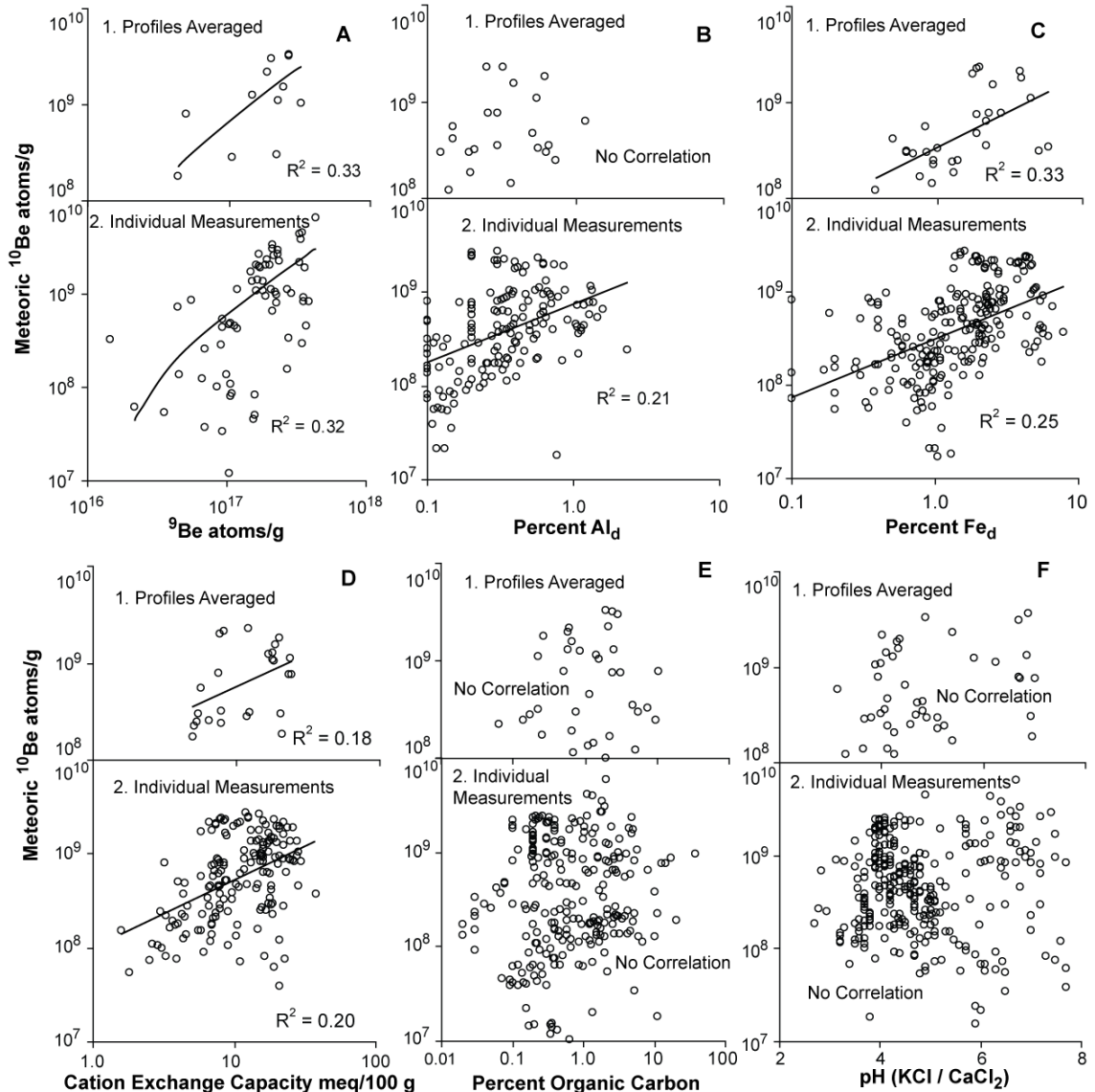


Figure 4: Relationship between meteoric <sup>10</sup>Be concentration and acid extractable <sup>9</sup>Be (A), dithionite-citrate extractable Al (B), dithionite-citrate extractable Fe (C), cation exchange capacity (D), organic carbon (E), and pH (F). Profile average values (1) and individual measurements (2) are compared. Linear or exponential correlations are plotted where the relationship is statistically significant.

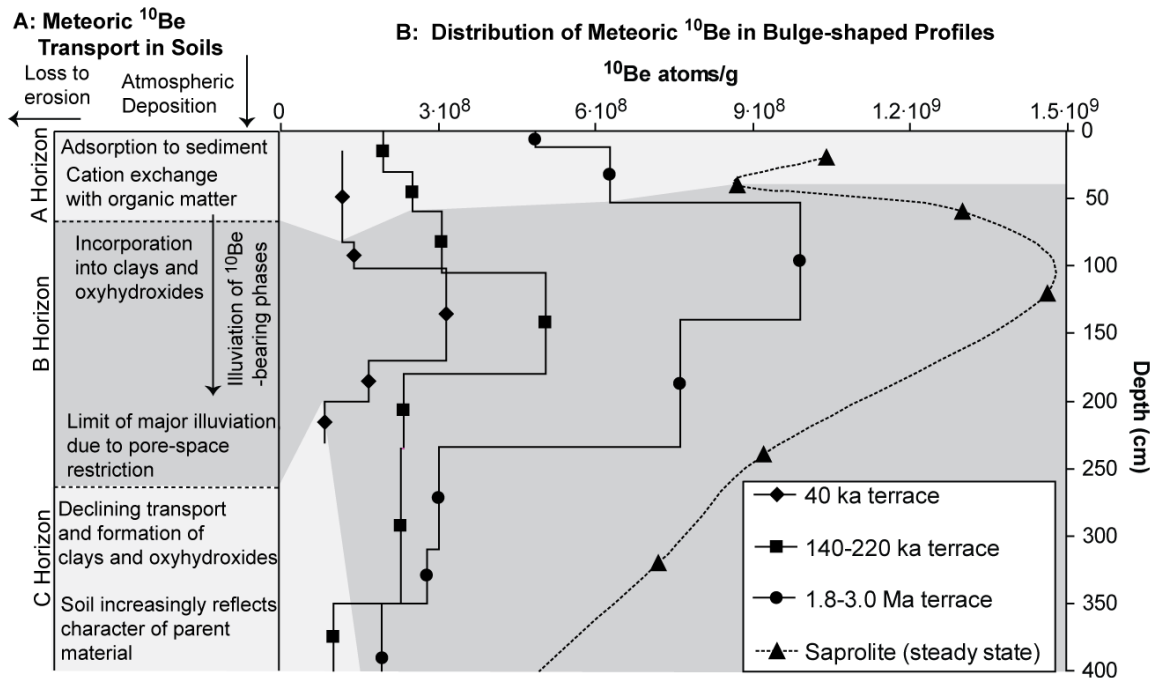


Figure 5: Conceptual model of the control of soil processes on meteoric  $^{10}\text{Be}$  distribution (A) compared to the top 400 cm of selected meteoric  $^{10}\text{Be}$  depth profiles from fluvial terraces of the Merced River, California (Pavich et al., 1986) and a Virginia saprolite core (Pavich et al., 1985) showing the typical “bulge” profile shape (B). Dashed lines indicate interpolation between point-sampled measurements. Solid lines indicate sections of the profile were integrated in the field during sample collection.

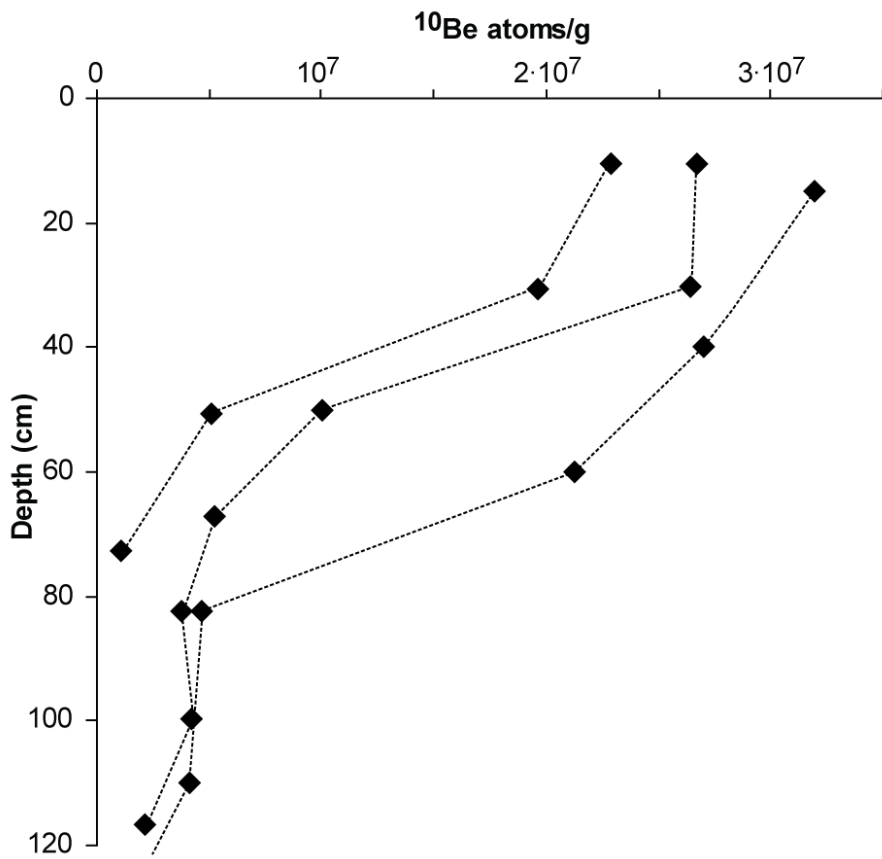


Figure 6: Hillslope profiles from Contra Costa, California showing declining profile shape (McKean et al., 1993). Dashed lines indicate interpolation between point-sampled measurements.

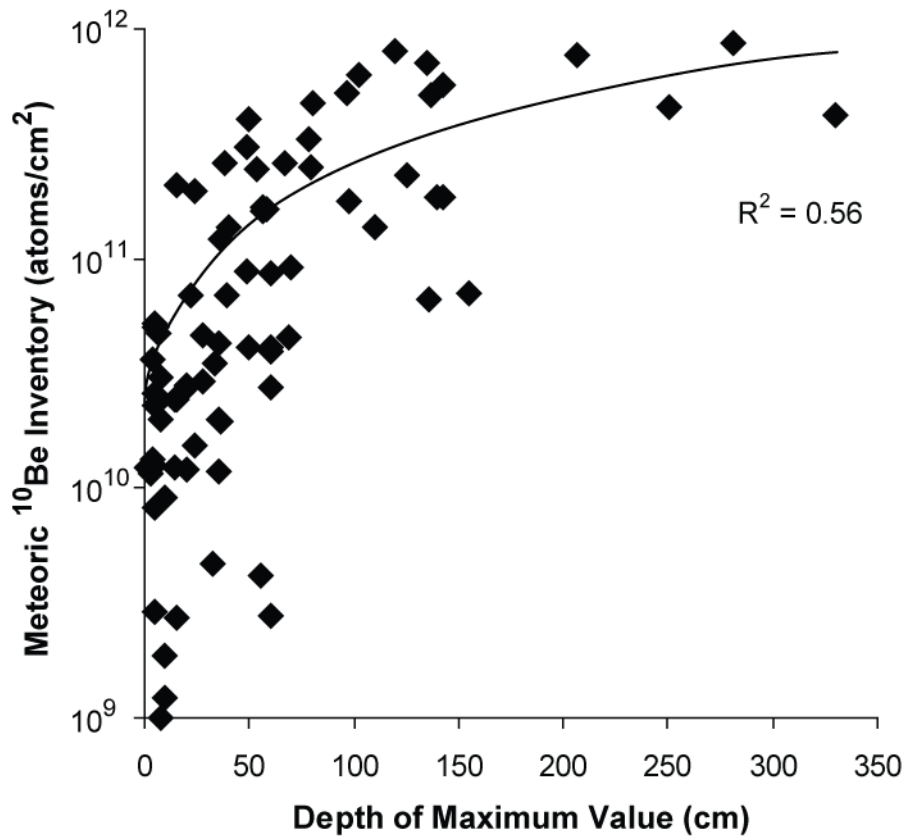


Figure 7: Linear fit between total meteoric <sup>10</sup>Be inventory (atoms) and depth of maximum meteoric <sup>10</sup>Be concentration (cm). Where the maximum meteoric <sup>10</sup>Be concentration was sampled over a range of depths, the median depth is used. Tropical deep oxic soils (Barg et al., 1997; You et al., 1988) are excluded from this trend. Such tropical soils can have maximum meteoric <sup>10</sup>Be concentrations located between 2 and 12 meters depth, with relatively small total meteoric <sup>10</sup>Be inventories.

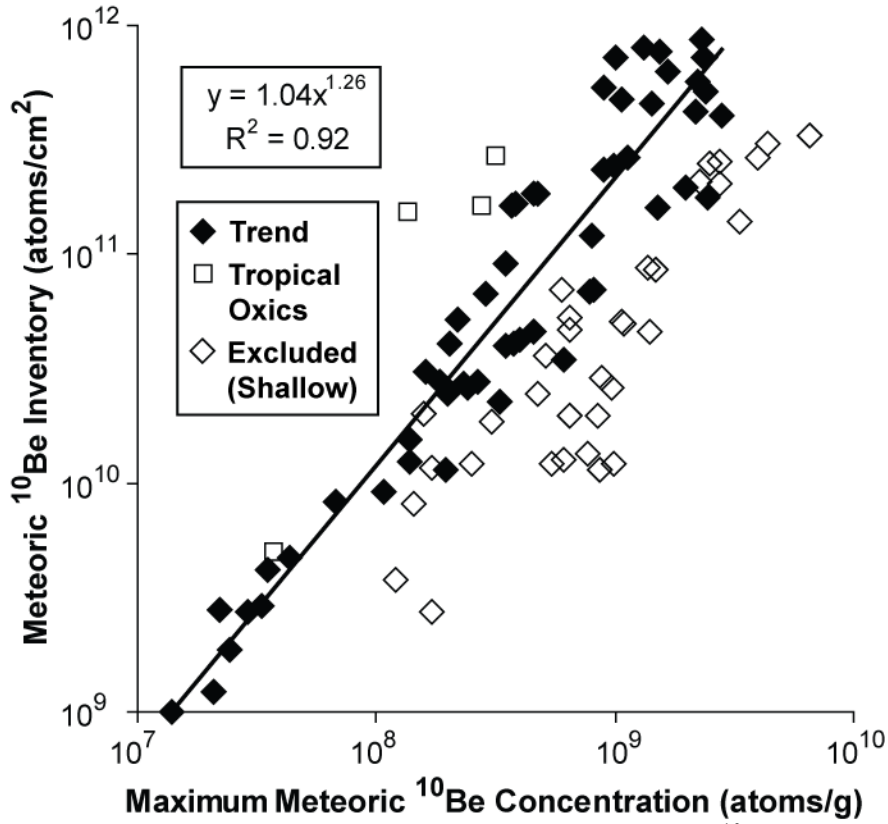


Figure 8: Power law correlation between peak meteoric  $^{10}\text{Be}$  concentration (atoms/g) and total  $^{10}\text{Be}$  inventory (atoms) in database profiles. Profiles less than 1 meter long that did not reach a C horizon are shown as open diamonds and are excluded from the trend. Deep oxic soils (squares) are also excluded.

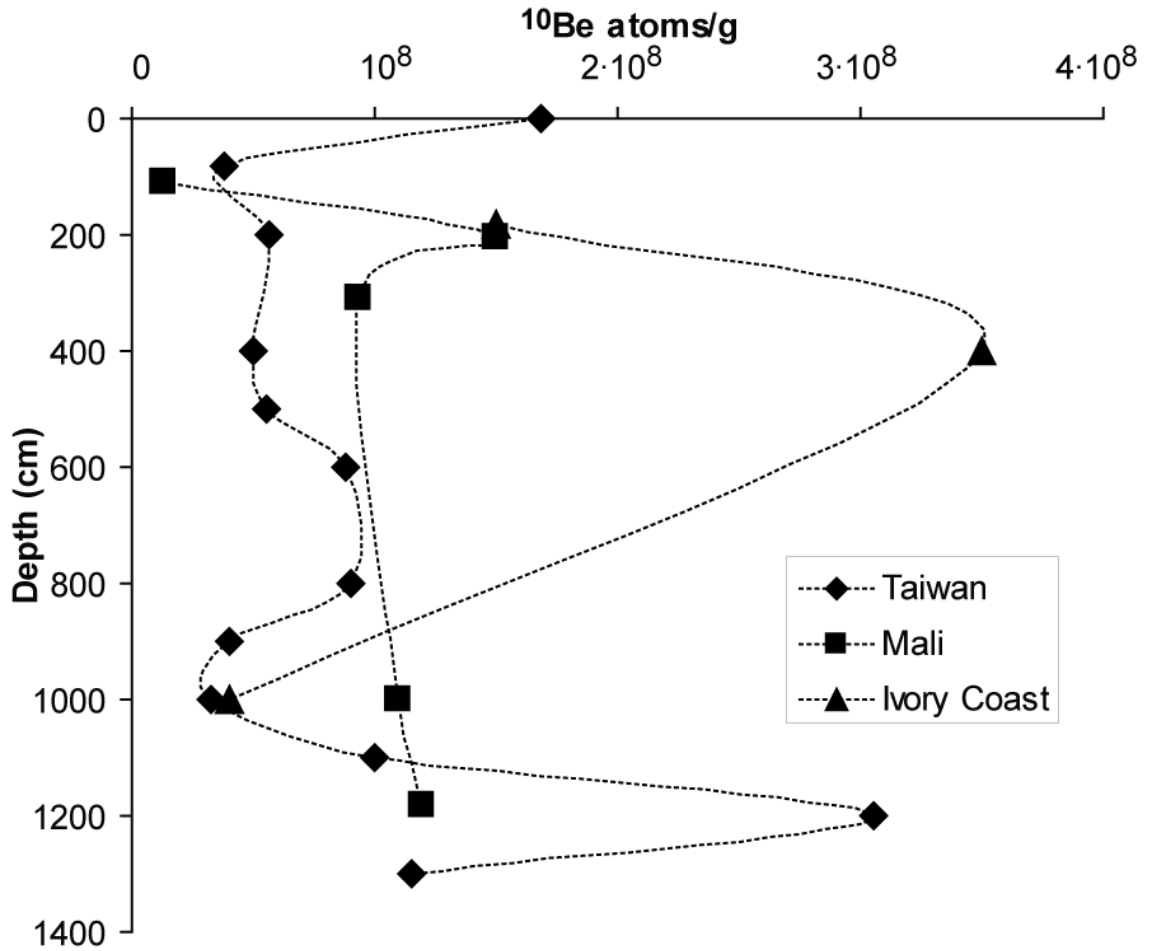


Figure 9: Tropical and subtropical oxic soils (Barg et al., 1997; You et al., 1989) showing deeper infiltration of meteoric  $^{10}\text{Be}$  and different profile shape dynamics than temperate soil profiles. Dashed lines indicate interpolation between point-sampled measurements.

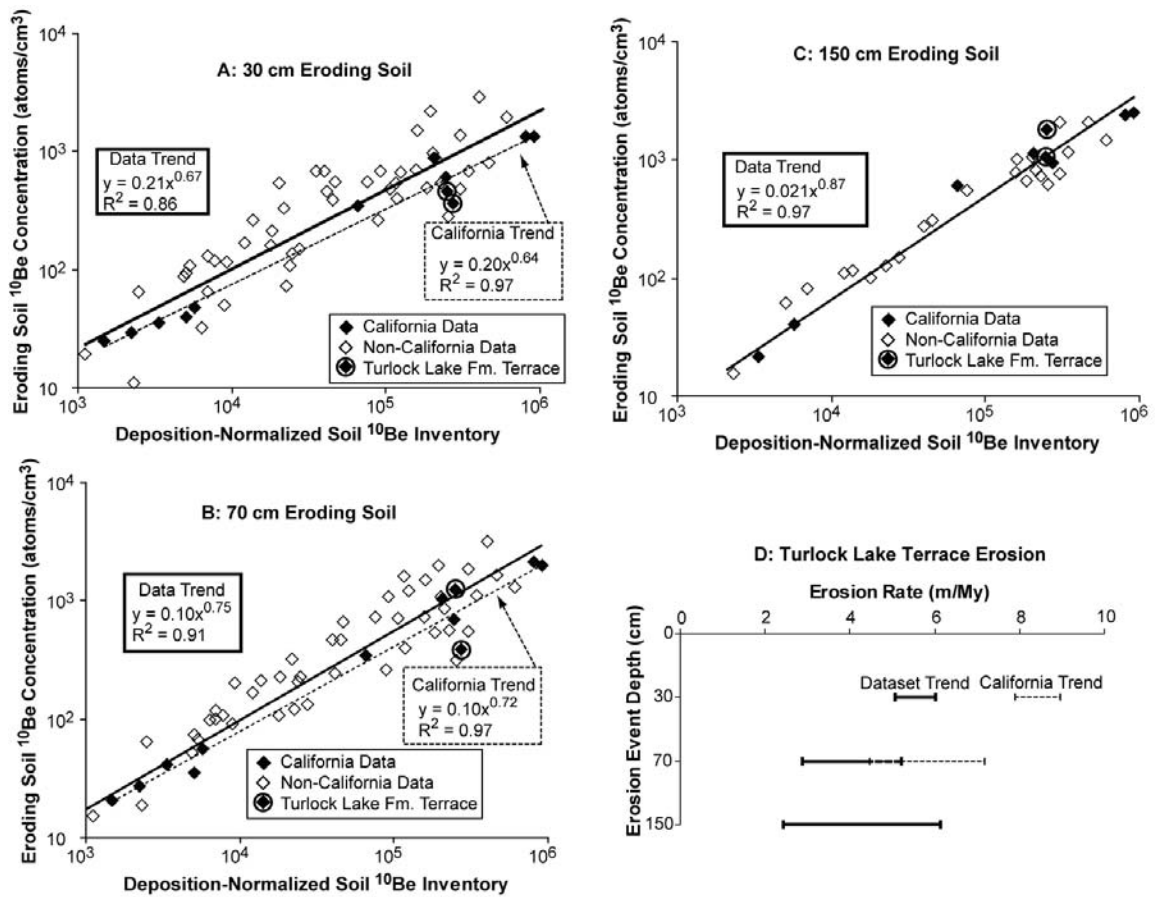


Figure 10: Upper soil meteoric  $^{10}\text{Be}$  concentrations vs. meteoric  $^{10}\text{Be}$  inventory in database soils. In this treatment, the meteoric  $^{10}\text{Be}$  inventory ( $\text{atoms}/\text{cm}^2$ ) is divided by the local meteoric  $^{10}\text{Be}$  deposition rate ( $\text{atoms}\cdot\text{cm}^{-2}\cdot\text{year}^{-1}$ ), effectively normalizing the data to a single deposition rate. Concentrations in  $\text{atoms}/\text{cm}^3$  are used to quantify volume rather than mass of soil loss to erosion. The upper soil is defined alternatively as the top 30, 70, or 150 cm of the profiles (A-C). Soil profiles shorter than the upper soil depth are excluded from the trends. Separate trends are calculated for profiles from central California. Maximum and minimum erosion rates for the Turlock Lake Formation terrace of the Merced River (Pavich et al., 1986) are estimated in panel D.

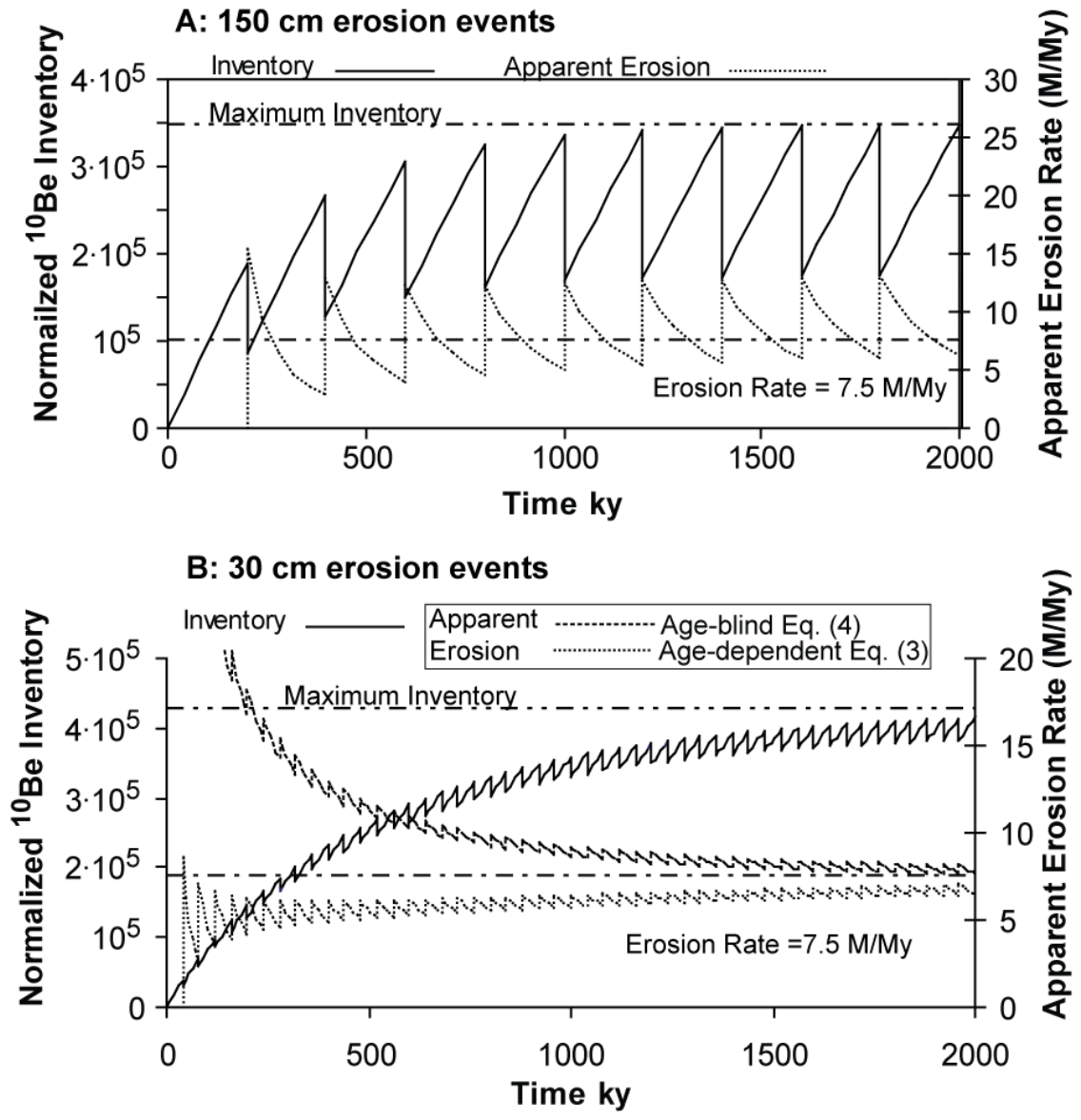


Figure 11: Model of meteoric  $^{10}\text{Be}$  inventory (atoms) over time with 150 cm and 30 cm erosion events and constant 7.5 m/My erosion rates. The erosion rate calculated if the measured upper soil meteoric  $^{10}\text{Be}$  concentration is assumed to be constant is also shown. In A, equation (3) is used. In B, both results from equations (3) and (4) are shown.

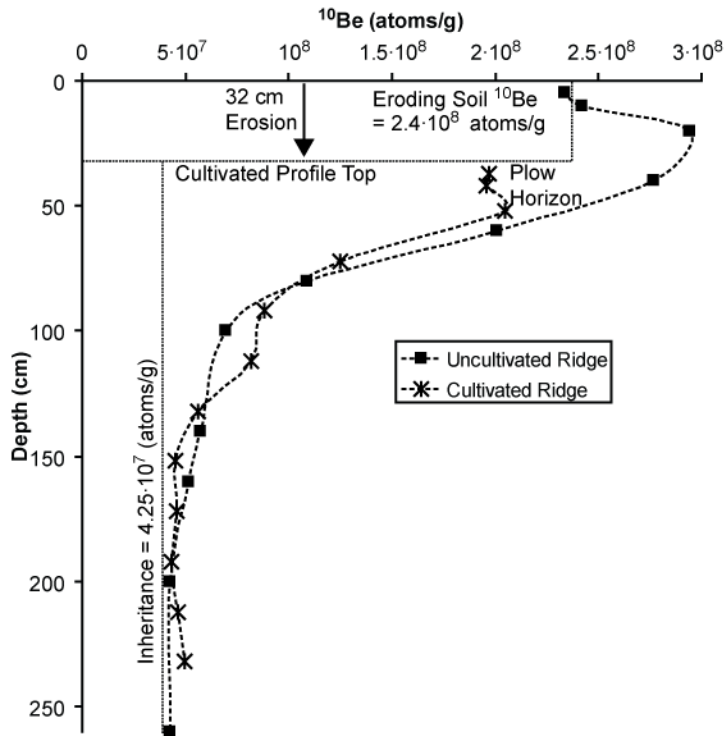


Figure 12: Meteoric  $^{10}\text{Be}$  depth profiles from uncultivated and cultivated ridges in the loess hills of Western Iowa (Harden et al., 2002). The cultivated profile is plotted with depth corrected for erosional loss.

**Chapter 4: Making global and temporal sense of meteoric  $^{10}\text{Be}$  deposition rates**  
(submitted as a separate paper to *Earth and Planetary Science Letters*)

**ABSTRACT**

In order to understand the spatial and temporal distribution of meteoric  $^{10}\text{Be}$  delivery to Earth's surface, contemporary, short-term measurements of meteoric  $^{10}\text{Be}$  in precipitation are compared to terrestrial geologic records of meteoric  $^{10}\text{Be}$  accumulation. In precipitation measurements, it is possible to deconvolve the contribution of atmospherically-produced "primary" meteoric  $^{10}\text{Be}$  from "recycled" meteoric  $^{10}\text{Be}$  delivered by terrestrial dust, if a second isotope is measured that quantifies either the recycled or primary components of meteoric  $^{10}\text{Be}$  deposition. In this paper, we use dust-concentration dependent differences between  $^7\text{Be}$  and  $^{10}\text{Be}$  measurements to make new estimates of the recycled contribution to total meteoric  $^{10}\text{Be}$  flux delivered to Earth's surface. These dust-corrected data show a strong linear dependence between precipitation amount and primary meteoric  $^{10}\text{Be}$  flux. Concentrations of primary meteoric  $^{10}\text{Be}$  in mid-latitude and low-latitude precipitation vary by latitude between  $0.65 \cdot 10^4$  and  $2.3 \cdot 10^4$  atoms/cm<sup>3</sup> of precipitation according to a sigmoidal fit ( $n=19$ ,  $R^2 = 0.95$ ). This fit provides a first-order estimate of primary meteoric  $^{10}\text{Be}$  deposition for a given latitude and precipitation rate.

Well-constrained, long-term average, total meteoric  $^{10}\text{Be}$  deposition rates are essential when this isotope is used as a chronometer or tracer of Earth surface processes. Though long-term variation in meteoric  $^{10}\text{Be}$  deposition has been quantified in ice and ocean sediment cores, these archives do not represent site-specific terrestrial conditions

well. Here, we estimate time-integrated meteoric  $^{10}\text{Be}$  deposition rates from meteoric  $^{10}\text{Be}$  inventories measured in dated terrestrial soils. In soils with minimally-eroded surfaces whose ages are tightly-constrained by another method, the decay-corrected soil meteoric  $^{10}\text{Be}$  inventory is used to calculate the time-averaged, total meteoric  $^{10}\text{Be}$  deposition rate over the soil's history. In published soil profiles where dating and no erosion assumptions are met, long-term meteoric  $^{10}\text{Be}$  deposition rates generally match contemporary deposition rates estimated from latitude and precipitation, but with substantial variability due to changes in climate,  $^{10}\text{Be}$  supplied by dust, and variations in magnetic field intensity.

## 1. INTRODUCTION

Meteoritic  $^{10}\text{Be}$  is a cosmogenic isotope formed by the spallation of oxygen and nitrogen atoms in the upper atmosphere (Lal and Peters, 1967). The isotope, with a half life of 1.36 my (Nishiizumi et al., 2007), adheres to aerosols and falls out in precipitation or as dry deposition (McHargue and Damon, 1991) accumulating in geologic archives including sediment and ice. Over the past several decades, meteoric  $^{10}\text{Be}$  has been used as a tracer for a wide set of Earth processes occurring over time scales of up to  $10^7$  years, including tracking soil movement (e.g. McKean et al., 1993), estimating landform age (e.g. Pavich et al., 1986), and tracing subducted sediment (e.g. Morris et al., 2002). Long-lived archives of meteoric  $^{10}\text{Be}$  deposition are contained in ice sheets (e.g. Finkel and Nishiizumi, 1997) and oceanic sediments (e.g. Frank et al., 1997). These records have been considered proxies for solar activity and Earth's magnetic field strength, as

both deflect cosmic rays from Earth's atmosphere thus changing rates of  $^{10}\text{Be}$  production and delivery to Earth's surface (Masarik and Beer, 1999).

Meteoric  $^{10}\text{Be}$  is delivered to Earth's surface either adhering to aerosols or as airborne dust (McHargue and Damon, 1991). Both the aerosols and the dust can either be scavenged by precipitation systems or fall out as dryfall. The aerosols contain  $^{10}\text{Be}$  produced in the atmosphere; dust contains  $^{10}\text{Be}$  that is recycled from terrestrial sources (Baumgartner et al., 1997). These are subsequently referred to as the "primary" and "recycled" components of meteoric  $^{10}\text{Be}$  deposition, respectively.

Once deposited on terrestrial surfaces, meteoric  $^{10}\text{Be}$  accumulates in soil profiles and the total meteoric  $^{10}\text{Be}$  inventory in a soil profile can be used to calculate a soil age or erosion rate if a variety of assumptions are met (Pavich et al., 1986). These include long-term retention of meteoric  $^{10}\text{Be}$  in soils, knowledge of meteoric  $^{10}\text{Be}$  concentrations inherited from soil sediment sources, and the assumption of steady loss by physical removal for erosion-rate estimation. These assumptions are similar to those underlying the well-known and widely applied *in situ* cosmogenic method (Cockburn and Summerfield, 2004), with one major difference. *In situ*-produced cosmogenic nuclides are considered closed systems – once produced, the isotopes reside in mineral lattices. In contrast, meteoric  $^{10}\text{Be}$  is geochemically mobile, moving within the soil complex (Jungers et al., 2009). This mobility implies the potential for downward translocation of meteoric  $^{10}\text{Be}$  within a soil profile and most importantly, homogenization of all meteoric  $^{10}\text{Be}$  delivered to the soil, including that delivered by rainfall, as dryfall, and in aeolian dust. Such homogenization in soils is critical to consider because it means that both

primary and recycled components of the meteoric  $^{10}\text{Be}$  delivery flux must be estimated before  $^{10}\text{Be}$  concentrations in soils can be interpreted accurately.

In order to infer either an age or an erosion rate from a measured meteoric  $^{10}\text{Be}$  inventory, the total meteoric  $^{10}\text{Be}$  deposition rate over time must be known. This is analogous to production rates used for interpreting *in situ* cosmogenic data (Clark et al., 1995). Early workers estimated meteoric  $^{10}\text{Be}$  deposition rates based on short-term measurements of  $^{10}\text{Be}$  in contemporary precipitation (Brown et al., 1989; Monaghan et al., 1986; Raisbeck et al., 1981). These workers conceived the problem in terms of a “global average” that might be applied universally. More recently, workers have modeled atmospheric production rates of meteoric  $^{10}\text{Be}$  and used general circulation models to estimate local primary meteoric  $^{10}\text{Be}$  deposition, focusing on deposition in ice sheets (Field et al., 2006; Heikkilä et al., 2008b). Although long-term variations in meteoric  $^{10}\text{Be}$  deposition in ice and sediment have been widely considered (Finkel and Nishiizumi, 1997; Frank et al., 1997), terrestrial soils have not yet been formally considered as an archive of meteoric  $^{10}\text{Be}$  deposition.

In this paper, we consider geologic rates of meteoric  $^{10}\text{Be}$  delivery as a function of latitude, precipitation rate, and time. We do this by both synthesizing short-term measurements of meteoric  $^{10}\text{Be}$  in precipitation, and by comparing these results to long-term rates of meteoric  $^{10}\text{Be}$  deposition inferred from marine and terrestrial archives. Such calibration of long-term meteoric  $^{10}\text{Be}$  delivery rates to soils is critical for improving the accuracy and precision of meteoric  $^{10}\text{Be}$  when it is applied as a chronometer or as a monitor of Earth surface processes such as erosion.

## 2. SHORT-TERM METEORIC $^{10}\text{Be}$ DELIVERY

To gauge short-term total meteoric  $^{10}\text{Be}$  deposition, the isotope's concentration in precipitation collectors has been measured at a range of locations in mid to low latitudes (Belmaker et al., 2008; Brown et al., 1992; Brown et al., 1989; Graham et al., 2003; Heikkilä et al., 2008a; Maejima et al., 2005; Monaghan et al., 1986; Raisbeck et al., 1981; Somayajulu et al., 1984). Collection periods range from several months to more than 7 years (Heikkilä et al., 2008a). In order to infer primary meteoric  $^{10}\text{Be}$  deposition from these measurements, the contribution of the recycled component must be estimated. This estimate is performed through the measurement of a secondary isotope such as  $^{238}\text{U}$  or  $^7\text{Be}$ .

### 2.1 Methods to Correct for “Recycled” $^{10}\text{Be}$

The first estimates of recycled  $^{10}\text{Be}$  were made by Monaghan and others (Monaghan et al., 1986) who estimated a global meteoric  $^{10}\text{Be}$  deposition rate from measurements taken at seven stations in the continental United States. They used the flux of  $^{238}\text{U}$  in precipitation to quantify recycled  $^{10}\text{Be}$  by measuring the concentrations of  $^{238}\text{U}$  in local soils. They assumed a uniform meteoric  $^{10}\text{Be}$  content in terrestrial dust ( $5 \cdot 10^8$  atoms/g (Monaghan et al., 1986)) and implicitly assumed that most dust was locally derived. The approach is therefore vulnerable to both uncertainty and variability in the  $^{238}\text{U}$  and meteoric  $^{10}\text{Be}$  content of the soils reworked in dust formation.

Other authors have used  $^7\text{Be}$  rather than  $^{238}\text{U}$  as a control on the recycled component of meteoric  $^{10}\text{Be}$  flux (Brown et al., 1989; Graham et al., 2003).  $^7\text{Be}$  is a cosmogenic isotope with a half life of approximately 53.7 days (Huh, 1999); because of the short half-life, little to none of the  $^7\text{Be}$  fallout is recycled. Precipitation samples with anomalously high  $^{10}\text{Be}/^7\text{Be}$  ratios therefore contain significant recycled meteoric  $^{10}\text{Be}$ . In a two-year study of  $^{10}\text{Be}$  fallout in New Zealand, Graham and others (2003) corrected for dust contamination by assuming that months with low dust/rainfall ratios represented conditions where the recycled meteoric  $^{10}\text{Be}$  contribution was minimal. They then estimated primary meteoric  $^{10}\text{Be}$  fallout by normalizing the meteoric  $^{10}\text{Be}$  values to the  $^{10}\text{Be}/^7\text{Be}$  ratios measured in low dust samples.

In a recent review, Willenbring and von Blanckenburg (2010) reinterpret Graham and others' (2003) data. They find that as precipitation increases, the concentration of  $^{10}\text{Be}$  in rain decreases according to the formula  $A/X + B$ , where  $X$  is rainfall. They interpret  $A$  as the primary component and  $B$  as the recycled component of meteoric  $^{10}\text{Be}$  deposition. This interpretation implies that primary meteoric  $^{10}\text{Be}$  flux is uniform regardless of precipitation and that total recycled  $^{10}\text{Be}$  flux increases in proportion to precipitation. However, in recent precipitation studies from Switzerland and New Zealand (Graham et al., 2003; Heikkilä et al., 2008a), the same inverse linear correlation also describes the relationship between precipitation and  $^7\text{Be}$  concentration (Figure 1). Due to  $^7\text{Be}$ 's short half life, there is no significant recycled component in  $^7\text{Be}$  deposition. Therefore, the uniform ( $B$ ) term cannot represent a recycled component in the  $^7\text{Be}$  relationship. Furthermore, as recycled  $^{10}\text{Be}$  is sourced from airborne dust (Baumgartner

et al., 1997), Willenbring and von Blanckenburg's interpretation (2010) implies that dust flux increases proportionately with rainfall and that dust concentration in rain would be uniform. However, the dust concentrations measured in the New Zealand data show dust per unit precipitation is more than three orders of magnitude greater in the driest months than it is in the wettest months, with dust concentrations being strongly and negatively controlled by precipitation (Graham et al., 2003).

We propose an alternative model for estimating the proportion of primary and recycled meteoric  $^{10}\text{Be}$  fluxes where both  $^{10}\text{Be}$  and  $^7\text{Be}$  are measured. As noted above,  $^7\text{Be}$  concentration in precipitation relates to total precipitation according to an  $A/X+B$  model, where  $X$  is precipitation. Here,  $A$  is interpreted as a dry component of  $^7\text{Be}$  flux that is uniform regardless of precipitation, and  $B$  as a wet component of  $^7\text{Be}$  flux, directly proportional to precipitation (Figure 1). Analogous dry and wet components of primary meteoric  $^{10}\text{Be}$  flux can be estimated if the atmospheric ratio between  $^{10}\text{Be}$  and  $^7\text{Be}$  is known (c.f. Brown et al., 1989). The total meteoric  $^{10}\text{Be}$  flux per unit precipitation can then be calculated from the primary meteoric  $^{10}\text{Be}/^7\text{Be}$  ratio ( $R$ ), the  $^{10}\text{Be}$  concentration in captured dust ( $Q_d$ ), and the concentration of dust per unit precipitation ( $C_d$ ) according to the formula:

$$^{10}\text{Be}_{\text{concentration}} = (^7\text{Be}_{\text{dry}}/X + ^7\text{Be}_{\text{wet}}) \cdot R + Q_d \cdot C_d \quad (1)$$

The first term of this equation represents primary meteoric  $^{10}\text{Be}$  deposition and the second term represents recycled meteoric  $^{10}\text{Be}$  deposition.

In analyzing the New Zealand data (Graham et al., 2003), the  $^7\text{Be}$  fluxes and the dust per unit precipitation ( $C_d$ ) are known, but the primary meteoric  $^{10}\text{Be}/^7\text{Be}$  ratio ( $R$ )

and the  $^{10}\text{Be}$  concentration in captured dust ( $Q_d$ ) are unknown. We therefore model values for these two unknown parameters to best match the meteoric  $^{10}\text{Be}$  and dust concentration data (Figure 2). In this model, neither the  $^7\text{Be}$  flux, the primary meteoric  $^{10}\text{Be}$  flux, nor the  $^{10}\text{Be}$  concentration in dust are treated as uniform. Measured concentrations of  $^{10}\text{Be}$  and  $^7\text{Be}$  increase in the upper atmosphere, where residence times are longer and production rates higher, the  $^{10}\text{Be}/^7\text{Be}$  ratio also increases due to the decay of  $^7\text{Be}$  over the longer residence time (Jordan et al., 2003). Seasonal variations in both  $^7\text{Be}$  and  $^{10}\text{Be}$  concentrations in aerosols and in the isotope ratio are observed at mid and high latitudes (Aldahan et al., 2001; Dibb et al., 1994; Zanis et al., 2003). Such variations are explained by the episodic intrusion of stratospheric air into the troposphere, particularly during the spring relaxation of the jet stream (Aldahan et al., 2001; Dibb et al., 1994; Jordan et al., 2003; Zanis et al., 2003). Recycled  $^{10}\text{Be}$  flux may vary seasonally due to weather and agricultural practices. In the New Zealand data (Graham et al., 2003), distinct summer/spring and fall/winter trends are present and we calculate unique model values for each (Figures 1 and 2). This separate treatment of seasonal trends yields model meteoric  $^{10}\text{Be}$  concentrations in precipitation that closely match the New Zealand data (Figure 3).

Meteoric  $^7\text{Be}$  was also measured in a multi-year study of meteoric  $^{10}\text{Be}$  in Swiss precipitation (Heikkilä et al., 2008a). However, in the Swiss data, precipitation dust concentrations ( $C_d$ ) were not measured. Instead of using equation (1), we vary recycled  $^{10}\text{Be}$  flux by precipitation according to an  $A \cdot X^{-B}$  model, allowing total recycled  $^{10}\text{Be}$  flux to decrease as precipitation increases. All four seasons are modelled separately (Table 1).

The estimated recycled component of meteoric  $^{10}\text{Be}$  deposition varies from 6.2% at the high altitude Jungfraujoch site in Switzerland to 16.1% at Dunedin, New Zealand. Monaghan and others (Monaghan et al., 1986) seven US sites have average recycled meteoric  $^{10}\text{Be}$  contributions amounting to 24% of the total deposited meteoric  $^{10}\text{Be}$ . This difference may be due to Monaghan and others' assumption of a uniform high meteoric  $^{10}\text{Be}$  content in soil. Other workers have made no correction for the recycled component (Brown et al., 1992; Maejima et al., 2005; Somayajulu et al., 1984). As meteoric  $^{10}\text{Be}$  dust is primarily sourced either from arid regions or soils impacted by human activity, Maejima and others' (2005) measurements from Kikai Island, Rukuyu Islands, Japan may have little dust contribution due to the island's oceanic location, but Somayajulu and others' (1984) measurements from 9 stations in India likely include significant but unquantified recycled  $^{10}\text{Be}$  flux.

## **2.2 Rainfall and Latitude Dependence**

At mid and low latitudes, primary meteoric  $^{10}\text{Be}$  flux strongly correlates to precipitation, both in periodic comparison at a single site (Brown et al., 1992; Graham et al., 2003; Heikkilä et al., 2008a; Maejima et al., 2005; Raisbeck et al., 1981; Somayajulu et al., 1984) and when multiple sites are compared against each other (Figure 4). When multiple sites are compared, a tight correlation ( $R^2 > 0.9$ ) between precipitation and primary meteoric  $^{10}\text{Be}$  flux is found only if sites are binned by latitude (Figure 4). When can therefore divide dust-corrected low and mid-latitude meteoric  $^{10}\text{Be}$  fallout data by local annual precipitation to derive a precipitation-normalized curve of meteoric  $^{10}\text{Be}$

fallout by latitude (Figure 5). This curve has the same sigmoidal shape as the  $^{10}\text{Be}$  atmospheric production curve, but at values in excess of those modelled for recent solar output (Masarik and Beer, 2009; Nagai et al., 2000; Webber et al., 2007). At first order, values from this latitude curve can be multiplied by average annual precipitation to estimate primary meteoric  $^{10}\text{Be}$  fallout at any mid or low latitude and for any precipitation rate. However, this approach ignores the primary dry component of meteoric  $^{10}\text{Be}$  deposition and therefore may provide a poor estimate in low precipitation regions. In principle, there is also a limit to the degree that precipitation systems can scavenge  $^{10}\text{Be}$ -bearing aerosols from low latitude, low production regions (Brown et al., 1988), though this has not been observed in the extant low-latitude precipitation data (Brown et al., 1992; Somayajulu et al., 1984).

At polar latitudes, meteoric  $^{10}\text{Be}$  deposition does not discernibly vary by latitude and does not appear to be as strongly precipitation-controlled. Meteoric  $^{10}\text{Be}$  deposition has been measured in ice and firn from the Greenland and Antarctic ice sheets (Beer et al., 1984; Beer et al., 1994; Berggren et al., 2009; Heikkilä et al., 2008c; Horiuchi et al., 2007; Pedro et al., 2006; Raisbeck et al., 1990; Steig et al., 1996). These measurements show significant annual variability that appears to be controlled by solar productivity (Beer et al., 1994; Steig et al., 1996), but decadal scale concentration and accumulation averages can be used to assess recent meteoric  $^{10}\text{Be}$  flux. In the combined Greenland and Antarctica data, primary dry and primary wet components of meteoric  $^{10}\text{Be}$  deposition can be distinguished. Recycled meteoric  $^{10}\text{Be}$  from dust is not likely to be significant (Baumgartner et al., 1997). The mixing curve between primary dry and primary wet

meteoric  $^{10}\text{Be}$  deposition indicates that primary dry deposition dominates, with an order of magnitude less primary wet deposition per unit precipitation than is found in the Swiss and New Zealand rains (Figure 6). Both early and recent models suggest that nearly all of the meteoric  $^{10}\text{Be}$  produced in the stratosphere above latitude  $60^\circ$ , where polar vortexes dominate circulation, is deposited at lower latitudes (Heikkilä et al., 2009; Lal and Peters, 1967) This redistribution of polar air may relate to low polar wet meteoric  $^{10}\text{Be}$  deposition.

The sigmoidal fit of the low and mid latitude primary meteoric  $^{10}\text{Be}$  concentration data (Figure 5) can be multiplied by a global latitudinal precipitation curve (Adler et al., 2003) to estimate the total quantity of primary meteoric  $^{10}\text{Be}$  atoms deposited at each latitudinal band (Figure 7). Above latitude  $65^\circ$ , the wet and dry components derived from Figure 6 are used. An interpolation is supposed between latitudes  $49^\circ$  and  $65^\circ$ . The area under this curve estimates total annual primary meteoric  $^{10}\text{Be}$  deposition.

Total primary meteoric  $^{10}\text{Be}$  production can be estimated based on magnetic field strength and solar activity (Masarik and Beer, 2009). 700 MV of solar activity is average for the years 1951-2004 (Usoskin et al., 2005). The area under our data-based deposition curve estimates total meteoric  $^{10}\text{Be}$  production as approximately 6% higher than the 700 MV production curve suggests (Figure 7). However, the deposition curve probably overstates primary meteoric  $^{10}\text{Be}$  deposition at low latitudes, as no dust correction has been applied to that dataset (Somayajulu et al., 1984) and the dilution of meteoric  $^{10}\text{Be}$  deposition in high rainfall events is not considered. This comparison of the latitudinal distribution of  $^{10}\text{Be}$  production at 700 MV solar activity to the latitudinal distribution of

primary meteoric  $^{10}\text{Be}$  deposition confirms the substantial redistribution of polar meteoric  $^{10}\text{Be}$  to mid-latitudes (Figure 7).

Efforts to estimate the latitudinal distribution of meteoric  $^{10}\text{Be}$  deposition from general circulation models (Heikkilä et al., 2009) do not necessarily match our data-based curves (Figures 5 and 7). In particular, these models expect primary meteoric  $^{10}\text{Be}$  concentrations to peak at approximately  $35^\circ$  latitude (Heikkilä et al., 2009), while the data suggest that the mid-latitude meteoric  $^{10}\text{Be}$  concentration peak occurs above  $45^\circ$  latitude (Figure 5). We cannot presently explain this discrepancy.

The curves presented in figures 5-7 provide a first-order estimate of contemporary, primary meteoric  $^{10}\text{Be}$  deposition for any latitude and precipitation rate. Caution should be used in applying figures 5 and 7 to areas of very high or low precipitation as these sites are not represented in the data and could be subject to dilution or domination by primary dry deposition, respectively. The transition zone between the polar and mid-latitude regimes ( $\sim 50\text{-}65^\circ$ ) is likewise poorly represented. Nevertheless, these curves provide a reference against which long-term variation in total meteoric  $^{10}\text{Be}$  deposition can be compared.

### **3. LONG-TERM VARIATION IN METEORIC $^{10}\text{Be}$ DEPOSITION**

Polar ice sheets, ocean sediments, and terrestrial depositional environments such as loess deposits or lake sediments can be analyzed to produce long-term records of total meteoric  $^{10}\text{Be}$  deposition. Variability in such records is controlled by climate, solar

activity, and magnetic field strength. Changing dust flux and concentration of recycled meteoric  $^{10}\text{Be}$  in dust will also affect records where the recycled component is significant.

The concentration of meteoric  $^{10}\text{Be}$  in ice sheets offers an unambiguous measurement of past meteoric  $^{10}\text{Be}$  fallout to precipitation ratios. The corresponding meteoric  $^{10}\text{Be}$  flux depends on ice accumulation estimates derived from the  $\delta^{18}\text{O}$  record (i.e. Finkel and Nishiizumi, 1997). The concentration of meteoric  $^{10}\text{Be}$  in recent annual layers of ice and firn shows control by the solar cycle (Raisbeck et al., 1990), which is strongly expressed at high latitudes due to diminished magnetic field effects (Masarik and Beer, 1999). Central Greenland ice cores (Finkel and Nishiizumi, 1997; Yiou et al., 1997) show mid-Holocene meteoric  $^{10}\text{Be}$  fluxes ~40% higher than recent fluxes in Greenland and Antarctica, which resemble Pleistocene values – suggesting considerable complexity to the climatic control of meteoric  $^{10}\text{Be}$  distribution. The Pleistocene ice core record also shows an approximately two-fold increase in meteoric  $^{10}\text{Be}$  flux around 40 ka, likely corresponding to the Laschamp magnetic field strength anomaly (Yiou et al., 1997).

While early workers attempted to use meteoric  $^{10}\text{Be}$  concentrations in deep ocean sediment to measure sedimentation rates while assuming constant meteoric  $^{10}\text{Be}$  fallout (i.e. Amin et al., 1975), the current practice is to estimate variation in meteoric  $^{10}\text{Be}$  flux over time by estimating sedimentation rates through alternate methods such as linear interpolation from the  $\delta^{18}\text{O}$  record (i.e. Aldahan and Possnert, 1998) or normalization to the values of another isotope, such as  $^{230}\text{Th}$ , the delivery of which is thought to be more uniform over time (i.e. Christl et al., 2003). Meteoric  $^{10}\text{Be}$  flux recorded by ocean sediment cores is controlled by ocean circulation, biological productivity, and boundary

layer scavenging, in addition to primary meteoric  $^{10}\text{Be}$  production and recycled  $^{10}\text{Be}$  deposition in dust (Christl et al., 2003). Because of these diverse controls on deposition rate, deep sea total meteoric  $^{10}\text{Be}$  deposition rates vary between  $0.25 \cdot 10^6$  and more than  $8 \cdot 10^6$  atoms/( $\text{cm}^2 \cdot \text{year}$ ) (Frank et al., 1997).

When the ocean sediment meteoric  $^{10}\text{Be}$  records are compared in a globally averaged stack, meteoric  $^{10}\text{Be}$  flux varies between 90% and 180% of modern values over a 200 ka record (Frank et al., 1997). These variations inversely correlate to changes in paleomagnetic field intensity (Figure 8). The highest paleointensity in the 200 ka record is found in the Holocene (Guyodo and Valet, 1996), which may explain the relatively low Holocene  $^{10}\text{Be}$  flux measured in oceanic sediment cores. However, approximately modern meteoric  $^{10}\text{Be}$  deposition rates are found during the oxygen isotope stage 5 interglacial period (110-130 ka), during which time, paleomagnetic field intensity varied between 40 and 50% of its Holocene value (Figure 8). During oxygen isotope stage 9 at the beginning of the 200 ka record, meteoric  $^{10}\text{Be}$  deposition likewise fell to Holocene values, with paleomagnetic field intensity at  $\sim 50\%$  of modern values. Ocean sediment cores from high latitudes show a trend opposite of the global stacks, with interglacial periods showing higher meteoric  $^{10}\text{Be}$  flux than glacial periods (Eisenhauer et al., 1994; Lao et al., 1992). The ice core record likewise shows higher meteoric  $^{10}\text{Be}$  flux during interglacial periods (Yiou et al., 1997). The consistent low meteoric  $^{10}\text{Be}$  fluxes to ocean sediments during warm periods in Earth history and corresponding high fluxes in polar regions suggest that climate plays a significant role in the global distribution of meteoric

$^{10}\text{Be}$  deposition over long timescales. This climate effect seems to often supersede the effects of paleomagnetic field intensity.

The most extensively studied terrestrial geologic archives of meteoric  $^{10}\text{Be}$  deposition are the loess deposits of central China. Alternating sequences of loess and paleosols comprise a record of meteoric  $^{10}\text{Be}$  deposition over the past 2.5 million years (Gu et al., 1996). Meteoric  $^{10}\text{Be}$  flux over the period of record averages  $4.2 \cdot 10^6$  atoms/( $\text{cm}^2 \cdot \text{yr}$ ) (Gu et al., 1996), though a large component of this deposition originates from recycled dust. Zhou and others (Zhou et al., 2007) use the correlation between meteoric  $^{10}\text{Be}$  concentration and magnetic susceptibility to disentangle the recycled  $^{10}\text{Be}$  flux from variations in rainfall and primary meteoric  $^{10}\text{Be}$  production in the most recent 80 ka of loess deposits in Luochuan, China. This method assumes that the lowest measured magnetic susceptibility and meteoric  $^{10}\text{Be}$  concentrations represent the values in recycled dust and that these recycled values are uniform over the period of record (Zhou et al., 2007). Variation in meteoric  $^{10}\text{Be}$  correlating to magnetic susceptibility is treated as a precipitation record and other variation is treated as a primary meteoric  $^{10}\text{Be}$  production record (Zhou et al., 2007). These derivative precipitation and primary meteoric  $^{10}\text{Be}$  production records approximately match the speleothem precipitation record and oceanic paleomagnetic intensity record, respectively (Zhou et al., 2007) – illustrating the combined effect of dust flux, precipitation, and magnetic field strength on terrestrial meteoric  $^{10}\text{Be}$  archives. At the Luochuan site, approximately two thirds of the total meteoric  $^{10}\text{Be}$  is sourced from recycled dust (Zhou et al., 2007), indicating that in certain environments recycled meteoric  $^{10}\text{Be}$  will significantly affect depositional flux.

Because long-term changes in climate, dust-flux, and magnetic field intensity can affect total meteoric  $^{10}\text{Be}$  delivery rates, the long-term delivery of meteoric  $^{10}\text{Be}$  to a specific site cannot be accurately estimated from measurements in contemporary rainfall alone. The accuracy of any local total meteoric  $^{10}\text{Be}$  delivery rate estimate will be improved when such estimates are calibrated using a site-specific meteoric  $^{10}\text{Be}$  inventory preserved in a dated long-term record. Though ice and sediment inventories provide accurate records of long-term variation in meteoric  $^{10}\text{Be}$  deposition, the meteoric  $^{10}\text{Be}$  delivery mechanisms to these sites typically do not represent terrestrial conditions. Thus, we next consider the long-term record of meteoric  $^{10}\text{Be}$  deposition preserved in dated terrestrial soils.

### 3.1 $^{10}\text{Be}$ Accumulation in Soil Profiles

When rainfall infiltrates into a soil, any meteoric  $^{10}\text{Be}$  is likely to adhere to soil particles where pH exceeds 4 (You et al., 1989). Beryllium subsequently remains mobile in the soil column and will often concentrate in clay-rich B-horizons.

The total meteoric  $^{10}\text{Be}$  inventory in a soil,  $N$ , can be calculated from consecutive depth profile measurements:

$$N = \sum n \cdot \rho_s \cdot l \quad (2)$$

where  $n$ ,  $\rho_s$ , and  $l$  are the meteoric  $^{10}\text{Be}$  concentration (atoms/gram), the soil density (grams/cm<sup>3</sup>), and the sample length (cm), respectively, of each sample in the profile. If the soil is sufficiently basic for meteoric  $^{10}\text{Be}$  not to be lost to groundwater and erosion is minimal, the total meteoric  $^{10}\text{Be}$  inventory ( $N$ ) equals the total meteoric  $^{10}\text{Be}$

deposition for the duration of soil formation – corrected for loss to decay (Pavich et al., 1986).

In cases where the soil forms from pre-existing sediments, such as fluvial sediments or loess, a portion of the total meteoric  $^{10}\text{Be}$  inventory derives from the soil's parent material and is therefore considered inherited. Two potential methods exist for estimating inheritance: modern sediment can be analyzed and modern concentrations applied to older sediments (Pavich et al., 1986); or sediment unaffected by meteoric  $^{10}\text{Be}$  delivery to the modern soil can be analyzed. Typically such material is identified by a consistent minimum meteoric  $^{10}\text{Be}$  concentration at the bottom of a soil profile (c.f. Anderson et al., 1996). An inherited meteoric  $^{10}\text{Be}$  inventory ( $N_i$ ) can be calculated by multiplying this inheritance concentration by the depth of the entire soil profile.

By assuming a constant meteoric  $^{10}\text{Be}$  deposition rate, past workers have used this inventory method to calculate a minimum soil age (Pavich and Vidic, 1993). Given the regional and seasonal variability in modern  $^{10}\text{Be}$  fallout and the long-term variability of meteoric  $^{10}\text{Be}$  fluxes preserved in ice and sediment records, any assumed meteoric  $^{10}\text{Be}$  deposition rate is vulnerable to uncertainty in long-term regional climate patterns and changes in regional dust flux, as well as variability in atmospheric production.

Conversely, when a soil's age is well-constrained by another method, one can use the meteoric  $^{10}\text{Be}$  inventory to calculate a minimum time-integrated meteoric  $^{10}\text{Be}$  deposition rate over the period of soil formation. Where erosion is known to be minimal and the entire soil profile is sampled, this minimum meteoric  $^{10}\text{Be}$  deposition rate approximates the integrated long-term meteoric  $^{10}\text{Be}$  deposition rate.

This long-term deposition rate (q) is calculated:

$$q=(N-N_i)\cdot\lambda/(1-e^{-\lambda t}) \quad (3)$$

where  $\lambda$  is the decay constant for  $^{10}\text{Be}$  (Nishiizumi et al., 2007) and t is the age of the soil.

#### **4. LONG-TERM METEORIC $^{10}\text{Be}$ DEPOSITION RATES FROM TERRESTRIAL SOILS**

In order to constrain a long-term meteoric  $^{10}\text{Be}$  deposition rate for a soil profile accurately, the soil age, inherited meteoric  $^{10}\text{Be}$  concentration, and soil meteoric  $^{10}\text{Be}$  inventory must be well-constrained, and soil erosion must be minimal. Of the extant meteoric  $^{10}\text{Be}$  soil profiles, few meet these criteria (Graly et al., Submitted). While much of the early work studying meteoric  $^{10}\text{Be}$  in soils focused on fluvial terraces with constrained geologic ages (Pavich et al., 1986; Pavich et al., 1984; Pavich and Vidic, 1993), these age constraints are often too imprecise to estimate a meaningful meteoric  $^{10}\text{Be}$  deposition rate. In other cases, the terraces have been substantially eroded (Pavich et al., 1986).

Using the latitude and rainfall relationships in global precipitation measurements (Figure 4, 6), we can compare these long-term, integrated meteoric  $^{10}\text{Be}$  deposition records with estimates of modern meteoric  $^{10}\text{Be}$  fallout, both total and primary (Table 2). The differences between total meteoric  $^{10}\text{Be}$  inventories and contemporary primary meteoric  $^{10}\text{Be}$  fallout can reflect precipitation changes, changes in primary meteoric  $^{10}\text{Be}$  production, and the addition of recycled meteoric  $^{10}\text{Be}$  to soil profiles by dust deposition.

##### **4.1 New Zealand Profile**

Thus far, only one meteoric  $^{10}\text{Be}$  soil profile has been collected with the specific intention of calibrating a long-term meteoric  $^{10}\text{Be}$  deposition rate (Reusser et al., Submitted). A fluvial terrace bordering the Waipaoa River, New Zealand was sampled deeply enough to reach sediment layers unaffected by meteoric  $^{10}\text{Be}$  deposited during current soil formation (Reusser et al., Submitted). This allows for the estimate of an inherited meteoric  $^{10}\text{Be}$  concentration (c.f. Anderson et al., 1996) and the calculation of a total meteoric  $^{10}\text{Be}$  inventory. A sub-terrace calibrated radiocarbon age of 17.9 ka produces a meteoric  $^{10}\text{Be}$  deposition rate of  $1.70 \cdot 10^6$  atoms/( $\text{cm}^2 \cdot \text{year}$ ).

According to the sigmoidal fit of the global mid to low latitude concentrations of primary meteoric  $^{10}\text{Be}$  in precipitation (Figure 5), the concentration of meteoric  $^{10}\text{Be}$  at the latitude of Waipaoa should be  $\sim 1.9 \cdot 10^4$   $^{10}\text{Be}$  atoms/ $\text{cm}^3$  precipitation. The modern rainfall is approximately 110 cm/yr (Hessell, 1980), suggesting a modern flux of  $2.1 \cdot 10^6$  atoms/( $\text{cm}^2 \cdot \text{year}$ ). The discrepancy between modern primary  $^{10}\text{Be}$  delivery rate and the total meteoric  $^{10}\text{Be}$  inventory suggests that on average, the 18 ka period since terrace formation was drier than present. Lower atmospheric  $^{10}\text{Be}$  production is an unlikely explanation, as the average paleomagnetic field intensity is approximately 18% lower than present over the 18 ka period (Guyodo and Valet, 1996). This inferred dryness is consistent with the suggestion of an ENSO-driven increase in rainfall to the western North Island of New Zealand circa 4 ka before present (Gomez et al., 2004). A long-term meteoric  $^{10}\text{Be}$  deposition rate below modern primary meteoric  $^{10}\text{Be}$  fallout also suggests that very little of the meteoric  $^{10}\text{Be}$  accumulated over the last 17.7 ka was recycled from dust; this inference is consistent with a marine, forested, non-glaciated landscape.

## 4.2 Midwestern Deglacial Profiles

Harden and others' (Harden et al., 2002) meteoric  $^{10}\text{Be}$  profile from an uncultivated prairie ridgetop soil in loess deposits in western Iowa has a minimum calibrated  $^{14}\text{C}$  age of 13.0 ka. Similar to the Waipaoa profile, the meteoric  $^{10}\text{Be}$  concentrations in the Iowa profile decline to a consistent value that can be treated as an inherited meteoric  $^{10}\text{Be}$  concentration (Harden et al., 2002). If the  $^{14}\text{C}$  minimum age approximates the true age of the loess deposit and there has been little to no erosion from the prairie ridgetop, then we can use the total inventory minus inheritance of  $1.73 \cdot 10^{10}$  atoms/cm<sup>2</sup> to estimate a long-term meteoric  $^{10}\text{Be}$  deposition rate of  $1.34 \cdot 10^6$  atoms/(cm<sup>2</sup>·year). Balco's (Balco, 2004) meteoric  $^{10}\text{Be}$  soil profile from glacial sediments in Minnesota has a total inventory minus inheritance of  $1.97 \cdot 10^{10}$  atoms/cm<sup>2</sup>. Using a deglacial age for that region of 15 ka, we estimate a long-term meteoric  $^{10}\text{Be}$  deposition rate of  $1.32 \cdot 10^6$  atoms/(cm<sup>2</sup>·year), nearly identical to the Iowa value.

Our curve of mid-latitude to low-latitude meteoric  $^{10}\text{Be}$  precipitation measurements estimates a primary meteoric  $^{10}\text{Be}$  concentration of approximately  $2.06 \cdot 10^4$  atoms/cm<sup>3</sup> precipitation at 41° latitude (Figure 5). When we normalize for the approximately 80 cm of annual precipitation in western Iowa and 75 cm in central Minnesota, both sites expect a modern meteoric  $^{10}\text{Be}$  flux of approximately  $1.65 \cdot 10^6$  atoms/(cm<sup>2</sup>·year). As with Waipaoa, a good explanation for the mismatch between modern and long-term meteoric  $^{10}\text{Be}$  deposition rates is previous periods of less than modern precipitation. Dust flux is also unlikely to be significant. During the Mid-

Holocene, periods of reduced precipitation are detected by increased salinity in the sediment records of closed-basin lakes in the Eastern Dakotas (Dean and Schwalb, 2000; Haskell et al., 1996; Valero-Garcés et al., 1997). The regional character of these events suggests that for parts of the Holocene, western Iowa and Minnesota may also have experienced reduced rainfall and therefore reduced meteoric  $^{10}\text{Be}$  delivery. However, the loss of meteoric  $^{10}\text{Be}$  to soil erosion cannot be ruled out as an alternative explanation for the less than modern apparent long-term meteoric  $^{10}\text{Be}$  delivery rates in this region.

#### **4.3 Ryukyu Islands, Japan**

Maejima and others (Maejima et al., 2005) measured total meteoric  $^{10}\text{Be}$  inventories in soils developed on six raised coral terraces on Kikai Island in the Ryukyu Islands, Japan. In additional short-term precipitation measurements over a two year period, they found an average  $^{10}\text{Be}$  depositional flux of  $2.75 \cdot 10^6$  atoms/( $\text{cm}^2 \cdot \text{year}$ ), consistent with the high rainfall and subtropical location of the island (Figure 5). The application of this deposition rate to the measured meteoric  $^{10}\text{Be}$  inventories of the raised terraces yields minimum ages discordant with both coral U-Th series dates and topographic chronologies (Maejima et al., 2005). If these meteoric  $^{10}\text{Be}$  inventories are instead interpreted as minimum meteoric  $^{10}\text{Be}$  deposition rates (and the U-Th coral chronology is accepted), long-term depositional averages range  $0.98 \cdot 10^6$  to  $4.1 \cdot 10^6$  atoms/( $\text{cm}^2 \cdot \text{year}$ ) (Table 2). The inherited inventories are estimated by assuming the youngest (5.2 ka) terrace has had a long-term meteoric  $^{10}\text{Be}$  deposition rate equal to the measured modern deposition rate. The difference between the expected and actual

meteoric  $^{10}\text{Be}$  inventories in this terrace establishes an inherited meteoric  $^{10}\text{Be}$  concentration in the coral of  $2.3 \cdot 10^8$  atoms/gram – suggesting that the coral scavenged substantial  $^{10}\text{Be}$  from seawater prior to its emergence and subsequent soil development.

There is a strong possibility of erosional loss in these terrace profiles, due to the extensive sugarcane cultivation on the island. Additionally, the two oldest profiles did not reach unweathered coral (Nagatsuka and Maejima, 2001), and therefore their meteoric  $^{10}\text{Be}$  inventories are minimum approximations of the true soil meteoric  $^{10}\text{Be}$  inventory. Given the potential erosion and under-sampling of these profiles, it is important to stress that these estimates of long-term deposition rates are minima (Table 2). The actual long-term deposition rate is therefore best approximated by the largest observed value of  $4.1 \cdot 10^6$  atoms/( $\text{cm}^2 \cdot \text{year}$ ). Due to a weaker magnetic field, atmospheric  $^{10}\text{Be}$  production was likely, on average, 25% greater than present during the last 80 ka (Frank et al., 1997) (Figure 8), explaining much of the difference between long-term and contemporary meteoric  $^{10}\text{Be}$  deposition on Kikai Island. Substantial loess deposits accumulated in northern China during the 80 ka period (Gu et al., 1996), so paleo dust flux may also contribute to the greater than modern long-term meteoric  $^{10}\text{Be}$  deposition rate. Increased Pleistocene rainfall also cannot be ruled out.

#### **4.4. Alpine Moraines**

A recent study in the Swiss and Italian alps compares meteoric  $^{10}\text{Be}$  inventories in otherwise dated glacial moraines (Egli et al., 2010). The moraines range in age from 3.3 ka to 19.5 ka and soils were collected from pits dug on slopes of 5 to 32% (Egli et al.,

2010). Older alpine soils on significant slopes are unlikely to be minimally eroded (Putkonen and Swanson, 2003), and therefore cannot be used to estimate meaningful long-term meteoric  $^{10}\text{Be}$  deposition rates. Of the six soil profiles, a 3.4 to 3.7 ka soil on a 5% slope is the most likely to have minimal erosion. This soil has a total meteoric  $^{10}\text{Be}$  inventory of  $1.47 \cdot 10^{10}$  atoms/cm<sup>2</sup>, producing an estimated meteoric  $^{10}\text{Be}$  deposition rate of  $4.15 \cdot 10^6$  atoms/(cm<sup>2</sup>·year) from a 3.55 ka age. When this rate is normalized by contemporary mean annual precipitation at the site, the calculated deposition rate is similar to the primary meteoric  $^{10}\text{Be}$  deposition rate at 46° latitude (Table 2). The soil's deposition rate per unit precipitation is also similar to meteoric  $^{10}\text{Be}$  concentrations found in contemporary precipitation at other Swiss sites (Heikkilä et al., 2008a).

## 5. CONCLUSIONS

The deposition of meteoric  $^{10}\text{Be}$  on Earth's surface is neither spatially nor temporally uniform. The concentration of meteoric  $^{10}\text{Be}$  in precipitation is composed of three components: a primary dry component – uniform regardless of precipitation, a primary wet component proportional to precipitation, and a recycled component from terrestrially-sourced dust. The values of the primary components vary both seasonally and by latitude, while the recycled component varies according to the  $^{10}\text{Be}$  content and magnitude of the terrestrially-derived dust flux. Despite these complexities, latitude and average annual precipitation can provide a first-order estimate of the primary meteoric  $^{10}\text{Be}$  flux (Figures 5 and 6). However, this latitude and precipitation-based estimate based on contemporary data does not fully predict local meteoric  $^{10}\text{Be}$  deposition over

geologic time scales. Long-term meteoric  $^{10}\text{Be}$  distribution reflects variability both in total atmospheric production – controlled by magnetic field intensity and solar activity, and in local deposition rate – controlled by climate. The input of recycled  $^{10}\text{Be}$  from dust can also vary over time.

To assess site-specific, long-term total meteoric  $^{10}\text{Be}$  deposition rates, the inventory of meteoric  $^{10}\text{Be}$  retained in a soil profile can be measured. Where the age of the soil is well-constrained by another dating method and erosion is minimal, the meteoric  $^{10}\text{Be}$  inventory can be used to calculate a long-term, integrated rate of meteoric  $^{10}\text{Be}$  deposition. So far, relevant data exist for only a few soil profiles. In these cases, the long-term meteoric  $^{10}\text{Be}$  deposition rates differ somewhat from contemporary deposition rates set by rainfall and latitude. This apparent temporal variation is likely due to long-term changes in site-specific climate patterns, changing primary production of meteoric  $^{10}\text{Be}$  in Earth's atmosphere over time, and the addition of recycled meteoric  $^{10}\text{Be}$  to soils.

Measurements of  $^{10}\text{Be}$  in rainfall, ice, and sediment over three decades indicate significant variability in the distribution of meteoric  $^{10}\text{Be}$  over Earth's surface. Many of the details regarding meteoric  $^{10}\text{Be}$  delivery to terrestrial landscapes remain uncertain. Measurements of  $^{10}\text{Be}$  in precipitation focus mostly on a narrow mid-latitude range, thus high and low latitude measurements – especially if dust-corrected, will be useful in improving assessments of precipitation and latitude effects. Equally useful will be additional measurements of meteoric  $^{10}\text{Be}$  inventories in age-controlled, minimally-eroded soils. These measurements will provide new insight into the long-term variability

of meteoric  $^{10}\text{Be}$  fallout distribution that is important for its application as a chronometer and monitor of Earth surface processes, such as erosion.

### **ACKNOWLEDGEMENTS**

J. Graly was supported to complete this work by National Science Foundation grant ARC-0713956. L. Reusser was supported by the University of Vermont Provost's office.

## Chapter 4 Tables

Table 1. Calculation of recycled  $^{10}\text{Be}$  Flux in Swiss precipitation (Heikkilä et al., 2008a)

Location	$^7\text{Be}$ Flux Model ( $10^4$ atoms/cm $^2$ )		$^{10}\text{Be}$ Flux Model ( $10^4$ atoms/cm $^2$ )			R $^2$	Recycled $^{10}\text{Be}$ Flux %
	Season	Model	Season	Primary	Recycled		
Dübendorf (440 m)	Winter	1.1 + 0.7·precip	Winter	1.96· $^7\text{Be}$	8.3·precip $^{-1.2}$	0.61	7.5%
			Spring	2.44· $^7\text{Be}$	2.2		
	Summer	4.0 + 0.93·precip	Summer	1.96· $^7\text{Be}$	1.4		
			Fall	1.45· $^7\text{Be}$	1.2		
Jungfrauoch (3580 m)	Winter	0.59·precip	Winter	1.82· $^7\text{Be}$	3.1·precip $^{-0.25}$	0.82	6.2%
	Spring	2.1 + 0.68·precip	Spring	2.78· $^7\text{Be}$	11.0·precip $^{-1.3}$		
	Summer	2.7 + 0.74·precip	Summer	2.33· $^7\text{Be}$	0.0		
	Fall	2.2 + 0.42·precip	Fall	1.43· $^7\text{Be}$	2.4		

Table 2. Comparison of modern and long-term meteoric  $^{10}\text{Be}$  deposition rates in dated soils.

First Author	Location	Surface Age (ka)	$^{10}\text{Be}$ Inventory (atoms/cm $^2$ )	Inherited Inventory (atoms/cm $^2$ )	Minimum Long-term Deposition Rate (atoms·cm $^{-2}$ ·yr $^{-1}$ )	Modern Deposition Rate (atoms·cm $^{-2}$ ·yr $^{-1}$ )	Percent Difference (Long-term vs. Modern)
Reusser [60]	Waipaoa, New Zealand	17.9	4.02·10 $^{10}$	9.90·10 $^9$	1.70·10 $^6$	2.09·10 $^6$	-18.5%
Harden [63]	Western Iowa	13.0	3.04·10 $^{10}$	1.30·10 $^{10}$	1.34·10 $^6$	1.68·10 $^6$	-20.3%
Balco [64]	Minnesota	15.0	2.70·10 $^{10}$	7.29·10 $^9$	1.32·10 $^6$	1.64·10 $^6$	-19.7%
Maejima [27]	Kikai Island, Japan	45	5.10·10 $^{10}$	7.40·10 $^9$	9.80·10 $^5$	2.88·10 $^6$	-66.0%*
Maejima [27]	Kikai Island, Japan	60	1.53·10 $^{11}$	1.16·10 $^{10}$	2.39·10 $^6$	2.88·10 $^6$	-16.9%*
Maejima [27]	Kikai Island, Japan	80	3.40·10 $^{11}$	1.85·10 $^{10}$	4.10·10 $^6$	2.88·10 $^6$	42.4%*
Maejima [27]	Kikai Island, Japan	100	3.63·10 $^{11}$	1.97·10 $^{10}$	3.52·10 $^6$	2.88·10 $^6$	22.3%*
Maejima [27]	Kikai Island, Japan	125	2.75·10 $^{11}$	2.08·10 $^{10}$	2.10·10 $^6$	2.88·10 $^6$	-27.1%*
Elgi [69]	Swiss Alps	3.55	1.47·10 $^{10}$	0	4.15·10 $^6$	4.49·10 $^6$	-7.5%

\*Due to likely erosion and incomplete sampling at Maejima and others' sites, the highest measured minimum long-term deposition rate is considered the best approximation of the true long-term deposition rate.

## Chapter 4 Figures

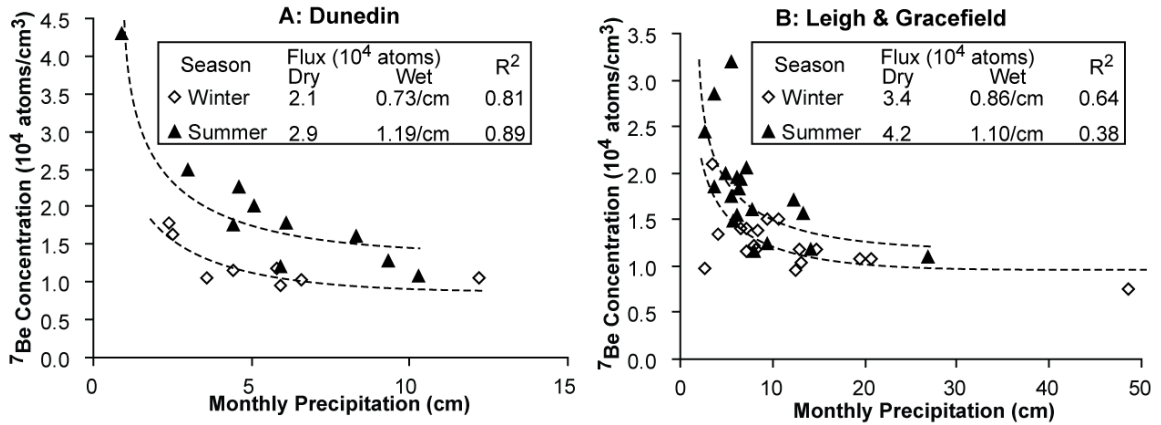


Figure 1: Mixing between dry and wet components in meteoric  $^7\text{Be}$  deposition in monthly  $^7\text{Be}$  measurements in New Zealand precipitation (Graham et al., 2003). The  $^7\text{Be}$  concentration in precipitation is derived from wet and dry  $^7\text{Be}$  flux components by  $^7\text{Be}_{\text{dry}}/\text{precipitation} + ^7\text{Be}_{\text{wet}}$  (dashed lines). Dunedin data (A) are modelled separately from Leigh and Gracefield sites (B). Fall/winter and spring/summer months are likewise modelled separately.

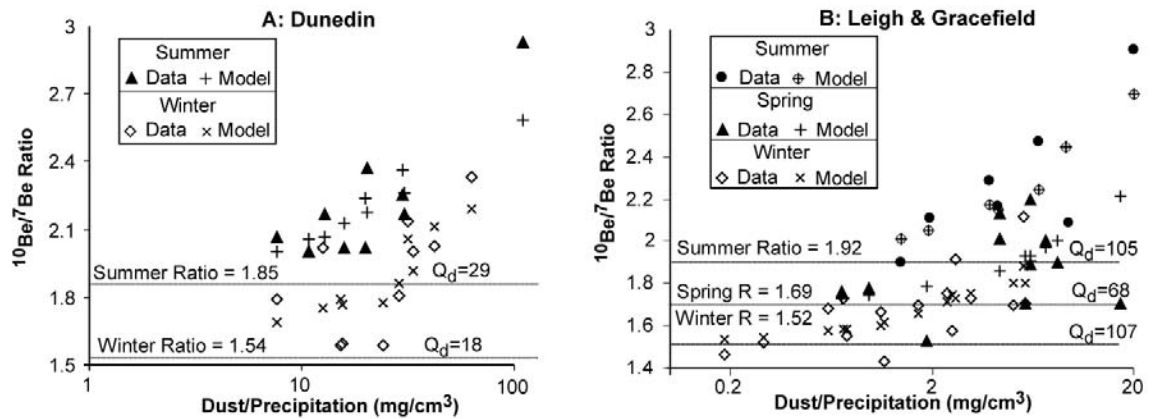


Figure 2: Control of dust flux on the ratio of meteoric  $^{10}\text{Be}/^7\text{Be}$  in New Zealand data (Graham et al., 2003). Model meteoric  $^{10}\text{Be}$  concentrations are calculated from model  $^7\text{Be}$  values (Figure 1) based on a seasonally variable primary  $^{10}\text{Be}/^7\text{Be}$  ratio (R) and concentration of meteoric  $^{10}\text{Be}$  in captured dust in atoms/mg ( $Q_d$ ). At Dunedin (A), fall/winter and spring/summer months are modelled separately. In the Leigh and Gracefield data (B), spring, summer, and fall/winter months are modelled separately.

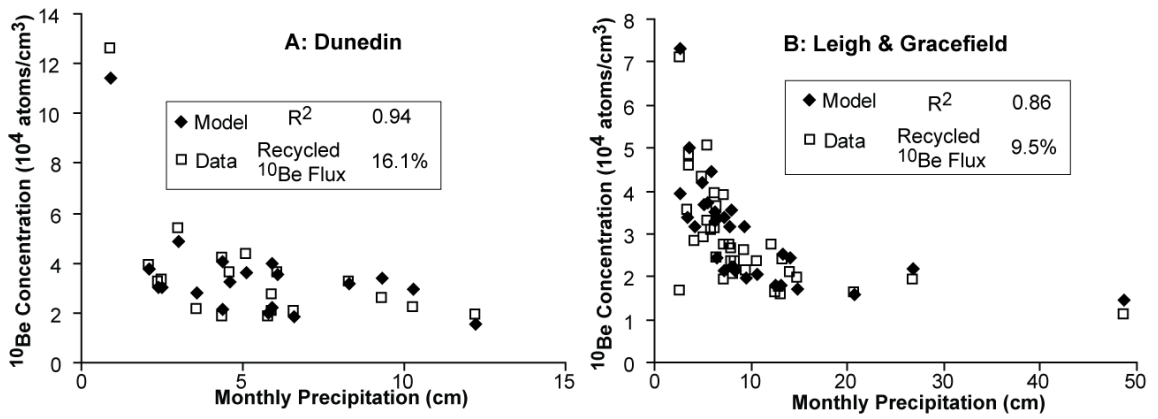


Figure 3: Model <sup>7</sup>Be values (Figure 1) multiplied by model <sup>10</sup>Be/<sup>7</sup>Be ratios (Figure 2) are added to recycled <sup>10</sup>Be concentrations to predict total meteoric <sup>10</sup>Be concentrations. The total inferred recycled meteoric <sup>10</sup>Be flux is also shown. Dunedin (A) and Leigh and Gracefield (B) are treated separately.

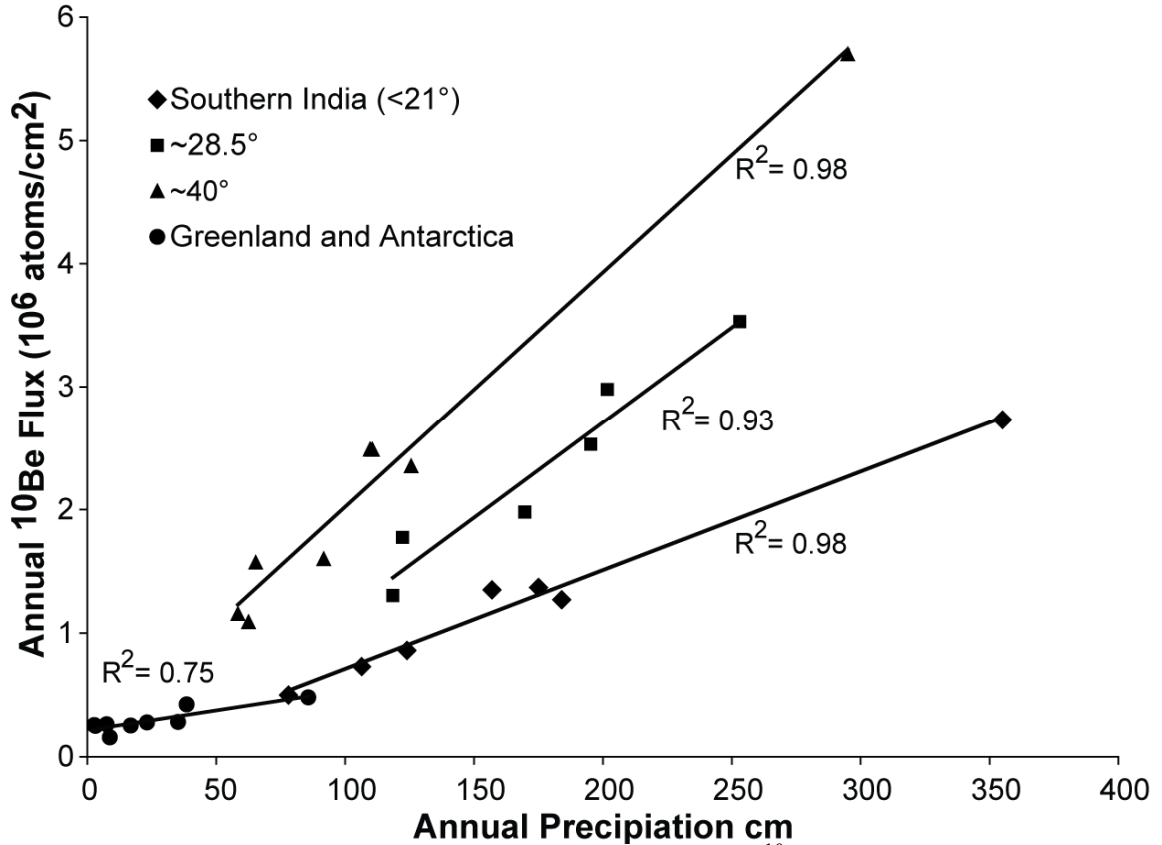


Figure 4: Strong precipitation control on primary meteoric <sup>10</sup>Be flux is shown in diverse global data. Southern India data is from Somayajulu and others (Somayajulu et al., 1984). The subtropical curve (28.5°) combines data from Kikai Island (Maejima et al., 2005) and stations in the southern United States (Monaghan et al., 1986), Somayajulu and others' northern India data (Somayajulu et al., 1984) are excluded due to likelihood of significant dust and thus recycled meteoric <sup>10</sup>Be contribution. The mid-latitude curve (40°) is from dust-corrected New Zealand and North American data (Graham et al., 2003; Monaghan et al., 1986). Antarctic and Greenland data come from snow and ice accumulation and meteoric <sup>10</sup>Be concentration measurements from recent layers (Beer et al., 1984; Beer et al., 1994; Berggren et al., 2009; Heikkilä et al., 2008c; Horiuchi et al., 2007; Pedro et al., 2006; Raisbeck et al., 1990; Steig et al., 1996).

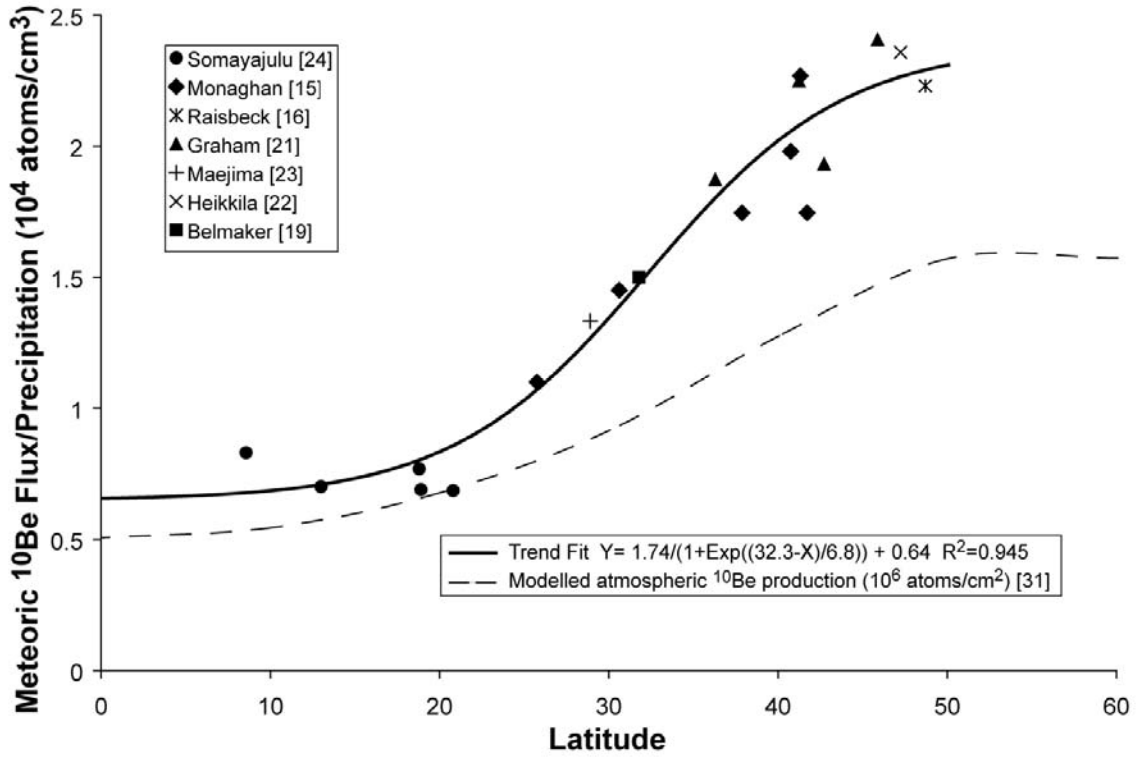


Figure 5: The latitudinal trend in meteoric <sup>10</sup>Be flux per unit precipitation data is compared to atmospheric production rates (Masarik and Beer, 2009). The atmospheric dust component is subtracted from the Graham, Monaghan, and Heikkilä data. The Jungfraujoch data (Heikkilä et al., 2008a) are not included, as the high altitude of the station makes it non-representative. The atmospheric production curve is for solar activity of 700 MV (Masarik and Beer, 2009).

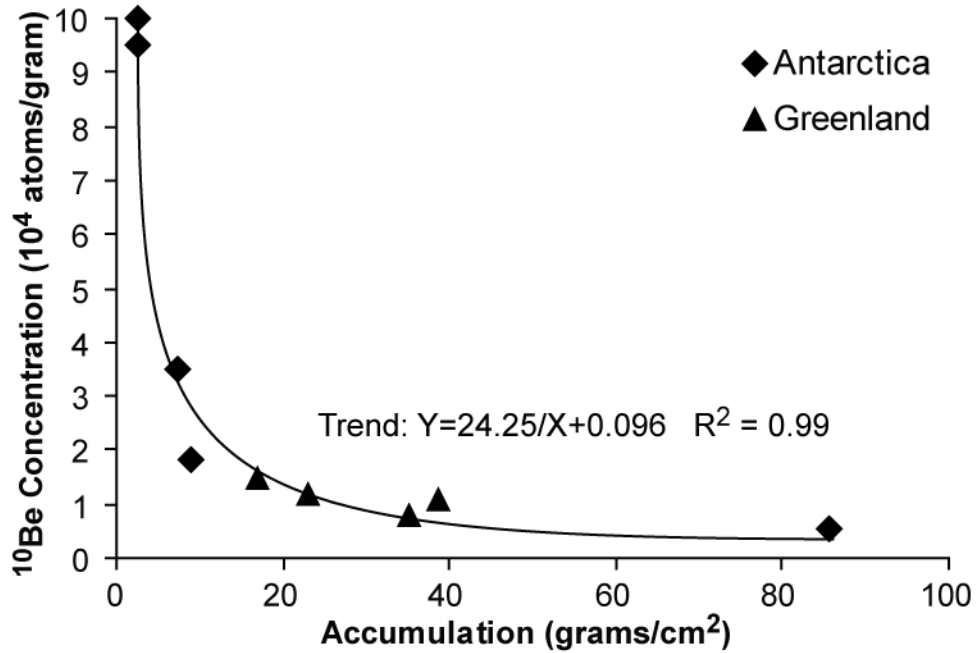


Figure 6: Accumulation of snow and ice versus meteoric  $^{10}\text{Be}$  concentration in recent Antarctic and Greenland measurements show a consistent polar mixing curve between dry and wet meteoric  $^{10}\text{Be}$  deposition. When compared to primary dry and wet meteoric  $^{10}\text{Be}$  deposition in Swiss and New Zealand precipitation measurements (Figures 1 and 2, Table 1), total polar dry meteoric  $^{10}\text{Be}$  deposition is a factor 5 higher and total polar wet meteoric  $^{10}\text{Be}$  deposition is an order of magnitude lower.

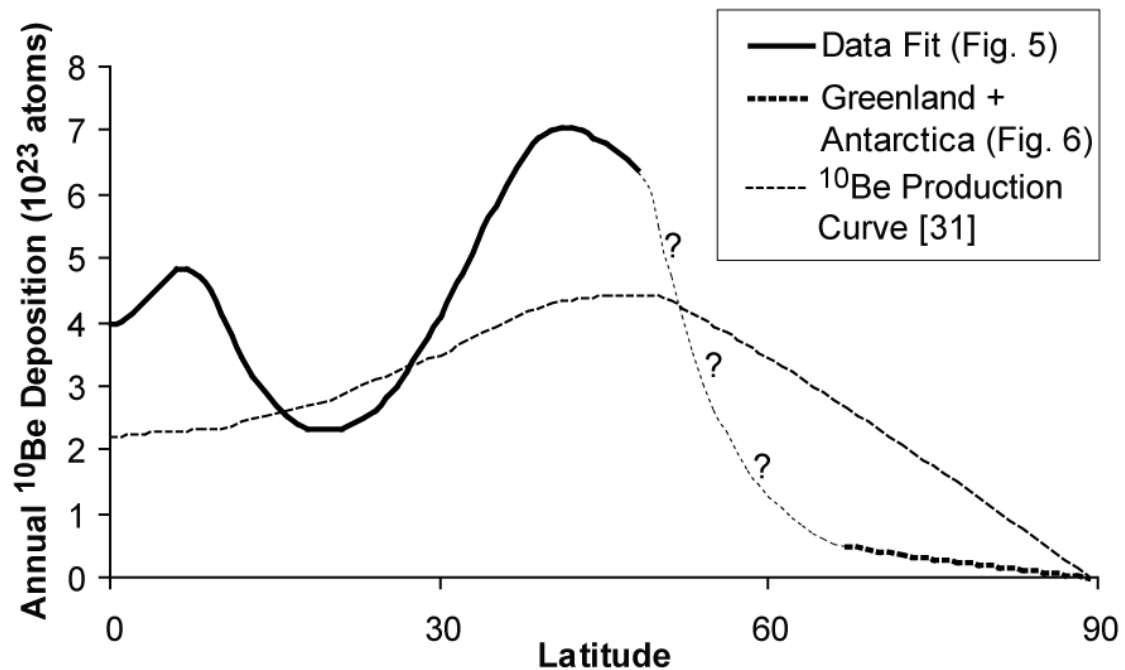


Figure 7: The meteoric  $^{10}\text{Be}$  concentration fit from Figure 6 is multiplied by a latitudinal rainfall model (hemispheres averaged) (Adler et al., 2003) and by the area of each latitudinal band to estimate total annual  $^{10}\text{Be}$  deposition. Above latitude  $65^\circ$ , deposition is estimated using the fit from snow and ice accumulation data (Figure 5). No data exist between latitudes  $49^\circ$  and  $65^\circ$ , so an interpolation is supposed. The atmospheric production curve for a solar activity of 700 MV (Masarik and Beer, 2009) is plotted for comparison, showing the redistribution of polar meteoric  $^{10}\text{Be}$  production to lower latitudes.

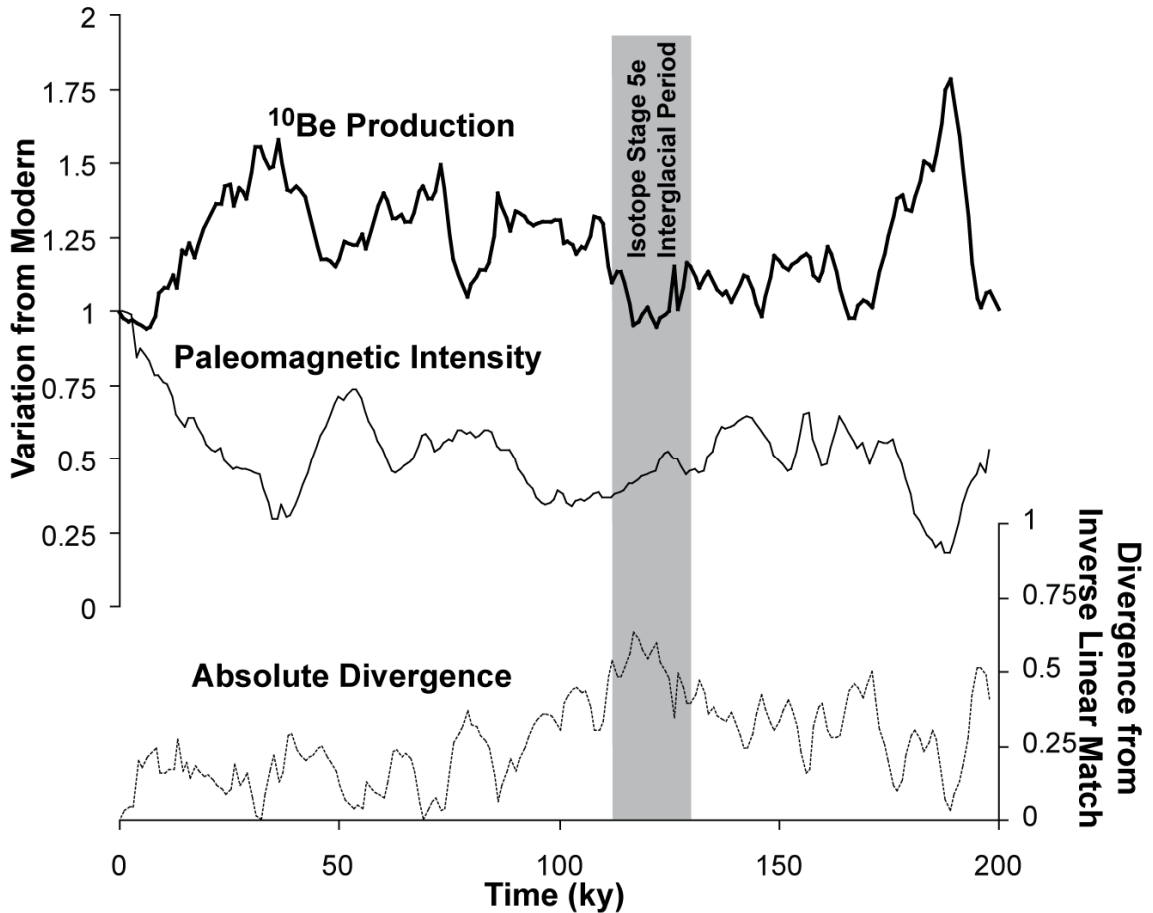


Figure 8: Relative variation in meteoric  $^{10}\text{Be}$  concentrations in sea sediments (globally averaged stack) is treated as a proxy for relative meteoric  $^{10}\text{Be}$  production (Frank et al., 1997) and compared to similarly-derived relative variation in paleomagnetic field intensity (Guyodo and Valet, 1996). Relative paleomagnetic field intensity is an inverse predictor of relative meteoric  $^{10}\text{Be}$  production. The absolute divergence between inverse relative meteoric  $^{10}\text{Be}$  production and relative paleomagnetic field intensity is also shown. This divergence is greatest during the Eemian interglacial period, suggesting that climate plays a significant role in meteoric  $^{10}\text{Be}$  delivery to ocean sediments.

## Chapter 5: Meteoric $^{10}\text{Be}$ evidence for past interglacial ice sheet retreat in western Greenland

(submitted as a separate paper to *Nature*)

Abstract: The influence of climate change on large ice sheets is often understood through the study of their response to past climate forcings. Global records of past ice volume predict several recent periods during which Earth was less glaciated than present (Bitanja and van de Wal, 2008; Lisiecki and Raymo, 2005), but the behavior of individual ice sheets during these periods remains poorly constrained. Modeling suggests that during warm interglacial periods the retreat of the Greenland Ice Sheet substantially contributed to global ice volume and sea-level change (Huybrechts, 2002; Otto-Bliesner et al., 2006), however empirical evidence of these retreats is limited to boreal forest type biomarkers in arctic sediment (Funder et al., 1985; Willerslev et al., 2007) and some discordant exposure ages in Holocene glacial detritus (Goehring et al., 2010). In order to directly test whether presently glaciated areas of Greenland were previously exposed during past ice sheet retreats, we measured a rare isotope, meteoric  $^{10}\text{Be}$ , in sediment entrained in ice, transported to the ice sheet's margin by glacial flow. Because meteoric  $^{10}\text{Be}$  is formed in the atmosphere and deposited in surface soils, this ice-bound sediment could only have acquired meteoric  $^{10}\text{Be}$  during periods when the Greenland Ice Sheet's extent was smaller than present. Therefore, the high concentrations of meteoric  $^{10}\text{Be}$  observed in ice-bound sediment indicate low subglacial erosion rates and substantial surface exposure of interior Greenland during past interglacial periods, suggesting that loss of ice in Greenland was indeed significant during past high sea-level events.

The global glacial ice volumes reconstructed from benthic carbonate oxygen isotopes show a pattern of cyclic oscillation between glacial and interglacial periods extending ~2.7 Ma, with ice volumes typically far greater than today's (Bitanja and van de Wal, 2008; Lisiecki and Raymo, 2005). According to this record, the modern global ice volume minimum has been exceeded for only ~30,000 of the past 2.1 million years (Bitanja and van de Wal, 2008). Models suggest that substantial melting of the Greenland Ice Sheet has influenced these past sea-level high stands (Huybrechts, 2002; Otto-Bliesner et al., 2006) and that the Greenland Ice Sheet will drive sea-level rise as global warming continues (Alley et al., 2005). Climate sensitivity is indicated in Holocene sediment and geochronology data that show that the Greenland Ice Sheet retreated past its present margins several millennia prior to the complete disappearance of other northern hemisphere ice masses (Weidick et al., 1990; Young et al., 2010). Earlier periods of ice sheet retreat are also suggested by the presence of boreal-forest pollen in offshore sediments in northern Greenland (Funder et al., 1985) and in sub-ice sediment in southern Greenland (Willerslev et al., 2007), and from inherited cosmogenic isotopes are present in Holocene glacial fluvial material (Goehring et al., 2010) and in a single sub-ice rock sample collected below the GISP2 ice core (Nishiizumi et al., 1996).

To further constrain the Greenland Ice Sheet's retreat history during past interglacials, we measured concentrations of meteoric  $^{10}\text{Be}$  in ice-bound silt and sand at the margin of the Greenland Ice Sheet. This sand and silt is derived from the erosion of the soil, sediment, and rock that forms the ice sheet's bed. Because meteoric  $^{10}\text{Be}$  forms in the upper atmosphere, is primarily deposited in precipitation (Lal and Peters, 1967),

and strongly adsorbs to sediment (Pavich et al., 1984), the meteoric  $^{10}\text{Be}$  content of the sampled material is a proxy for the duration of ice-free surface exposure. During glacial times,  $^{10}\text{Be}$ -bearing aerosols are deposited on the ice sheet; thus, meteoric  $^{10}\text{Be}$  in the basal ice-bound sediment can only accumulate during interglacial surface exposure.

We collected ice-bound fine sediment from the ice sheet margin at three locations in western Greenland: Kangerlussuaq (67.1° N, n=10), Ilulissat (69.4° N, n=8), and Upernavik (72.6° N, n=16) (Figure 1). Meteoric  $^{10}\text{Be}$  was isolated through total fusion of the sediment (Stone, 1998), and its concentration measured by accelerator mass spectrometry.  $\delta^{18}\text{O}$  and  $\delta^2\text{H}$  were measured in the surrounding ice to determine the global and local climate conditions when the ice formed (Johnsen et al., 1989).

In 34 ice-bound sediment samples, meteoric  $^{10}\text{Be}$  concentrations vary from  $1.8 \cdot 10^6$  to  $2.1 \cdot 10^8$  atoms $\cdot\text{g}^{-1}$ , with an average of  $2.9 \cdot 10^7$  atoms/g (Figure 1). Comparing between field sites, an unequal variance t-test shows meteoric  $^{10}\text{Be}$  concentrations to be significantly lower at Kangerlussuaq, the southernmost site ( $p=0.03$ ). The ranges of meteoric  $^{10}\text{Be}$  concentrations at the two northern sites are not statistically distinguishable. Kangerlussuaq is located on the Greenland Ice Sheet's Southern Dome, which may be significantly more responsive to climate than the northern Main Dome (Otto-Bliesner et al., 2006).

In temperate mid-latitude soils, there is a strong correlation ( $R^2=0.92$ ) between maximum measured  $^{10}\text{Be}$  concentration and total  $^{10}\text{Be}$  inventory (Graly et al., Submitted). Conservatively assuming that the highest-measured meteoric  $^{10}\text{Be}$  value at each sampling site represents the maximum meteoric  $^{10}\text{Be}$  concentration in source soils for that site, this

correlation allows estimation of the total meteoric  $^{10}\text{Be}$  inventory in the source soils of each of the 3 sites (Figure 2). While the lack of arctic meteoric  $^{10}\text{Be}$  soil measurements necessitates estimation from mid-latitude soils, the correlation is robust ( $n=57$ )(Graly et al., Submitted).

To convert a total meteoric  $^{10}\text{Be}$  inventory to a soil age corresponding to surface exposure duration, a meteoric  $^{10}\text{Be}$  deposition rate must be known. Meteoric  $^{10}\text{Be}$  deposition rates in the interior of Greenland are well-constrained by measurements of  $^{10}\text{Be}$  in ice cores (Finkel and Nishiizumi, 1997). As deposition rates from the mid-Holocene are the most likely to represent conditions during earlier interglacial periods, a value of  $3.5 \cdot 10^5 \text{ atoms} \cdot \text{cm}^{-2} \cdot \text{yr}^{-1}$  is applied here. This deposition rate and the root means square error of 1.41 in the conversion between maximum concentration and inventory (Graly et al., Submitted) generate soil ages of 60-122 ka at Upernavik ( $72.6^\circ \text{ N}$ ), 39-78 ka at Ilulissat ( $69.4^\circ \text{ N}$ ), and 9-18 ka at Kangerlussuaq ( $67.1^\circ \text{ N}$ ).

These ages alone do not constrain the duration of Greenland's interglacial periods. Meteoric  $^{10}\text{Be}$  accumulating during each of several Late Pliocene and Pleistocene interglacial periods and prior to glaciation all may have contributed to the total meteoric  $^{10}\text{Be}$  inventory at modern sediment source sites. The soil age is controlled by meteoric  $^{10}\text{Be}$  accumulation during of each of these periods, minus meteoric  $^{10}\text{Be}$  lost to glacial period erosion and decay over  $^{10}\text{Be}$ 's half-life of  $1.39 \cdot 10^6$  years (Korshinek et al., 2010). Constraint on interglacial period duration is therefore possible only if glacial erosion rates are known.

Sediment volumes in southern Greenland fjords suggest Holocene glacial erosion rates of  $\sim 10$  m/My (Andrews et al., 1994). Contemporary sediment fluxes in the Kangerlussuaq area are  $\sim 20 \text{ m}^3 \text{ m}^{-1} \text{ a}^{-1}$ , suggesting  $\sim 60$  m/My of subglacial erosion if sediment is evenly and steadily sourced over the 340 km flowline (though such conditions are unlikely) (Knight et al., 2002). Erosion and sediment flux data are absent at the northern sites. Given these uncertainties, we do not estimate interglacial exposure from a prescribed erosion rate, but model a set of interglacial exposure lengths and matching erosion rates, all of which potentially explain the meteoric  $^{10}\text{Be}$  data.

We model the meteoric  $^{10}\text{Be}$  accumulation during interglacial periods based on Bitanja and van de Wal's (Bitanja and van de Wal, 2008) estimates of Late Pliocene and Pleistocene global ice volumes, allowing Greenland's interglacial periods to begin and end at specified sea-level equivalents. To compare model simulations, the lengths of interglacial periods are corrected for the loss of  $^{10}\text{Be}$  to decay and summed. Interglacial period meteoric  $^{10}\text{Be}$  deposition and glacial period erosion of subglacial material are assumed to be temporally and spatially uniform. While the meteoric  $^{10}\text{Be}$  content of wind-blown dust can be substantial (Baumgartner et al., 1997), net dust flux is assumed to be zero, because most dust would be both sourced and deposited within Greenland.

Prior to the onset of Northern Hemisphere glaciation  $\sim 2.7$  Ma ago (Bitanja and van de Wal, 2008), Greenland's surface likely developed a regolith zone that may have been tens of meters deep (Lidmar-Bergström, 1997). The meteoric  $^{10}\text{Be}$  inventory of this regolith zone was estimated assuming meteoric  $^{10}\text{Be}$  deposition equaled meteoric  $^{10}\text{Be}$  loss to erosion and isotope decay (Brown et al., 1988). The resulting inventory value

varies depending on pre-glacial erosion rate. Erosion rates in dry, passive margin, continental environments vary between 2 and 10 m/My (Bierman and Caffee, 2001), with resulting pre-glacial meteoric  $^{10}\text{Be}$  inventories varying within a factor of four. If erosion rates are low enough that pre-glacial sediments remain beneath the glacial bed, their contribution to contemporary sub-glacial meteoric  $^{10}\text{Be}$  inventories may be substantial (Figure 3).

The model results are also sensitive to the rate of glacial sediment transport. Under uniform subglacial erosion conditions, eroded sediments are initially replaced by similar material sourced up flowline. This creates a temporal lag between the onset of glaciation and the effect of glacial erosion on the meteoric  $^{10}\text{Be}$  inventory of subglacial sediments (Figure 3). Depending on basal topography and ice dynamics, the contemporary transport speed of ice-entrained sediment along the flowlines of the three West Greenland sites varies between 2-30 m/yr, averaging  $\sim 8$  m/yr (Wang et al., 2002). This slow rate of basal ice movement is supported by Pleistocene-aged  $\delta^{18}\text{O}$  and  $\delta^2\text{H}$  values in the sampled ice. Assuming Pleistocene rates of sediment transport were similar to today's, the sediment transport lag time is between  $10^4$  and  $10^5$  years.

Despite the several sources of uncertainty in model variables, broad conclusions can still be robustly drawn. At the northern two sites, the meteoric  $^{10}\text{Be}$  inventories are large enough that erosion rates are less than 4 m/My under all simulation conditions (Figure 4). Under such low erosion, much of the meteoric  $^{10}\text{Be}$  inventory is inherited from pre-Quaternary sediment and the results are sensitive to assumed pre-glacial erosion rates. At Kangerlussuaq, glacial erosion rates of 10-20 m/My are possible only under

greater than 150 ka of decay-correct interglacial exposure and some affect of sediment transport lag time (Figure 4). This exposure time is substantially longer than ~30 ka the global ice volume record indicates (Bitanja and van de Wal, 2008), suggesting that glacial retreat along this flowline leads global ice sheet response to climate warming by several thousand years. Preservation of pre-Quaternary meteoric  $^{10}\text{Be}$  inventory is unlikely, as erosion rates less than 3 m/My would be required.

These results suggest substantial differences between the northern and southern domes of the Greenland Ice Sheet. The northern Greenland Ice Sheet appears to lack the long-term erosive capability of Southern Dome, retaining pre-Quaternary meteoric  $^{10}\text{Be}$  regardless of the length of interglacial periods prescribed. With at least moderately high erosion rates for the southern Greenland Ice Sheet confirmed by sediment flux and sediment volume studies (Andrews et al., 1994; Knight et al., 2002), the meteoric  $^{10}\text{Be}$  concentrations are explained through prolonged interglacial exposure. This suggests that at least the southern Greenland Ice Sheet is highly responsive to temperature increase and partially confirms models of its past retreats (Otto-Bliesner et al., 2006).

Chapter 5 Figures

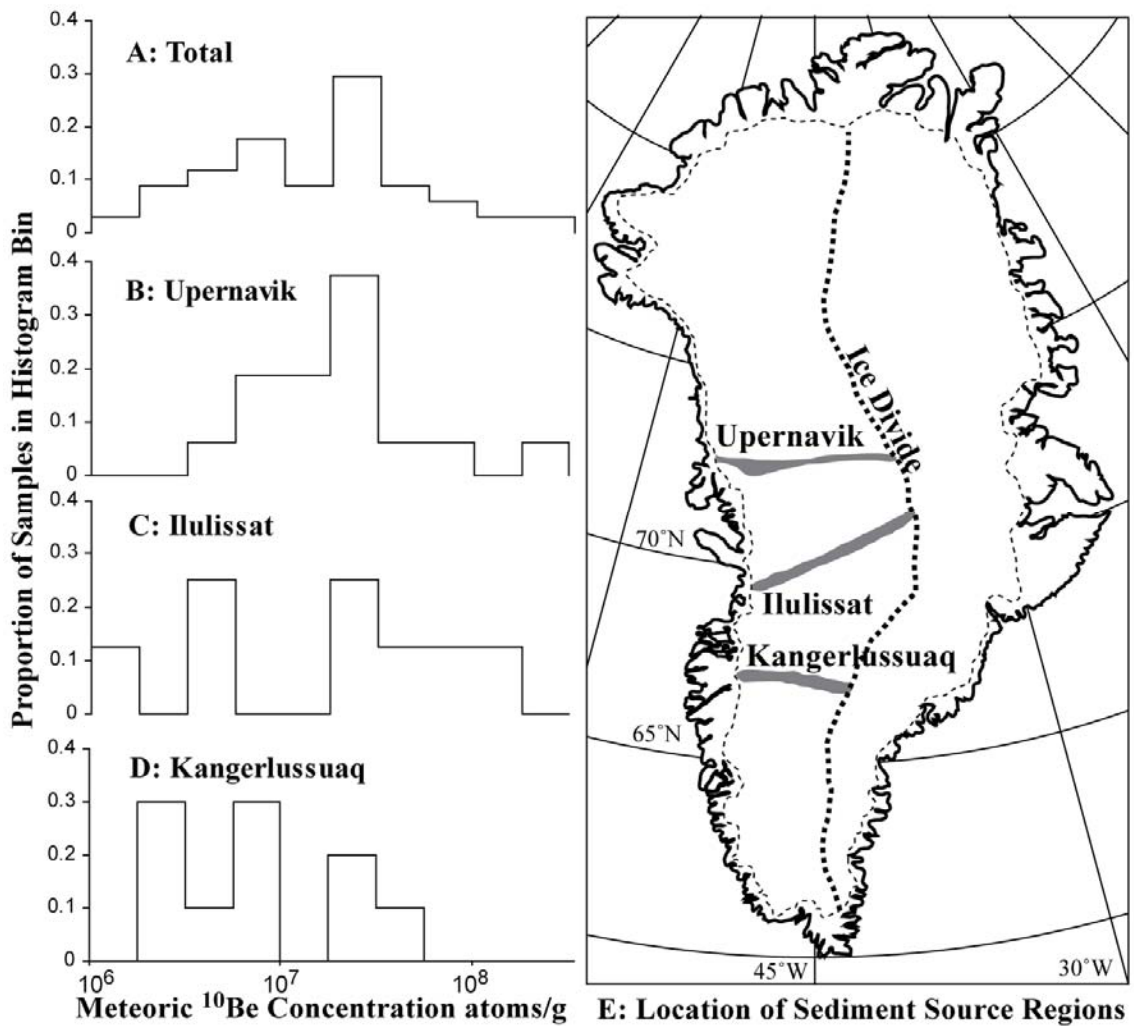


Figure 1: Total (A) and site specific (B-D) distribution of meteoric  $^{10}\text{Be}$  concentrations in ice-entrained sediment at the three West Greenland sites. Source regions of sediment delivered to the modern margin of the Greenland Ice Sheet based on flowlines modeled from geophysical data (Wang et al., 2002) are also shown (E).

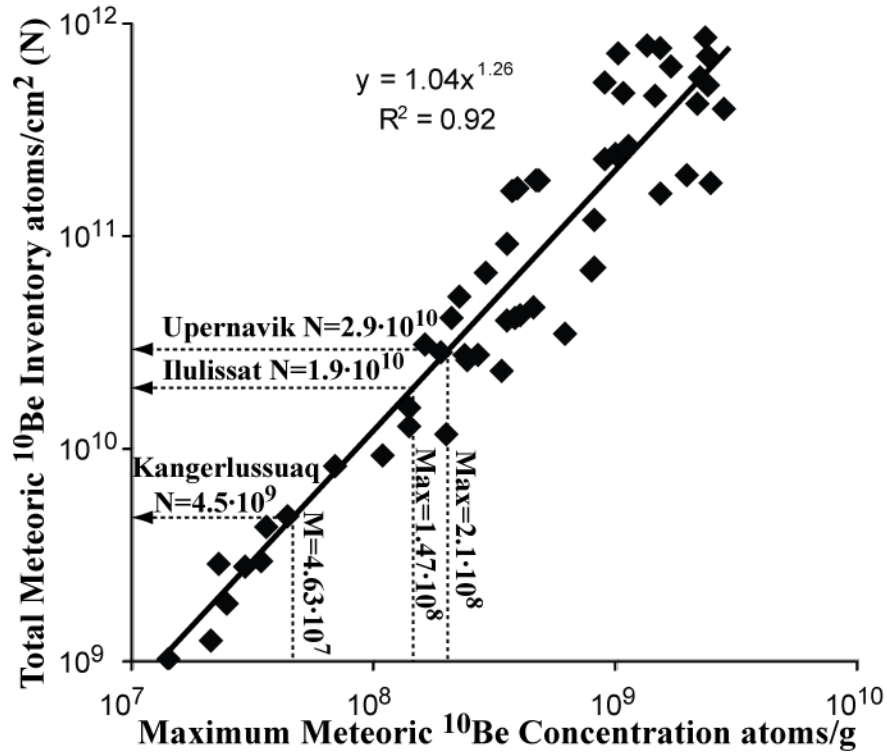


Figure 2: Derivation of meteoric  $^{10}\text{Be}$  inventories in source soils from the maximum measured meteoric  $^{10}\text{Be}$  concentration at each site. The relationship between maximum meteoric  $^{10}\text{Be}$  concentration and total meteoric  $^{10}\text{Be}$  inventory in mid latitude soils is used as a calibration curve (Graly et al., Submitted).

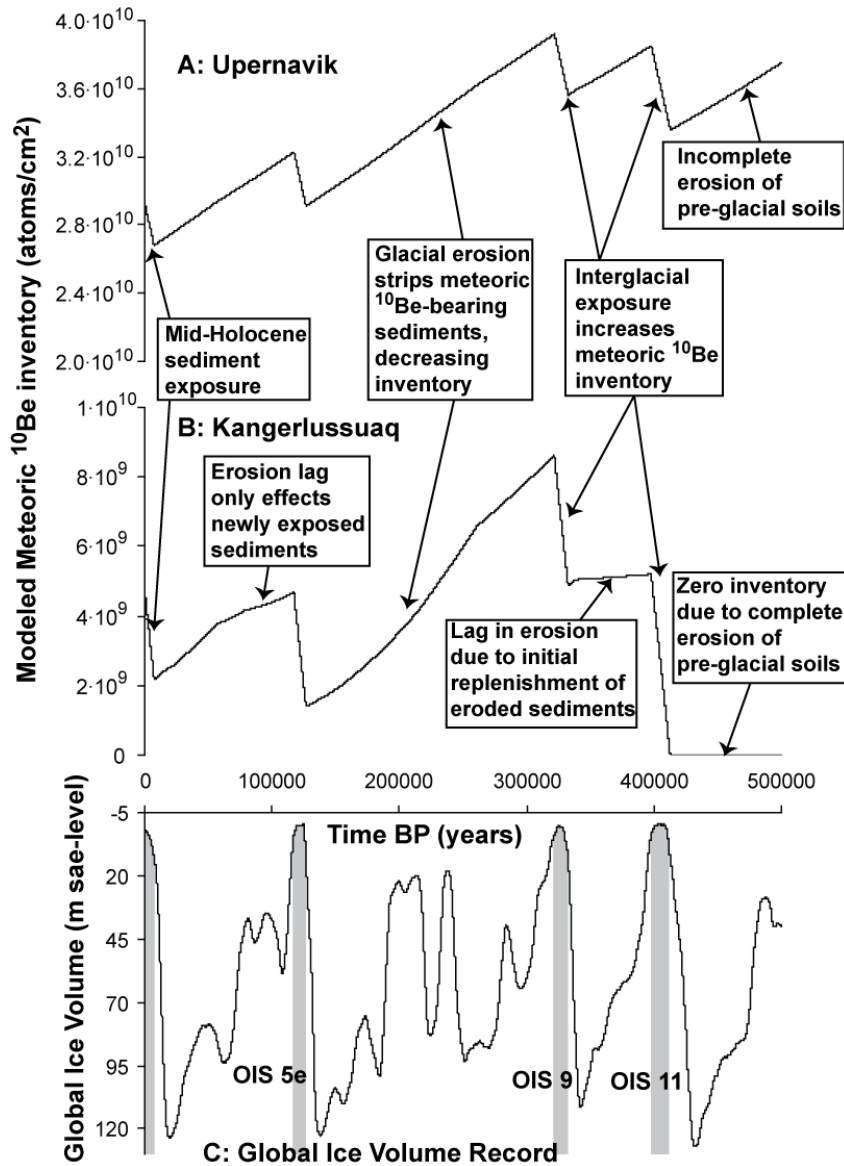


Figure 3: Modeled effect of 500 ka of interglacial period surface exposure and glacial period erosion on the meteoric  $^{10}\text{Be}$  inventory in sub ice soils. The low erosion northern site (A: Upernavik) is compared to the high erosion southern site (B: Kangerlussuaq). The construction of interglacial period length from the global ice volume record (Bitanja and van de Wal, 2008) is also shown (C).

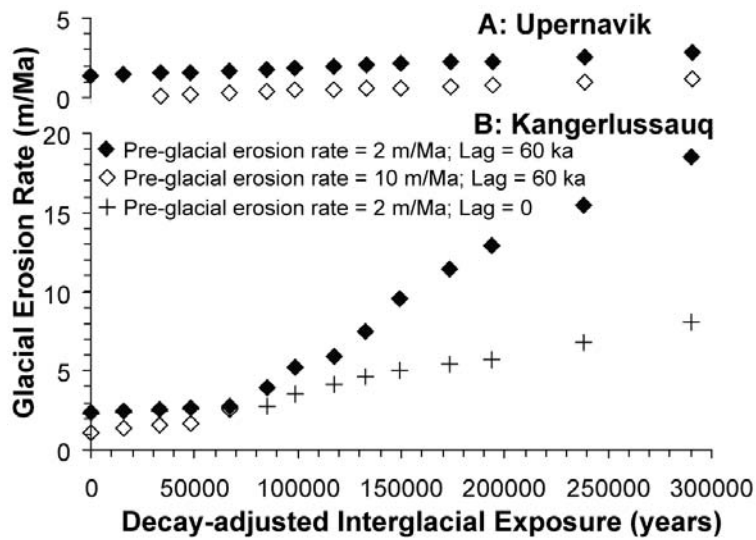


Figure 4: Modeled relationship between glacial period erosion rate and cumulative interglacial exposure of sub-ice soils for Upernavik (A) and Kangerlussauq (B), showing sensitivity to pre-glacial meteoric  $^{10}\text{Be}$  inventory and the lag in erosion from the sub-glacial transport of sediment.

## **Chapter 6: Supplement from Meteoric $^{10}\text{Be}$ evidence for past interglacial ice sheet retreat in western Greenland**

(submitted as an online supplement accompanying the submission to *Nature*)

### **Supplement A: Accelerator Mass Spectrometry Measurements**

After their removal from the ice sheet, sediment-rich ice samples were stored in sealed containers where they were allowed to melt. The meltwater was decanted and the sediment dried and pulverized.  $^{10}\text{Be}$  was extracted from the sediment using a modification of the  $\text{KHF}_2$  flux method (Stone, 1998). In the meltwater,  $\delta^{18}\text{O}$  was measured through equilibration with  $\text{CO}_2$  gas (Socki et al., 1992), and  $\delta^2\text{H}$  was measured through  $\text{H}_2$  extraction by elemental zinc (Coleman et al., 1982)

$^{10}\text{Be}$  content was measured by using an accelerator mass spectrometer to determine a  $^{10}\text{Be}/^9\text{Be}$  ratio, where the  $^9\text{Be}$  values were controlled by adding about 300  $\mu\text{g}$  of Be carrier. A full process blank was measured with each batch of 16 samples to quantify the  $^{10}\text{Be}$  introduced in the preparation and measurement process. The measurements were performed at Lawrence Livermore National Laboratory and referenced to the 07KNSTD standard (Nishiizumi et al., 2007). The raw data from these measurements are presented in Table A1.

## Supplement B: Stable Isotope Results

The ice samples were determined to be of Pleistocene age based on the comparison of the  $\delta^{18}\text{O}$  and  $\delta^2\text{H}$  values in the samples to measurements of these stable isotopes in Central Greenland ice core records. The ice sheet flowlines at Kangerlussauq (67.1° N) trace slightly north of the site of the Dye-3 ice core, while the Ilulissat (69.4° N) and Upernavik (72.6°) flowlines trace approximately to the location of the Summit ice cores (Figure 1e – text). In both Summit and Dye-3 cores, Pleistocene cold phases, Pleistocene mild phases, and the Holocene can be differentiated by their distinctive  $\delta^{18}\text{O}$  (Dansgaard et al., 1982; Stuiver and Grootes, 2000) and  $\delta^2\text{H}$  signatures (Johnsen et al., 1989; Jouzel et al., 2007).

When glacial basal ice melts and refreezes along the glacial bed through the process of regelation, if a portion of the meltwater escapes into subglacial drainage systems, the basal ice becomes progressively enriched in heavy isotopes. (Iverson and Souchez, 1996; Sugden et al., 1987). Marginal basal ice samples are therefore not necessarily directly comparable to isotopic phases found unregelated ice. Because this enrichment effect is more strongly expressed by  $\delta^2\text{H}$  values than  $\delta^{18}\text{O}$  values, the relationship between the two isotope systems can be used to estimate the pre-regelation isotopic composition of the ice. Under experimental conditions, ice subjected to open-system regelation develops a  $\delta^{18}\text{O} / \delta^2\text{H}$  enrichment trend with a slope of  $\sim 6.08$ , 1.92 less than the slope of 8 found in the meteoric water line (Iverson and Souchez, 1996).

At each of the three sites, samples were collected from a number of sub-sites, where different glaciological conditions could be expected (Table B1). Only at sub-site

U1 were enough samples collected to construct a statistically significant enrichment trend. This site is characterized by a gently sloping terminal ice face that allowed samples to be collected in a vertical transect across the basal ice layer. The  $\delta^{18}\text{O} / \delta^2\text{H}$  enrichment trend at this site has a slope of  $6.07 \pm 0.57$  (Figure B1), nearly identical to the regelation slope found under experimental conditions (Iverson and Souchez, 1996).

Based on the  $\delta^{18}\text{O} / \delta^2\text{H}$  enrichment slope of 8 found in precipitation (Craig, 1961), deuterium excess is defined as  $\delta^2\text{H} - 8 \cdot \delta^{18}\text{O}$ . Treating sub-site U1 and Iverson and Souchez's (1996) results as representative, we apply a correction of 1‰  $\delta^{18}\text{O}$  for every 1.92‰ deuterium excess is depleted below central Greenland ice cores values. Due to the variability in the central Greenland ice core deuterium excess values (Table B2), this correction is approximate. The Pleistocene mild phases exhibit about 4‰ less deuterium excess than the Holocene and Pleistocene cold phases (Johnsen et al., 1989), necessitating a separate correction. Measurements of  $\delta^{18}\text{O}$  and  $\delta^2\text{H}$  and the corrections for regelation effects are summarized in Table B3.

The heterogeneity of ice ages at several of the sites is consistent with layer deformation and mixing often found in basal and marginal ice (e.g. Patrenko et al., 2006; Suwa et al., 2006). The ice is predominately Pleistocene in age, though at some sites, Holocene ice is intermixed. Though site U1 does not display this sort of heterogeneity, its interpretation is unclear. The regelation corrected  $\delta^{18}\text{O}$  values are about 1‰ depleted from Summit Holocene values, but well enriched from Summit Pleistocene cold or mild phase values. Given the site's proximity to a regional flow divide (Zwally and Giovinetto, 2001), it is possible that the ice here is sourced more locally. If this is case,

the values are very likely Pleistocene, as  $\delta^{18}\text{O}$  is enriched in coastal regions. It is also possible that the ice does originate near Summit and the isotope values reflect conditions of a non-typical period such as the Eemian interglacial (116-130 ka before present) or the Holocene/Pleistocene transition.

### **Supplement C: Sediment Transport Model**

The estimates of the rate of transport of basal sediment material are based on the two dimensional geophysical reconstructions of the modern Greenland Ice Sheet's flowlines by WL Wang (i.e. Wang et al., 2002). The flowline is divided into 1km horizontal grid components and 100 vertical components scaled to the height of the ice sheet. Because the effect of vertical velocity in the bottom layer of this model is largely inconsequential, only the horizontal velocity component is used to calculate rates of basal sediment transport.

The resulting transport rates are variable, but are generally higher closer to the ice sheet margin and lower in the interior (Figure C1). A total time required to transport sediment from a position in the interior to the margin can be calculated by summing the inverse of these horizontal transport rates (Figure C2). This shows that within ~100 km of the modern ice margin, sediment was likely evacuated within the ~10,000 years of Holocene climate conditions. Interior of this, total sediment transport time increases exponentially to ~100,000 years near the continental flow divide, raising the possibility that some sediment was in transit for most of the last glacial period.

## Supplement D: Erosion/Exposure Model

A model is used to determine a series of possible solutions that explain the meteoric  $^{10}\text{Be}$  data through a combination of interglacial period exposure and glacial period erosion. The reconstruction of global ice volume by Bitanja and van de Wal (2008) is used to construct a series of glacial and interglacial periods by specifying the sea-level equivalent at which the interglacial periods commence on a falling ice volume trend and cease on a rising ice volume trend. In most of the simulations, the initiation of interglacial periods is assumed to correspond to a higher ice volume than the termination. This is consistent with the Greenland Ice Sheet's inferred behavior during the Holocene, where retreat surpassed the present margin at  $\sim 7$  ka before present (while global ice volume was  $\sim 10\text{m}$  sea level equivalent above modern) and advanced to present margins during the Little Ice Age (with no discernable effect on global ice volume) (Young et al., 2010). The model numerically calculates an erosion rate that generates the observed meteoric  $^{10}\text{Be}$  inventory over this prescribed series of glacial cycles.

To simplify the calculations, the entire sediment source region for each of the three sites is treated as a single, one dimensional soil profile whose meteoric  $^{10}\text{Be}$  depth distribution changes with time. This distribution is based on the relationship between total meteoric  $^{10}\text{Be}$  inventory and average meteoric  $^{10}\text{Be}$  concentration to depths 30 cm, 70 cm, and 150 cm in the same mid-latitude soil dataset that was used to estimate total meteoric  $^{10}\text{Be}$  inventory originally (Graly et al., Submitted) (Figure D1). To correctly simulate that new meteoric  $^{10}\text{Be}$  is deposited at the top of the soil profile, the contribution

of each interglacial period to the total contemporary meteoric  $^{10}\text{Be}$  inventory is treated separately. The inventory generated during a interglacial period (N) is calculated:

$$N=(q/\lambda)(1-e^{-\lambda t}) \quad (1)$$

Where N is measured in atoms/cm<sup>2</sup>, t is the length of the interglacial period (years),  $\lambda$  is the  $^{10}\text{Be}$  disintegration constant  $5.0 \cdot 10^{-7}$  (yr<sup>-1</sup>) (KORSHINEK et al., 2010), and q is the average annual flux of meteoric  $^{10}\text{Be}$  atoms into the soil profile of  $3.5 \cdot 10^5$  (atoms·cm<sup>-2</sup>·yr<sup>-1</sup>). The subsequent loss of meteoric  $^{10}\text{Be}$  to glacial erosion ( $N_L$ ) is calculated:

$$N_L = z \cdot q \cdot \alpha \cdot (N/q)^\beta \quad (2)$$

Where z is the depth of erosion (cm) calculated from the glacial erosion rate multiplied by the cumulative length of glacial periods, and  $\alpha$  and  $\beta$  are the empirical power-law components of the inventory depth relationship (Figure D1). For  $z < 30\text{cm}$ , the components for the Figure D1A are applied. For z between 30 and 150 cm, a weighted average of the results of the two nearest correlations is applied. Below 150 cm, interpretation is more ambiguous as only a few deep regolith cores have been studied. In these, meteoric  $^{10}\text{Be}$  can be detected at over 10 meters of depth (Brown et al., 1988). To simulate this distribution, we continue to use the power law components from the 150 cm relationship (Figure D1C), but adjust the applied depth (z) by a exponent factor of 0.85. This creates a depth distribution that moderately matches data from published regolith cores (Figure D2).

Prior to the first significant ice volume minimum 2.72 Ma before present, meteoric  $^{10}\text{Be}$  inventory is assumed to be in steady state between deposition and loss to decay and fluvially-dominated erosion. This pre-glacial meteoric  $^{10}\text{Be}$  inventory (N) is

calculated numerically based on an assumed pre-glacial meteoric  $^{10}\text{Be}$  deposition rate ( $q$ ) and erosion rate ( $E$ ):

$$N=q(1-E\cdot\alpha\cdot(N/q)^\beta)/(\lambda(1-e^{-\lambda t})) \quad (3)$$

Where  $E$  is measured in cm/yr. and  $\alpha$  and  $\beta$  values from the 30 cm trend are used (Figure D1A).

Because interglacial periods are not sufficiently long for large fluvial drainage systems to develop, interglacial period erosion is assumed to be zero. However, interglacial soil development processes may vertically transport meteoric  $^{10}\text{Be}$  within the soil column. A small correction for this effect is applied by reducing the depth adjustment exponent for erosion below 150 cm by 0.01 for every 200,000 years of interglacial exposure.

Basal sediment transport is modelled simply by subtracting a transport time from the cumulative glacial period erosion length applied to each interglacial exposure. Per supplement C, the appropriate value is not necessarily clear. Mean transport times vary from 20,000 – 40,000 years (Figure C2). But if sediment is primarily entrained near the ice sheet margin (e.g. Alley et al., 1997), the average transport value could be much shorter. But if entrained sediment can exit and re-enter the basal ice layer as glaciological conditions change (e.g. Rempel, 2008), the average transport time might be longer. The values of 60,000 and 0 used in the Figure 4 of the text may set reasonable boundaries on this uncertainty.

The model parameters and results used for Figure 4 in the text are summarized in Table D1.

## Chapter 6 Tables

Table A1: Accelerator Mass Spectrometry Data

Sample	Site	Sample Mass (g)	Be Carrier Mass (g)	Measured $^{10}\text{Be} / ^9\text{Be}$ Ratio	Blank Corrected Ratio	Error (%)	$^{10}\text{Be}$ (atoms/g)
GK001W	Kangerlussuaq	0.215	0.299	$2.34 \cdot 10^{-13}$	$2.19 \cdot 10^{-13}$	2.26	$2.04 \cdot 10^7$
GK011W	Kangerlussuaq	0.170	0.301	$8.00 \cdot 10^{-14}$	$6.49 \cdot 10^{-14}$	3.37	$7.69 \cdot 10^6$
GK025W	Kangerlussuaq	0.497	0.299	$2.21 \cdot 10^{-13}$	$2.06 \cdot 10^{-13}$	2.66	$8.29 \cdot 10^6$
GK028W	Kangerlussuaq	0.525	0.302	$7.16 \cdot 10^{-14}$	$5.65 \cdot 10^{-14}$	5.58	$2.17 \cdot 10^6$
GK037WA	Kangerlussuaq	0.496	0.300	$1.16 \cdot 10^{-13}$	$1.01 \cdot 10^{-13}$	3.25	$4.07 \cdot 10^6$
GK037WB	Kangerlussuaq	0.552	0.301	$1.16 \cdot 10^{-13}$	$1.01 \cdot 10^{-13}$	5.14	$3.67 \cdot 10^6$
GK076W	Kangerlussuaq	0.546	0.302	$1.04 \cdot 10^{-13}$	$8.85 \cdot 10^{-14}$	4.19	$3.28 \cdot 10^6$
GK081W	Kangerlussuaq	0.245	0.301	$3.82 \cdot 10^{-13}$	$3.67 \cdot 10^{-13}$	2.48	$3.02 \cdot 10^7$
GK091W	Kangerlussuaq	0.215	0.302	$8.75 \cdot 10^{-14}$	$7.24 \cdot 10^{-14}$	4.53	$6.81 \cdot 10^6$
GK093W	Kangerlussuaq	0.100	0.301	$2.45 \cdot 10^{-13}$	$2.30 \cdot 10^{-13}$	3.25	$4.63 \cdot 10^7$
GL005W	Ilulissat	0.463	0.301	$1.48 \cdot 10^{-12}$	$1.47 \cdot 10^{-12}$	2.38	$6.38 \cdot 10^7$
GL011W	Ilulissat	0.516	0.300	$6.02 \cdot 10^{-14}$	$4.51 \cdot 10^{-14}$	6.74	$1.75 \cdot 10^6$
GL015W	Ilulissat	0.128	0.301	$9.49 \cdot 10^{-13}$	$9.34 \cdot 10^{-13}$	1.53	$1.47 \cdot 10^8$
GL019W	Ilulissat	0.249	0.301	$5.32 \cdot 10^{-13}$	$5.17 \cdot 10^{-13}$	1.76	$4.18 \cdot 10^7$
GL020W	Ilulissat	0.377	0.298	$3.96 \cdot 10^{-13}$	$3.81 \cdot 10^{-13}$	2.47	$2.02 \cdot 10^7$
GL028W	Ilulissat	0.495	0.303	$1.14 \cdot 10^{-13}$	$9.90 \cdot 10^{-14}$	3.36	$4.05 \cdot 10^6$
GL031W	Ilulissat	0.623	0.302	$7.34 \cdot 10^{-13}$	$7.19 \cdot 10^{-13}$	5.24	$2.33 \cdot 10^7$
GL052W	Ilulissat	0.502	0.301	$1.20 \cdot 10^{-13}$	$1.04 \cdot 10^{-13}$	4.70	$4.19 \cdot 10^6$
GU018W	Upernavik	0.498	0.301	$1.98 \cdot 10^{-13}$	$1.83 \cdot 10^{-13}$	3.00	$7.42 \cdot 10^6$
GU019W	Upernavik	0.206	0.301	$9.13 \cdot 10^{-14}$	$7.62 \cdot 10^{-14}$	3.18	$7.45 \cdot 10^6$
GU021W	Upernavik	0.506	0.295	$2.98 \cdot 10^{-13}$	$2.83 \cdot 10^{-13}$	3.85	$1.11 \cdot 10^7$
GU022W	Upernavik	0.490	0.302	$1.95 \cdot 10^{-13}$	$1.80 \cdot 10^{-13}$	2.20	$7.43 \cdot 10^6$
GU023W	Upernavik	0.500	0.300	$1.24 \cdot 10^{-13}$	$1.09 \cdot 10^{-13}$	4.49	$4.39 \cdot 10^6$
GU025W	Upernavik	0.324	0.299	$2.21 \cdot 10^{-13}$	$2.06 \cdot 10^{-13}$	2.56	$1.27 \cdot 10^7$
GU028W	Upernavik	0.500	0.300	$7.82 \cdot 10^{-13}$	$7.66 \cdot 10^{-13}$	3.76	$3.08 \cdot 10^7$
GU029W	Upernavik	0.442	0.299	$5.30 \cdot 10^{-13}$	$5.15 \cdot 10^{-13}$	2.40	$2.33 \cdot 10^7$
GU030W	Upernavik	0.492	0.301	$3.12 \cdot 10^{-13}$	$2.97 \cdot 10^{-13}$	2.02	$1.22 \cdot 10^7$
GU032W	Upernavik	0.301	0.300	$3.61 \cdot 10^{-13}$	$3.46 \cdot 10^{-13}$	2.44	$2.31 \cdot 10^7$
GU034W	Upernavik	0.437	0.302	$4.52 \cdot 10^{-12}$	$4.50 \cdot 10^{-12}$	2.40	$2.08 \cdot 10^8$
GU050W	Upernavik	0.084	0.298	$1.39 \cdot 10^{-13}$	$1.24 \cdot 10^{-13}$	2.79	$2.93 \cdot 10^7$
GU054W	Upernavik	0.348	0.301	$1.29 \cdot 10^{-12}$	$1.27 \cdot 10^{-12}$	2.44	$7.37 \cdot 10^7$
GU059W	Upernavik	0.587	0.297	$5.96 \cdot 10^{-13}$	$5.81 \cdot 10^{-13}$	2.49	$1.97 \cdot 10^7$
GU065W	Upernavik	0.279	0.297	$7.23 \cdot 10^{-13}$	$7.08 \cdot 10^{-13}$	2.37	$5.04 \cdot 10^7$
GU077W	Upernavik	0.338	0.304	$3.59 \cdot 10^{-13}$	$3.44 \cdot 10^{-13}$	2.81	$2.07 \cdot 10^7$

Table B1: Site descriptions

Subsite*	Latitude	Longitude	# of samples	Description
K1	67.156	-50.027	4	Dead ice zone between the Russell and Isunnguata Sermia Glaciers
K2	67.157	-50.064	5	South lateral margin of Isunnguata Sermia Glacier
K3	67.136	-50.062	2	North lateral margin of Russell Glacier
K4	67.140	-50.046	1	Terminal margin between Russell and Isunnguata Sermia Glaciers
L1	69.431	-50.263	5	West lateral margin of the Sermeq Avannarleq Glacier
L2	69.426	-50.360	3	Small terminal offbranch of Sermeq Avannarleq Glacier
U1	72.534	-53.678	15	Terminal Ice Sheet margin
U2	72.619	-53.576	3	Terminal margin on east side of nunatak
U3	72.713	-54.177	3	Terminal Ice Sheet margin

\*K is for Kangerlussuaq, L for Ilulissat, and U for Upernavik

Table B2: Central Greenland stable isotope value ranges

Ice Core Site	Phase	$\delta^{18}\text{O}$ ‰	Deuterium Excess ‰
Dye 3 <sup>[1]</sup>	Pleistocene Cold	-34 to -36.5	7 to 9
	Pleistocene Mild	-31 to -33	3 to 5
	Holocene	-27 to -29	7 to 9
Summit <sup>[2]</sup>	Pleistocene Cold	-40 to -44	8 to 10
	Pleistocene Mild	-36 to -39	4 to 6
	Holocene	-34 to -35.5	~9

[1]:  $\delta^{18}\text{O}$  data from (Dansgaard et al., 1982);  $\delta^2\text{H}$  data from (Johnsen et al., 1996)

[2]:  $\delta^{18}\text{O}$  data from (Stuiver and Groot, 2000);  $\delta^2\text{H}$  data from (Jouzel et al., 2007)

Table B3: Stable Isotope Data

Sample	Location	$\delta^{18}\text{O}$ ‰	$\delta^2\text{H}$ ‰	Deuterium Excess ‰	Meteoric $^{10}\text{Be}$ (atoms/g)	Corrected $\delta^{18}\text{O}$ ‰		Phase determination
						Pleistocene Mild Phase Correction	Cold Phase / Holocene Correction	
GK001W	K1	-33.51	-265.73	2.37	$2.04 \cdot 10^7$	-34.36	-36.44	Pleistocene Cold
GK011W	K1	-32.13	-253.54	3.47	$7.69 \cdot 10^6$	-32.13	-34.49	Either Pleistocene
GK076W	K1	-33.40	-263.11	4.11	$3.28 \cdot 10^6$	-33.40	-35.43	Either Pleistocene
GK081W	K1	-30.95	-242.77	4.84	$3.02 \cdot 10^7$	-30.95	-32.60	Pleistocene Mild
GK025W	K2	-33.23	-261.86	3.98	$8.29 \cdot 10^6$	-33.23	-35.33	Either Pleistocene
GK028W	K2	-33.20	-266.46	-0.83	$2.17 \cdot 10^6$	-35.72	-37.80	Pleistocene Cold
GK032W	K2	-32.61	-262.14	-1.26	-	-35.35	-37.43	Pleistocene Cold
GK037WA	K2	-25.43	-199.03	4.42	$4.07 \cdot 10^6$	-25.43	-27.29	Holocene
GK037WB	K2	-32.46	-262.53	-2.85	$3.67 \cdot 10^6$	-36.03	-38.11	Pleistocene Cold
GK087W	K3	-30.03	-239.54	0.69	-	-31.75	-33.84	Pleistocene Mild
GK091W	K3	-24.25	-195.11	-1.11	$6.81 \cdot 10^6$	-26.91	-28.99	Holocene
GK093W	K4	-32.30	-258.78	-0.39	$4.63 \cdot 10^7$	-34.58	-36.67	Pleistocene Cold
GL005W	L1	-36.86	-291.86	3.02	$6.38 \cdot 10^7$	-37.85	-39.98	Pleistocene Mild
GL011W	L1	-37.24	-293.37	4.58	$1.75 \cdot 10^6$	-37.45	-39.55	Pleistocene Mild
GL015W	L1	-35.72	-283.35	2.43	$1.47 \cdot 10^8$	-37.01	-39.15	Pleistocene Mild
GL019W	L1	-37.20	-289.92	7.67	$4.18 \cdot 10^7$	-37.20	-37.89	Pleistocene Mild
GL020W	L1	-36.64	-290.91	2.23	$2.02 \cdot 10^7$	-38.03	-40.17	Pleistocene Mild
GL028W	L2	-34.37	-274.65	0.31	$4.05 \cdot 10^6$	-36.72	-38.90	Pleistocene Mild
GL031W	L2	-33.84	-266.22	4.51	$2.33 \cdot 10^7$	-34.08	-36.18	Holocene?
GL052W	L2	-33.89	-269.22	1.92	$4.19 \cdot 10^6$	-35.43	-37.58	Pleistocene Mild
GU018W <sup>[1]</sup>	U1	-32.88	-259.53	3.54	$7.42 \cdot 10^6$	-33.61	-35.73	Unclear
GU019W	U1	-31.50	-251.14	0.83	$7.45 \cdot 10^6$	-33.58	-35.75	Unclear
GU020W	U1	-32.64	-261.22	-0.09	-	-35.19	-37.37	Unclear
GU021W	U1	-34.72	-270.90	6.86	$1.11 \cdot 10^7$	-33.79	-35.84	Unclear
GU022W	U1	-32.86	-260.78	2.08	$7.43 \cdot 10^6$	-34.32	-36.46	Unclear
GU023W	U1	-35.45	-276.69	6.91	$4.39 \cdot 10^6$	-34.49	-36.54	Unclear
GU024W	U1	-33.53	-265.29	2.95	-	-34.56	-36.68	Unclear
GU025W	U1	-33.57	-266.51	2.01	$1.27 \cdot 10^7$	-35.06	-37.21	Unclear
GU027W	U1	-34.16	-264.31	8.97	-	-34.16	-34.18	Unclear
GU028W	U1	-33.84	-264.52	6.20	$3.08 \cdot 10^7$	-33.24	-35.30	Unclear
GU029W	U1	-35.91	-273.77	13.54	$2.33 \cdot 10^7$	-	-35.91	Unclear
GU030W	U1	-35.91	-282.14	5.16	$1.22 \cdot 10^7$	-35.83	-37.91	Unclear
GU032W	U1	-34.35	-269.44	5.36	$2.31 \cdot 10^7$	-	-36.24	Unclear
GU034W <sup>[2]</sup>	U1	-35.75	-277.14	8.88	$2.08 \cdot 10^8$	-35.75	-35.81	Unclear
GU035W <sup>[3]</sup>	U1	-33.13	-255.05	10.02	-	-33.13	-33.13	Unclear
GU046W	U2	-38.91	-312.87	-1.59	-	-42.21	-44.21	Pleistocene Cold
GU050W	U2	-30.84	-246.01	0.71	$2.93 \cdot 10^7$	-32.99	-34.99	Holocene
GU054W	U2	-37.98	-294.90	8.91	$7.37 \cdot 10^7$	-37.98	-38.02	Pleistocene Mild
GU059W	U3	-31.22	-246.60	3.20	$1.97 \cdot 10^7$	-32.12	-34.12	Holocene
GU065W	U3	-37.53	-300.54	-0.32	$5.04 \cdot 10^7$	-40.19	-42.19	Pleistocene Cold
GU077W	U3	-37.79	-300.27	2.08	$2.07 \cdot 10^7$	-39.25	-41.25	Pleistocene Cold

[1]: Bottom of basal ice layer

[2]: Top of basal ice layer

[3]: Sample from clean ice above basal ice layer

Table D1: Erosion/Exposure model results

Interglacial Initiation Ice Volume (m sea-level) <sup>[1]</sup>	Interglacial Termination Ice Volume (m sea-level) <sup>[1]</sup>	Decay- Adjusted Interglacial Duration (10 <sup>3</sup> Years)	Erosion Rate (m/My)								
			Pre-glacial Inventory = 3.70·10 <sup>11</sup> Erosion lag = 60,000 years		Pre-glacial Inventory = 8.38·10 <sup>10</sup> Erosion lag = 60,000 years		Pre-glacial Inventory = 3.70·10 <sup>11</sup> Erosion lag = 0 years				
			Kangerlussaq	Ilulissat	Upernavik	Kangerlussaq	Ilulissat	Upernavik	Kangerlussaq	Ilulissat	Upernavik
-1	-1	0	2.32	1.74	1.34	1.09	0.12	[2]	2.27	1.70	1.31
0	0	15.5	2.43	1.84	1.45	1.38	0.25	[2]	2.36	1.79	1.40
0.6	0.6	33.5	2.52	1.93	1.53	1.55	0.37	0.10	2.44	1.86	1.47
1.6	1.6	48.1	2.62	2.01	1.60	1.70	0.46	0.19	2.52	1.93	1.54
4	2	67.0	2.76	2.13	1.71	2.57	0.61	0.27	2.66	2.05	1.64
6	3	85.2	3.98	2.25	1.81	3.98	0.74	0.36	2.80	2.16	1.74
8	4	98.6	5.25	2.34	1.89	5.25	0.85	0.45	3.54	2.23	1.80
10	4	117.3	5.88	2.42	1.96	5.88	0.92	0.52	4.09	2.31	1.87
12.5	4	133.0	7.51	2.51	2.03	7.51	1.00	0.58	4.65	2.40	1.94
15	4	149.5	9.55	2.61	2.11	9.55	1.07	0.64	5.05	2.49	2.01
17.5	4	173.6	11.43	2.73	2.21	11.43	1.16	0.72	5.40	2.60	2.10
20	4	193.6	12.95	2.83	2.30	12.95	1.25	0.79	5.75	2.69	2.18
25	4	238.2	15.43	3.09	2.53	15.43	1.51	0.96	6.80	2.90	2.37
30	4	290.0	18.53	3.41	2.80	18.53	1.77	1.13	8.11	3.18	2.60
40	4	375.1	43.84	4.13	3.41	43.84	2.56	1.61	12.76	3.76	3.10

[1]: Modern ice volume is 1.6 m

[2] Due to the decay of the isotope over 2.72 Ma, interglacial exposure this low is not possible with this pre-glacial inventory.

Chapter 6 Figures

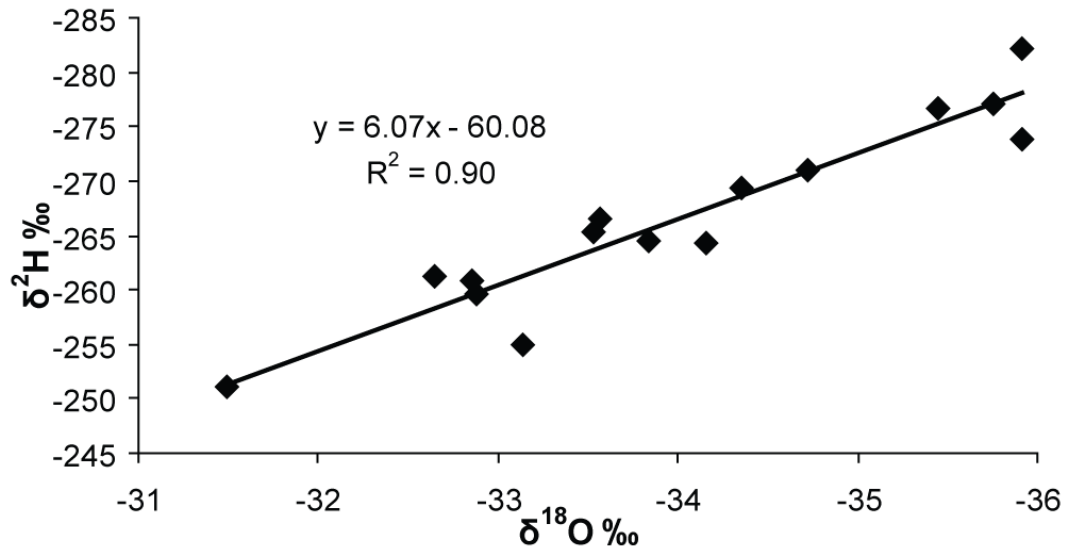


Figure B1: Regeneration enrichment trend in stable isotope data from subsite U1.

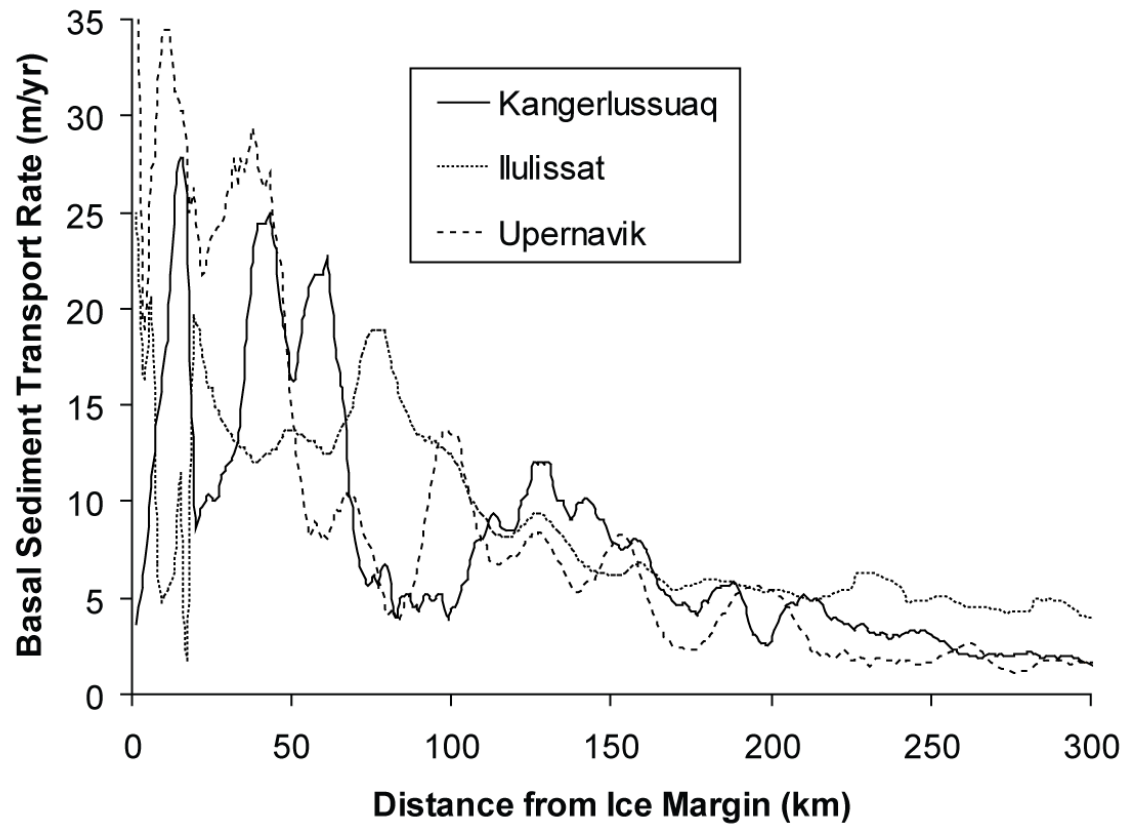


Figure C1: Rate of basal sediment transport as a function of distance from the Greenland Ice Sheet margin along the flowlines of the three West Greenland sites.

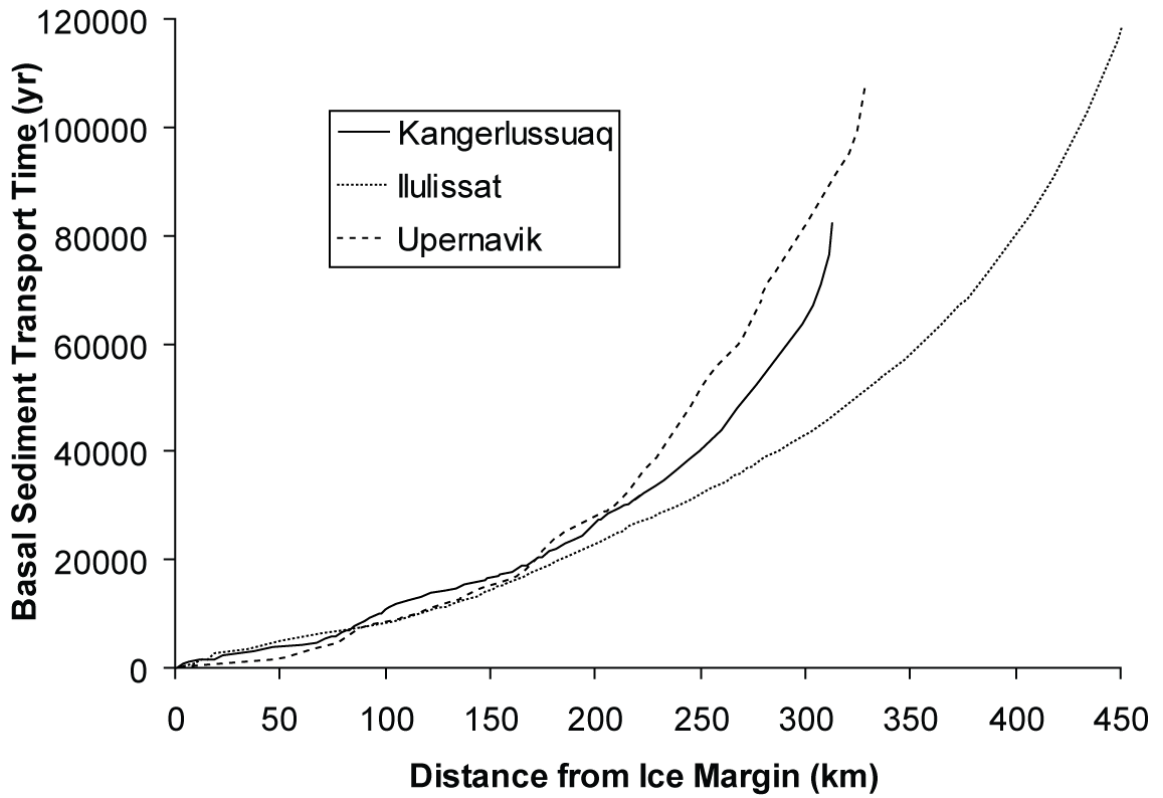


Figure C2: Total time necessary to transport basal sediment to the Greenland Ice Sheet margin from X distance in the interior along the flowlines of the three West Greenland sites.

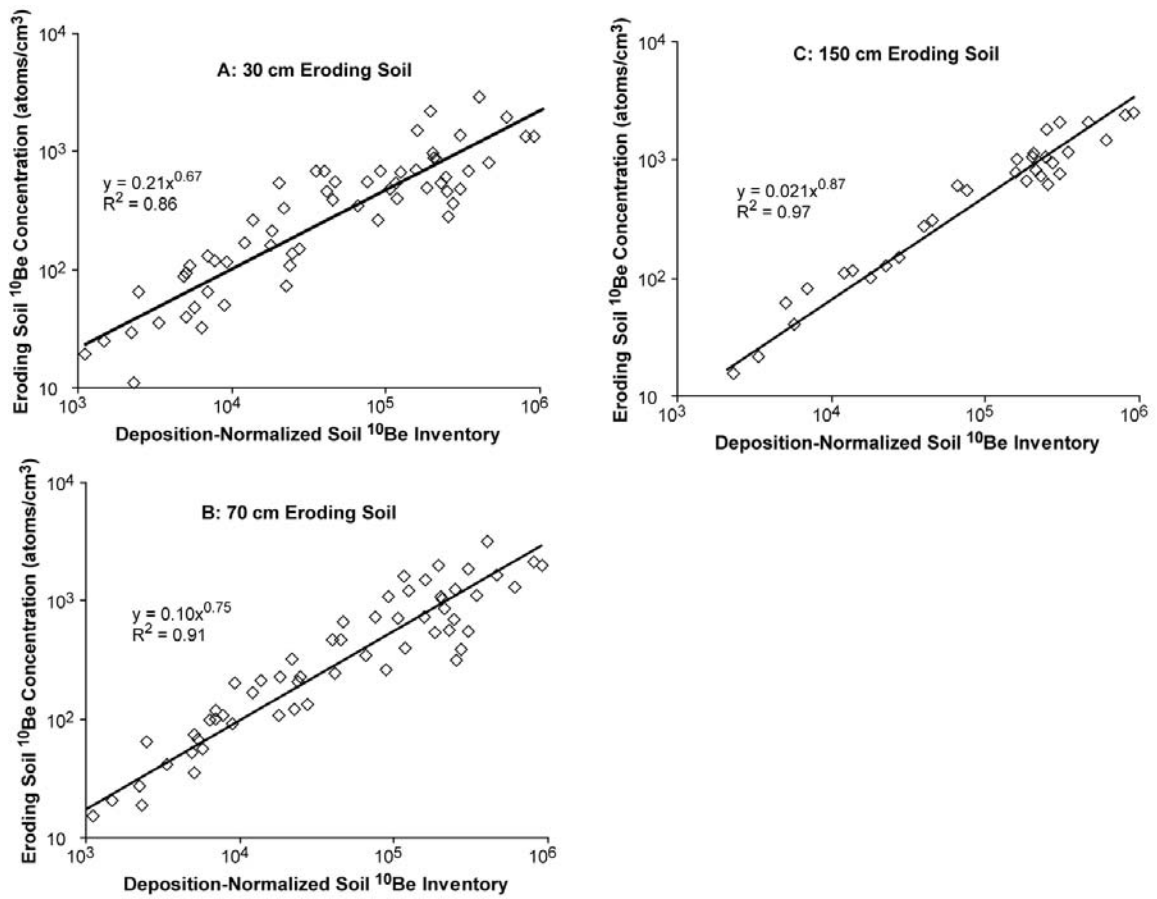


Figure D1: Relationship between meteoric <sup>10</sup>Be inventory and the average meteoric <sup>10</sup>Be concentration in the first 30 cm (A), 70 cm (B), 150 cm (C) in temperate mid-latitude soils (Graly et al., Submitted). Both inventory and concentration data have been divided by the local deposition rate.

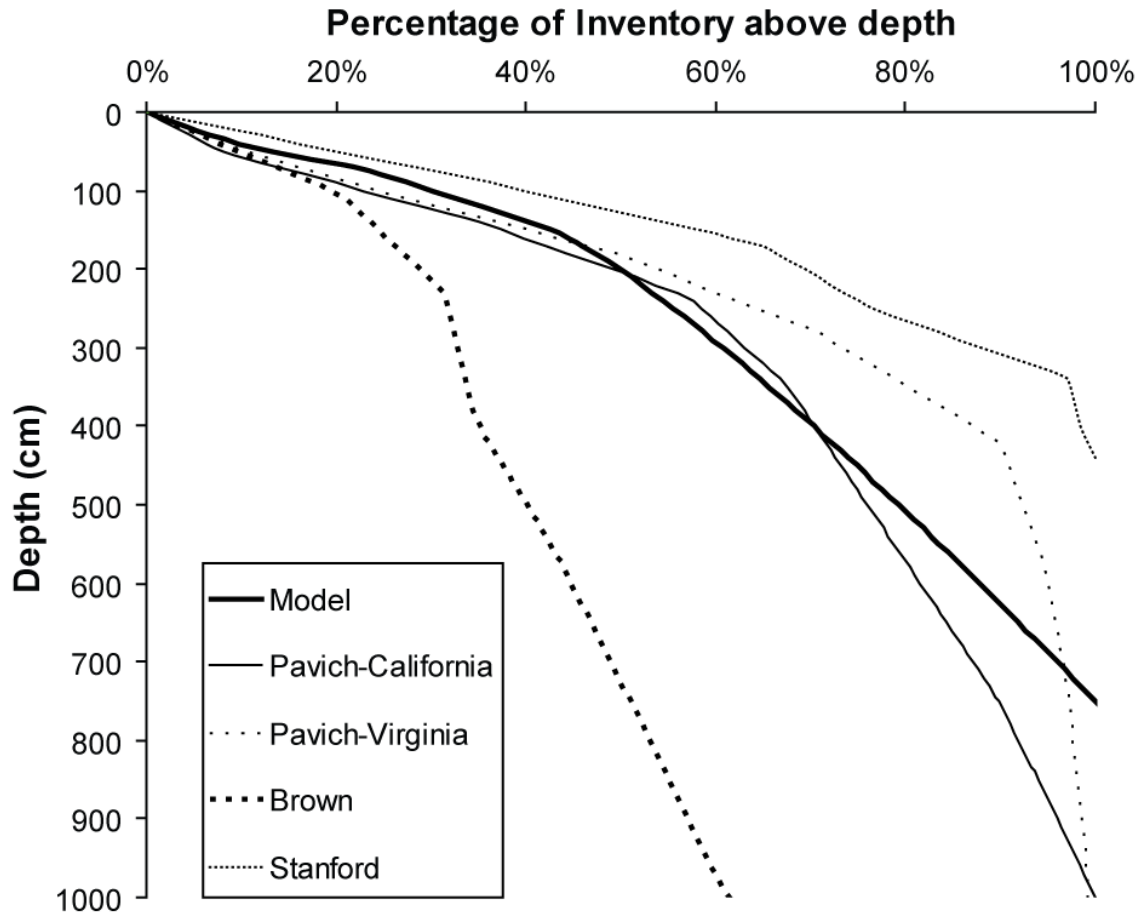


Figure D2: Model of meteoric  $^{10}\text{Be}$  distribution with depth assuming a meteoric  $^{10}\text{Be}$  inventory of  $3.7 \cdot 10^{11}$  atoms $\cdot\text{cm}^{-2}$  and deposition rate of  $3.5 \cdot 10^5$  atoms $\cdot\text{cm}^{-2}\cdot\text{yr}^{-1}$  compared to depth distribution of published deep regolith cores (Brown et al., 1988; Pavich et al., 1986; Stanford et al., 2000).

## Chapter 7: Conclusions

This project has advanced the use of the rare isotope meteoric  $^{10}\text{Be}$ , both by initiating its measurement in basal ice sediment and by developing a new framework for its interpretation. The framework arises out of the compilation of published meteoric  $^{10}\text{Be}$  measurements in soil and the development of a model of typical meteoric  $^{10}\text{Be}$  distribution with depth. Comparison of such a wide range of data also allows for the testing of the correlation of meteoric  $^{10}\text{Be}$  concentration in soils to a wide range of other soil properties. While this comparison confirms meteoric  $^{10}\text{Be}$ 's affinity for clay and oxyhydroxide phases, it shows the soil distribution of meteoric  $^{10}\text{Be}$  is complex and not tied to any one chemical or physical soil property. Despite this complexity, the concentration of meteoric  $^{10}\text{Be}$  with depth can be predicted from total meteoric  $^{10}\text{Be}$  inventory by analyzing the trends in large datasets of soils. These trends predict meteoric  $^{10}\text{Be}$  concentration from meteoric  $^{10}\text{Be}$  inventory with a power-law root mean square error typically less than 2.

The synthetic analysis of meteoric  $^{10}\text{Be}$  deposition rates provides an approximate formula that predicts deposition rate for any latitude and precipitation rate. It also demonstrates that meteoric  $^{10}\text{Be}$  in contemporary deposition can approximate long-term meteoric  $^{10}\text{Be}$  delivery to soil. The uncertainty associated with this approximation remains undetermined, as direct comparison of short and long term meteoric  $^{10}\text{Be}$  deposition rates is only currently available for a few sites. Nevertheless, this analysis suggests that Greenland's mid-Holocene meteoric  $^{10}\text{Be}$  deposition rates may approximate pre-Quaternary conditions.

While meteoric  $^{10}\text{Be}$  concentrations in sampled ice-bound fine sediment definitively indicate >10 ka of exposure in the southern Greenland Ice Sheet and >50 ka of exposure in the northern Greenland Ice Sheet, the timing of this exposure remains uncertain. In particular, the contributions of pre-glacial meteoric  $^{10}\text{Be}$  accumulation and interglacial meteoric  $^{10}\text{Be}$  accumulation cannot be definitively determined. Modeling of interglacial period exposure and glacial period erosion allows some constraint of meteoric  $^{10}\text{Be}$  source. High meteoric  $^{10}\text{Be}$  concentrations are found in northern Greenland because sediment beneath the northern Greenland Ice Sheet erodes slowly, less than 5 m/My. Preservation of pre-glacial regolith is necessary when a uniform erosion rate is applied. If sufficiently long interglacial periods assumed, the model shows southern Greenland to have higher erosion rates and lack any preserved pre-glacial regolith. Because independent evidence shows southern Greenland's erosion rates to indeed be at least ~10 m/My, the measured meteoric  $^{10}\text{Be}$  concentrations imply temporally extensive retreat of the Greenland Ice Sheet's Southern Dome during past interglacial periods.

These conclusions about the long-term history of the Greenland Ice Sheet fit within an expanding body of knowledge. The half-dozen modeling studies that predict total or near-total Eemian period melting of the Greenland Ice Sheet's Southern Dome are partially validated by these meteoric  $^{10}\text{Be}$  results. Still lacking is any control on the total retreat distance. Meteoric  $^{10}\text{Be}$  measurements in sediment from beneath the ice bed within the interior of Greenland would greatly constrain the uncertainties of past

retreat extent. Such measurements are likely to be performed as part of my doctoral research at the University of Wyoming.

The low erosion rates in the northern Greenland Ice Sheet are consistent with studies of Pleistocene erosion at high latitudes. Most of these studies have focused on bedrock surfaces. The meteoric  $^{10}\text{Be}$  results show high latitude ice to be largely non-erosive of sediment as well. Further measurements here would constrain the geographic extent of this low erosion and landscape preservation. Measurements from areas of fast glacial flow such as Sermeq Kujalleq (Jakobshavn Isbræ) or the Northeast Greenland Ice Stream would test the uniformity of these erosion rates.

This thesis tentatively supports the conclusion that during past warm periods, the Southern Dome of the Greenland Ice Sheet experienced several prolonged periods of retreat beyond its present boundaries. This conclusion is not necessarily new, but it bases on direct evidence what had previously been mostly inferred from models. Warming temperatures will likely cause such ice sheet retreat to occur again. This thesis does not constrain the rate of past or future ice retreat nor does it provide a temperature at which retreat might commence. These crucial questions can only be answered through further work. This thesis aids the study of these questions chiefly by developing a new method for constraining the extent of past ice sheet retreats. As this method is applied more widely, more definitive results may be possible.

## Cited References

- Aalbersberg, G., and Litt, T., 1998, Multiproxy climate reconstructions for the Eemian and Early Weichselian: *Quaternary Science Reviews*, v. 13, p. 367-390.
- Adler, R.F., Huffman, G.J., Chang, A., Ferraro, R., Xie, P.-P., Janowiak, J., Rudolf, B., Schneider, U., Curtis, S., Bolvin, D., Gruber, A., Susskind, J., Arkin, P., and Nelkin, E., 2003, The version-2 Global Precipitation Climatology Project (GPCP) monthly precipitation analysis (1979-present): *Journal of Hydrometeorology*, v. 4, p. 1147-1167.
- Aldahan, A., and Possnert, G., 1998, A high-resolution  $^{10}\text{Be}$  profile from deep sea sediment covering the last 70 ka: indication from globally synchronized environmental events: *Quaternary Geochronology*, v. 17, p. 1023-1032.
- Aldahan, A., Possnert, G., and Vintersved, I., 2001, Atmospheric interactions at northern high latitudes from weekly Be-isotopes in surface air: *Applied Radiation and Isotopes*, v. 54, p. 345-353.
- Alley, R.B., Clark, P.U., Huybrechts, P., and Joughin, I., 2005, Ice-sheet and sea-level changes: *Science*, v. 310, p. 456-460.
- Alley, R.B., Cuffey, K.M., Evenson, E.B., Strasser, J.C., Lawson, D.E., and Larson, G.J., 1997, How glaciers entrain and transport basal sediment: physical constraints: *Quaternary Science Reviews*, v. 16, p. 1017-1038.
- Alley, R.B., Lawson, D.E., Evenson, E.B., Strasser, J.C., and Larson, G.J., 1998, Glaciohydraulic supercooling: a freeze-on mechanism to create stratified, debris-rich basal ice: II Theory: *Journal of Glaciology*, v. 44, p. 563-569.
- Alley, R.B., Lawson, D.E., Larson, G.J., Evenson, E.B., and Baker, G.S., 2003, Stabilizing feedbacks in glacier-bed erosion: *Nature*, v. 424, p. 758-760.
- Amin, B.S., Lal, D., and Somayajulu, B.L.K., 1975, Chronology of marine sediments using the  $^{10}\text{Be}$  method: intercomparison with other methods: *Geochimica et Cosmochimica Acta*, v. 39, p. 1187-1192.
- Anderson, R.S., Repka, J.L., and Dick, G.S., 1996, Explicit treatment of inheritance in dating depositional surfaces using in situ  $^{10}\text{Be}$  and  $^{26}\text{Al}$ : *Geology*, v. 24, p. 47-51.
- Andrews, J.T., Millman, J.D., Jennings, A.E., Rynes, N., and Dwyer, J., 1994, Sediment Thickness of Holocene Glacial Marine Sedimentation Rates in Three East Greenland Fjords (ca. 68°N): *Journal of Geology*, v. 102, p. 669-683.
- Asano, M., 2007, Dynamics of pedogenic carbonate carbon under vegetation sequence in Mongolia: Japan, University of Tsukuba.
- Balco, G., Stone, J.O., Lifton, N.A., and Dunai, T.J., 2008, A complete and easily accessible means of calculating surface exposure ages or erosion rates from  $^{10}\text{Be}$  and  $^{26}\text{Al}$  measurements: *Quaternary Geochronology*, v. 3, p. 174-195.
- Balco, G.A., 2004, The sedimentary record of subglacial erosion beneath the Laurentide Ice Sheet: Seattle, University of Washington.
- Bamber, J.L., Layberry, R.L., and Gogineni, S.P., 2001, A new ice thickness and bed data set for the Greenland ice sheet 1. Measurement, data reduction, and errors: *Journal of Geophysical Research*, v. 106, p. 33773-33780.

- Barg, E., Lal, D., Pavich, M.J., Caffee, M.W., and Southon, J.R., 1997, Beryllium geochemistry in soils; evaluation of  $^{10}\text{Be}/^{9}\text{Be}$  ratios in authigenic minerals as a basis for age models: *Chemical Geology*, v. 140, p. 237-258.
- Baumgartner, S., Beer, J., Wagner, G., Kubik, P., Suter, M., Raisbeck, G.M., and Yiou, F., 1997,  $^{10}\text{Be}$  and dust: *Nuclear Instruments and Methods in Physics Research B*, v. 123, p. 296-301.
- Beer, J., Andree, M., Oescher, H., Siegenthaler, U., Bonani, G., Hofmann, H., Morezoni, E., Nessi, M., Suter, M., Wölfi, W., Finkel, R., and Langway, C., 1984, The Camp Century  $^{10}\text{Be}$  record: Implications for long-term variations of the geomagnetic dipole moment: *Nuclear Instruments and Methods in Physics Research B*, v. 5.
- Beer, J., Joos, F., Lukaczyk, C., Mende, W., Rodriguez, J., Siegenthaler, U., and Stellmacher, R., 1994,  $^{10}\text{Be}$  as an indicator of solar variability and climate, *in* Nesme-Ribes, E., ed., *The solar engine and its influence on terrestrial atmosphere and climate*: Berlin, Springer-Verlag, p. 221-233.
- Bell, M., and Laine, E.P., 1985, Erosion of the Laurentide Region of North America by glacial and glaciofluvial processes: *Quaternary Research*, v. 23, p. 154-174.
- Belmaker, R., Lazar, B., Tepelyakov, N., Stein, M., and Beer, J., 2008,  $^{10}\text{Be}$  in Lake Lisan sediments - A proxy for production or climate?: *Earth and Planetary Science Letters*, v. 269, p. 448-457.
- Bennike, O., and Bocher, J., 1994, Land biotas of the last interglacial cycle on Jameson Land, East Greenland: *Boreas*, v. 23, p. 479-487.
- Bensen, C.S., 1962, Stratigraphic studies in the snow and firn of Greenland, SIPRE Research Report.
- Berggren, A.-M., Beer, J., Possnert, G., Aldahan, A., Kubik, P., Christl, M., Johnsen, S.J., Abreu, J., and Vinther, B.M., 2009, A 600-year annual  $^{10}\text{Be}$  record from the NGRIP ice core, Greenland: *Geophysical Research Letters*, v. 46, p. L11801.
- Bierman, P.R., 1994, Using in situ produced cosmogenic isotopes to estimate rates of landscape evolution: A review from the geomorphic perspective: *Journal of Geophysical Research*, v. 99, p. 13885-13896.
- Bierman, P.R., and Caffee, M., 2001, Slow rates of rock surface erosion and sediment production across the Namib Desert and Escarpment, Southern Africa: *American Journal of Science*, v. 302, p. 326-358.
- Bierman, P.R., Marsella, K.A., Patterson, C., Davis, P.T., and Caffee, M., 1999, Mid-Pleistocene cosmogenic minimum-age limits for pre-Wisconsinan glacial surfaces in southwestern Minnesota and southern Baffin Island: a multiple nuclide approach: *Geomorphology*, v. 27, p. 25-39.
- Birkeland, P.W., 1999, *Soils and Geomorphology*, 3rd edition: Oxford, University Press.
- Bitanja, R., and van de Wal, R.S.W., 2008, North American ice-sheet dynamics and the onset of the 100,000-year glacial cycles: *Nature*, v. 454, p. 869-872.
- Bouchard, M., and Pavich, M.J., 1989, Characteristics and significance of pre-Wisconsinan saprolites in the northern Appalachians: *Zeitschrift für Geomorphologie*, v. 72, p. 125-137.
- Braun, A., Kim, H.R., Csatho, B., and Frese, R.R.B.v., 2007, Gravity-inferred crustal thickness of Greenland: *Earth and Planetary Science Letters*, v. 262, p. 138-158.

- Briner, J.P., Miller, G.H., Davis, T.P., and Finkel, R.C., 2006, Cosmogenic radionuclides from fiord landscapes support differential erosion by overriding ice sheets: *GSA Bulletin*, v. 118, p. 406-420.
- Briner, J.P., and Swanson, T.W., 1998, Using inherited cosmogenic  $^{36}\text{Cl}$  to constrain glacial erosion rates of the Cordilleran ice sheet: *Geology*, v. 26, p. 3-6.
- Brown, E.T., Edmond, J.M., Raisbeck, G.M., Bourlès, D.L., Yiou, F., and Measures, C.I., 1992, Beryllium isotope geochemistry in tropical river basins: *Geochimica et Cosmochimica Acta*, v. 56, p. 1607-1624.
- Brown, L., Pavich, M.J., Hickman, R.E., Klein, J., and Middleton, R., 1988, Erosion of the eastern United States observed with  $^{10}\text{Be}$ : *Earth Surface Processes and Landforms*, v. 13, p. 441-457.
- Brown, L., Stensland, G.J., Klein, J., and Middleton, R., 1989, Atmospheric deposition of  $^7\text{Be}$  and  $^{10}\text{Be}$ : *Geochimica et Cosmochimica Acta*, v. 53, p. 135-142.
- Christl, M., Strobl, C., and Mangini, A., 2003, Beryllium-10 in deep-sea sediments: a tracer for the Earth's magnetic field intensity during the last 200,000 years: *Quaternary Science Reviews*, v. 22, p. 725-739.
- Clark, D.H., Bierman, P.R., and Larsen, P., 1995, Improving *in situ* cosmogenic chronometers: *Quaternary Research*, v. 44, p. 367-377.
- Cockburn, H.A.P., and Summerfield, M.A., 2004, Geomorphological applications of cosmogenic isotope analysis: *Progress in Physical Geography*, v. 28, p. 1-42.
- Cohen, D., Hooyer, T.S., Iverson, N.R., Thomason, J.F., and Jackson, M., 2006, Role of transient water pressure in quarrying: A subglacial experiment using acoustic emissions: *Journal of Geophysical Research*, v. 111, p. F03006.
- Coleman, M.L., Shepherd, T.J., Durham, J.J., Rouse, J.E., and Moore, G.R., 1982, Reduction of water with zinc for hydrogen isotope analysis: *Analytical Chemistry*, v. 54, p. 993-995.
- Colgan, P.M., Bierman, P.R., Mickelson, D.M., and Caffee, M., 2002, Variation in glacial erosion near the southern margin of the Laurentide Ice Sheet, south-central Wisconsin, USA: Implications for cosmogenic dating of glacial terrains: *GSA Bulletin*, v. 114, p. 1581-1591.
- Cook, S.J., Waller, R.I., and Knight, P.G., 2006, Glaciohydraulic supercooling: the process and its significance: *Progress in Physical Geography*, v. 30, p. 577-588.
- Craig, H., 1961, Isotopic variations in meteoric water: *Science*, v. 133, p. 1702-1703.
- Cuffey, K.M., and Alley, R.B., 1996, Is erosion by deforming subglacial sediments significant? (Toward till continuity): *Annals of Glaciology*, v. 22, p. 17-24.
- Cuffey, K.M., and Clow, G.D., 1997, Temperature, accumulation, and ice sheet elevation in central Greenland through the last deglacial transition: *Journal of Geophysical Research*, v. 102, p. 26383-26396.
- Cuffey, K.M., Clow, G.D., Alley, R.B., Stuiver, M., Waddington, E.D., and Saltus, R.W., 1995, Large arctic temperature change at the Wisconsin-Holocene glacial transition: *Science*, v. 270, p. 455-458.
- Cuffey, K.M., Conway, H., Gades, A.M., Hallet, B., Lorrain, R., Severinghaus, J.P., Steig, E.J., and Vaughn, J.W.C., 2000, Entrainment at cold glacier beds: *Geology*, v. 28, p. 351-354.

- Cuffey, K.M., and Marshall, S.J., 2000, Substantial contribution to sea-level rise during the last interglacial from the Greenland ice sheet: *Nature*, v. 404, p. 591-594.
- Curry, B.B., and Pavich, M.J., 1996, Absence of glaciation in Illinois during Marine Isotope Stages 3 through 5: *Quaternary International*, v. 46, p. 19-26.
- Dansgaard, W., Clausen, H.B., Gundestrup, N., Hammer, C.U., Johnsen, S.F., Kristinsdottir, P.M., and Reeh, N., 1982, A New Greenland Deep Ice Core: *Science*, v. 218, p. 1273-1277.
- Darmondy, R.G., Thorn, C.E., Seppälä, M., Campbell, S.W., Li, Y.K., and Harbor, J., 2008, Age and weathering status of granite tors in Arctic Finland (~68° N): *Geomorphology*, v. 94, p. 10-23.
- Dean, W.E., and Schwalb, A., 2000, Holocene environmental and climatic change in the Northern Great Plains as recorded in the geochemistry of sediments in Pickerel Lake, South Dakota: *Quaternary International*, v. 67, p. 5-20.
- Dibb, J.E., Meeker, L.D., Finkel, R.C., Southon, J.R., Caffee, M.W., and Barrie, L.A., 1994, Estimation of stratospheric input to the Arctic troposphere:  $^7\text{Be}$  and  $^{10}\text{Be}$  in aerosols at Alert, Canada: *Journal of Geophysical Research*, v. 99, p. 12855-12864.
- Dowdeswell, J.A., Ottesen, D., and Rise, L., 2010, Rates of sediment delivery from the Fennoscandian Ice Sheet through an ice age: *Geology*, v. 38, p. 3-6.
- Drewry, D., 1986, *Glacial Geologic Processes*: London, Edward Arnold, 276 p.
- Egli, M., Brandová, D., Böhlert, R., Favilli, F., and Kubik, P.W., 2010,  $^{10}\text{Be}$  inventories in Alpine soils and their potential for dating land surfaces: *Geomorphology*, v. 119, p. 62-73.
- Eisenhauer, A., Spielhagen, R.F., Frank, M., Hentzschel, G., Mangini, A., Kubik, P.W., Dittrich-Hanner, B., and Billen, T., 1994,  $^{10}\text{Be}$  records of sediment cores from high latitudes: Implications for environmental and climatic changes: *Earth and Planetary Science Letters*, v. 124, p. 171-184.
- Eleverhøi, A., Hooke, R.L., and Solheim, A., 1998, Late Cenozoic erosion and sediment yield from the Salvard-Barents Sea region: implications for understanding erosion of glacierized basins: *Quaternary Science Reviews*, v. 17, p. 209-241.
- Elmore, D., and Phillips, F.M., 1987, Accelerator mass spectrometry for measurement of long-lived radioisotopes: *Science*, v. 236, p. 543-550.
- Fabel, D., Stoeven, A.P., Harbor, J., Kleman, J., Elmore, D., and Fink, D., 2002, Landscape preservation under Fennoscandian ice sheets determined from in situ produced  $^{10}\text{Be}$  and  $^{26}\text{Al}$ : *Earth and Planetary Science Letters*, v. 201, p. 397-406.
- Fahnestock, M., Abdalati, W., Luo, S., and Gogineni, S., 2001, Internal layer tracing and age-depth-accumulation relationships for the northern Greenland ice sheet: *Journal of Geophysical Research*, v. 106, p. 33,789-33,797.
- Field, C.V., Schmidt, G.A., Koch, D., and Salyk, C., 2006, Modeling production and climate-related impacts on  $^{10}\text{Be}$  concentration in ice cores: *Journal of Geophysical Research*, v. 111, p. D15107.
- Fifield, L.K., Wasson, R.J., Pillans, B., and Stone, J.O.H., 2010, The longevity of hillslope soil in SE and NW Australia: *Catena*, v. 81, p. 32-42.

- Finkel, R.C., and Nishiizumi, K., 1997, Beryllium 10 concentrations in the Greenland Ice Sheet Project 2 ice core from 3-40 ka: *Journal of Geophysical Research*, v. 102, p. 26699-26706.
- Frank, M., Schwarz, B., Baumann, S., Kubik, P.W., Suter, M., and Mangini, A., 1997, A 200 kyr record of cosmogenic radionuclide production rate and geomagnetic field intensity from  $^{10}\text{Be}$  in globally stacked deep-sea sediments: *Earth and Planetary Science Letters*, v. 149, p. 121-129.
- Funder, S., Abrahamsen, N., Bennike, O., and Feyling-Hanssen, R.W., 1985, Forested arctic: Evidence from North Greenland: *Geology*, v. 13, p. 542-546.
- Glasser, N.F., and Hall, A.M., 1997, Calculating Quaternary glacial erosion rates in northeast Scotland: *Geomorphology*, v. 20, p. 29-48.
- Goehring, B.M., Kelly, M.A., Schaefer, J.M., Finkel, R.C., and Lowell, T.V., 2010, Dating of raised marine and lacustrine deposits in east Greenland using beryllium-10 depth profiles and implications for estimates of subglacial erosion: *Journal of Quaternary Science*, p. DOI: 10.1002/jps.
- Gomez, B., Carter, L., Trustrum, N.A., Palmer, A.S., and Roberts, A.P., 2004, El Niño-Southern Oscillation signal associated with middle Holocene climate change in intercorrelated terrestrial and marine sediment cores, North Island, New Zealand: *Geology*, v. 32, p. 653-656.
- Graham, I., Ditchburn, R., and Barry, B., 2003, Atmospheric deposition of  $^7\text{Be}$  and  $^{10}\text{Be}$  in New Zealand rain (1996-98): *Geochimica et Cosmochimica Acta*, v. 67, p. 361-373.
- Graham, I.J., Ditchburn, R.G., Claridge, G.G.C., Whitehead, N.E., Zondervan, A., and Sheppard, D.S., 2002, Dating Antarctic soils using atmosphere-derived  $^{10}\text{Be}$  and nitrate: *Royal Society of New Zealand Bulletin*, v. 35, p. 429-436.
- Graham, I.J., Ditchburn, R.G., and Whitehead, N.E., 2001, Be isotope analysis of a 0-500 ka loess-paleosol sequence from Rangitatau East, New Zealand: *Quaternary International*, v. 76/77, p. 29-42.
- Graly, J.A., Bierman, P.R., Reusser, L.J., and Pavich, M.J., Submitted, Meteoric  $^{10}\text{Be}$  in soil profiles – a global meta-analysis: *Geochimica et Cosmochimica Acta*.
- Greve, R., 2005, Relation of measured basal temperatures and the spatial distribution of geothermal heat flux for the Greenland ice sheet: *Annals of Glaciology*, v. 42, p. 424-432.
- Gu, Z.Y., Lal, D., Liu, T.S., Southon, J., Caffee, M.W., Guo, Z.T., and Chen, M.Y., 1996, Five million year  $^{10}\text{Be}$  record in Chinese loess and red-clay: climate and weathering relationships: *Earth and Planetary Science Letters*, v. 144, p. 273-287.
- Guyodo, Y., and Valet, J.P., 1996, Relative variations in geomagnetic intensity from sedimentary records: the past 200 thousand years: *Earth and Planetary Science Letters*, v. 143, p. 23-36.
- Håkansson, L., Briner, J., Alexanderson, H., Aldahan, A., and Possnert, G., 2007,  $^{10}\text{Be}$  ages from central east Greenland constrain the extent of the Greenland ice sheet during the Last Glacial Maximum: *Quaternary Science Reviews*, v. 26, p. 2316-2321.

- Hallet, B., 1996, Glacial quarrying a simple theoretical model: *Annals of Glaciology*, v. 22, p. 1-8.
- Hallet, B., Hunter, L., and Bogen, J., 1996, Rates of erosion and sediment evacuation by glaciers: A review of field data and their implications: *Global and Planetary Change*, v. 12, p. 213-235.
- Hansen, J., 2005, A Slippery Slope: How much global warming constitutes "dangerous anthropogenic interference"?: *Climate Change*, v. 68, p. 269-279.
- Harden, J.W., 1987, Soils developed in granitic alluvium near Merced, California: *US Geological Survey Bulletin* v. 1590A, p. 1-65.
- Harden, J.W., Fries, T.L., and Pavich, M.J., 2002, Cycling of Beryllium and Carbon through hillslope soils in Iowa: *Biogeochemistry*, v. 60, p. 317-336.
- Harrison, C.H., 1973, Radio echo sounding of horizontal layers in ice: *Journal of Glaciology*, v. 12, p. 383-397.
- Haskell, B.J., Engstrom, D.R., and Fritz, S.C., 1996, Late Quaternary paleohydrology in the North American Great Plains inferred from geochemistry of endogenic carbonate and fossil ostracodes from Devils Lake, North Dakota, USA: *Palaeogeography, Palaeoclimatology, Palaeoecology*, v. 124.
- Hay, W.W., Shaw, C.A., and Wold, C.N., 1989, Mass-balanced paleogeographic reconstructions: *Geologische Rundschau*, v. 78, p. 207-242.
- Heikkilä, U., Beer, J., and Alfimov, V., 2008a, Beryllium-10 and beryllium-7 in precipitation in Dübendorf (440 m) and Jungfraujoch (3580 m), Switzerland (1998-2005): *Journal of Geophysical Research*, v. 113, p. D11104.
- Heikkilä, U., Beer, J., and Feichter, J., 2008b, Modeling cosmogenic radionuclides  $^{10}\text{Be}$  and  $^7\text{Be}$  during the Meander Minimum using the ECHAM5-HAM General Circulation Model: *Atmospheric Chemistry and Physics*, v. 8, p. 2797-2809.
- , 2009, Meridional transport and deposition of atmospheric  $^{10}\text{Be}$ : *Atmospheric Chemistry and Physics*, v. 9, p. 515-527.
- Heikkilä, U., Beer, J., Jouzel, J., Feichter, J., and Kubik, P., 2008c,  $^{10}\text{Be}$  measured in a GRIP snow pit and modeled using the ECHAM5-HAM general circulation model: *Geophysical Research Letters*, v. 35.
- Hessell, J.W.D., 1980, The climate and weather of the Gisborne Region, Volume 115, *New Zealand Meteorological Service*, p. 30.
- Hoffmann, W., 1975, Die Internationale Glaziologische Grönland-Expedition (EGIG). 2. Die geodätische Lagemessung-Eisbewegung 1959-1967 in den EGIG-Profilen: *Zeitschrift für Gletscherkunde und Glazialgeologie*, v. 10, p. 217-224.
- Horiuchi, K., Ohta, A., Uchida, T., Matsuzaki, H., Shibata, Y., and Motoyama, H., 2007, Concentration of  $^{10}\text{Be}$  in an ice core from the Dome Fuji station, Eastern Antarctica: Preliminary results from 1500 to 1810 yr AD: *Nuclear Instruments and Methods in Physics Research B*, v. 259, p. 584-587.
- Hubbard, B., and Sharp, M., 1993, Weertman regelation, multiple refreezing events and the isotopic evolution of the basal ice layer: *Journal of Glaciology*, v. 39, p. 275-291.
- Huh, C.-A., 1999, Dependence of the decay rate of  $^7\text{Be}$  on chemical forms: *Earth and Planetary Science Letters*, v. 171, p. 325-328.

- Huybrechts, P., 2002, Sea-level changes at the LGM from ice-dynamic reconstructions of Greenland and Antarctic ice sheets during the glacial cycles: *Quaternary Science Reviews*, v. 21, p. 203-231.
- , 2006, Numerical modelling of polar ice sheets through time, *in* Knight, P.G., ed., *Glacier Science and Environmental Change*.
- Iverson, N.R., 1991, Potential effects of subglacial water-pressure fluctuations on quarrying: *Journal of Glaciology*, v. 37, p. 27-36.
- , 1993, Regelation of ice through debris at glacier beds: Implications for sediment transport: *Geology*, v. 21, p. 559-562.
- Iverson, N.R., and Semmens, D.J., 1995, Intrusion of ice porous media by regelation: A mechanism of sediment entrainment by glaciers: *Journal of Geophysical Research*, v. 100, p. 10219-10230.
- Iverson, N.R., and Souchez, R., 1996, Isotopic signature of debris-rich ice formed by regelation into a subglacial sediment bed: *Geophysical Research Letters*, v. 23, p. 1151-1154.
- Johnsen, S.F., Dansgaard, W., and White, J.W.C., 1989, The origin of Arctic precipitation under present and glacial conditions: *Tellus*, v. 41B, p. 452-468.
- Jordan, C.E., Dibb, J.E., and Finkel, R.C., 2003,  $^{10}\text{Be}/^7\text{Be}$  tracer of atmospheric transport and stratosphere-troposphere exchange: *Journal of Geophysical Research*, v. 108, p. 4234.
- Jouzel, J., Stievenard, M., Johnsen, S.J., Landais, A., Masson-Delmotte, V., Sveinbjornsdottir, A., Vimeux, F., von Grafenstein, U., and White, J.W.C., 2007, The GRIP deuterium-excess record: *Quaternary Science Reviews*, v. 26, p. 1-17.
- Jungers, M.C., Bierman, P.R., Matmon, A., Nichols, K., Larsen, J., and Finkel, R., 2009, Tracing hillslope sediment production and transport with *in situ* and meteoric  $^{10}\text{Be}$ : *Journal of Geophysical Research – Earth Surface*, v. 114, p. F04020.
- Kaszycski, C.A., and Shilts, W.W., 1987, Glacial erosion of the Canadian Shield, *in* Graf, W.L., ed., *Geomorphic Systems of North America*: Boulder, Geological Society of America.
- Klein, J., Middleton, R., and Tang, H., 1982, Modifications of an FN tandem for quantitative  $^{10}\text{Be}$  measurement: *Nuclear Instruments and Methods in Physics Research*, v. 193, p. 3895-3899.
- Knight, P.G., and Cook, S.J., 2008, Glaciohydraulic supercooling: *Progress in Physical Geography*, v. 32, p. 65-71.
- Knight, P.G., Waller, R.I., Patterson, C.J., Jones, A.P., and Robinson, Z.P., 2002, Discharge of debris from ice at the margin of the Greenland ice sheet: *Journal of Glaciology*, v. 48, p. 192-198.
- Korschinek, G., Bergmaier, A., Faestermann, T., Gerstmann, U.C., Knie, K., Rugel, G., Wallner, A., Dillmann, I., Dollinger, G., von Gostomski, C.L., Kossert, K., Poutivtsev, M., and Remmert, A., 2010, A new value for the half-life of  $^{10}\text{Be}$  by heavy-ion elastic recoil detection and liquid scintillation counting: *Nuclear Instruments and Methods in Physics Research B*, v. 268, p. 187-191.
- Korschinek, G., Bergmaier, A., Faestermann, T., Gerstmann, U.C., Knie, K., Rugel, G., Wallner, A., Dillmann, I., Dollinger, G., von Gostomski, C.L., Kossert, K.,

- Poutivtsev, M., and Remmert, A., 2010, A new value for the half-life of  $^{10}\text{Be}$  by heavy-ion elastic recoil detection and liquid scintillation counting: *Nuclear Instruments and Methods in Physics Research B*, v. 268, p. 187-191.
- Laine, E.P., 1980, New evidence from beneath the Western North Atlantic for the depth of glacial erosion in Greenland and North America: *Quaternary Research*, v. 14, p. 188-198.
- Lal, D., 1988, In-situ produced cosmogenic isotopes in terrestrial rocks: *Annual Review of Earth and Planetary Sciences*, v. 16, p. 355-388.
- , 2001, New nuclear methods for studies of soil dynamics utilizing cosmic ray produced radionuclides, *in* Scott, D.E., Mohtar, R.H., and Steinhart, G.C., eds., *Sustain the Global Farm: Selected papers from the 10th International Soil Conservation Organization Meeting held May 24-29 at Purdue University and the USDA-ARS National Soil Erosion Research Laboratory: West Lafayette, Purdue University*, p. 1044-1052.
- Lal, D., and Peters, B., 1967, Cosmic-ray produced radioactivity on earth, *Handbook of Physics*: Berlin, Springer-Verlag, p. 551-612.
- Lao, Y., Anderson, R.F., Broecker, W.S., Trumbore, S.E., Hofmann, H.J., and Wolfli, W., 1992, Increased production of cosmogenic  $^{10}\text{Be}$  during the Last Glacial Maximum: *Nature*, v. 357, p. 576-579.
- Larson, G.J., Lawson, D.E., Evenson, E.B., Alley, R.B., Knudsen, O., Lachniet, M.S., and Goetz, S.L., 2006, Glaciohydraulic supercooling in former ice sheets?: *Geomorphology*, v. 75, p. 20-32.
- Lawson, D.E., Strasser, J.C., Evenson, E.B., Alley, R.B., Larson, G.J., and Arcone, S.A., 1998, Glaciohydraulic supercooling: a freeze-on mechanism to create stratified, debris-rich basal ice: *Journal of Glaciology*, v. 44, p. 547-562.
- Letreguilly, A., Reeh, N., and Huybrechts, P., 1991, The Greenland ice sheet through the glacial-interglacial cycle: *Global and Planetary Change*, v. 3, p. 385-394.
- Lhomme, N., Clarke, G.K., and Marshall, S.J., 2005, Tracer transport in the Greenland Ice Sheet: constraints on ice cores and glacial history: *Quaternary Science Reviews*, v. 24, p. 173-194.
- Li, J., Jacka, T.H., and Budd, W.F., 1996, Deformation rates in combined compression and shear for ice which is initially isotropic and after the development of strong anisotropy: *Annals of Glaciology*, v. 23, p. 247-252.
- Lidmar-Bergström, K., 1997, A long-term perspective on glacial erosion: *Earth Surface Processes and Landforms*, v. 22, p. 297-306.
- Lisiecki, L.E., and Raymo, M.E., 2005, A Pliocene-Pleistocene stack of 57 globally distributed benthic  $\delta^{18}\text{O}$  records: *Paleoceanography*, v. 20, p. PA1003.
- Lliboutry, L., 1993, Internal melting and ice accretion at the bottom of temperate glaciers: *Journal of Glaciology*, v. 39, p. 50-64.
- Mackey, B.H., Roering, J.J., and McKean, J.A., 2009, Long-term kinematics and sediment flux of an active earthflow, Eel River, California: *Geology*, v. 37, p. 803-806.

- Maejima, Y., Matsuzaki, H., and Higashi, T., 2005, Application of cosmogenic  $^{10}\text{Be}$  to dating soils on the raised coral reef terraces of Kikai Island, southwest Japan: *Geoderma*, v. 126, p. 388-399.
- Maejima, Y., Matsuzaki, H., and Nakano, C., 2004,  $^{10}\text{Be}$  concentrations of red soils in Southwest Japan and its possibility of dating: *Nuclear Instruments and Methods in Physics Research B*, v. 223-224, p. 596-600.
- Markewich, H.W., Pavich, M.J., Mausbach, M.J., Hall, R.L., Johnson, R.G., and Hearn, P.P., 1987, Age relations between soils and geology in the coastal plain of Maryland and Virginia: *US Geological Survey Bulletin* v. 1589, p. 1-34.
- Marshall, S.J., and Cuffey, K.M., 2000, Peregrinations of the Greenland Ice Sheet divide in the last glacial cycle: implications for central Greenland ice cores: *Earth and Planetary Science Letters*, v. 179, p. 73-90.
- Masarik, J., and Beer, J., 1999, Simulation of particle fluxes and cosmogenic nuclide production in the Earth's atmosphere: *Journal of Geophysical Research*, v. 104, p. 12099-12111.
- , 2009, An updated simulation of particle fluxes and cosmogenic nuclide production in the Earth's atmosphere: *Journal of Geophysical Research*, v. 144, p. D11103.
- McHargue, L.R., and Damon, P.E., 1991, The global beryllium 10 cycle: *Reviews of Geophysics*, v. 29, p. 141-158.
- McKean, J.A., Dietrich, W.E., Finkel, R.C., Southon, J.R., and Caffee, M.W., 1993, Quantification of soil production and downslope creep rates from cosmogenic  $^{10}\text{Be}$  accumulations on a hillslope profile: *Geology*, v. 21, p. 343-346.
- Mock, S.J., and Weeks, W.F., 1966, The distribution of 10 meter snow temperatures on the Greenland ice sheet: *Journal of Glaciology*, v. 6, p. 23-41.
- Monaghan, M.C., Krishnaswami, S., and Thomas, J.H., 1983,  $^{10}\text{Be}$  concentrations and the long-term fate of particle-reactive nuclides in five soil profiles from California: *Earth and Planetary Science Letters*, v. 65, p. 51-60.
- Monaghan, M.C., Krishnaswami, S., and Turekian, K.K., 1986, The global-average production rate of  $^{10}\text{Be}$ : *Earth and Planetary Science Letters*, v. 76, p. 279-287.
- Monaghan, M.C., McKean, J.A., Dietrich, W.E., and Klein, J., 1992,  $^{10}\text{Be}$  chronometry of bedrock-to-soil conversion rates: *Earth and Planetary Science Letters*, v. 111, p. 483-492.
- Morris, J., Valentine, R., and Harrison, T., 2002,  $^{10}\text{Be}$  imaging of sediment accretion and subduction along the northeast Japan and Costa Rica convergent margins: *Geology*, v. 30, p. 59-62.
- Muhs, D.R., Ager, T.A., Bettis, E.A., McGeehin, J., Been, J.M., Beget, J.E., Pavich, M.J., Stafford, T.W., and Stevens, D.A.S.P., 2003, Stratigraphy and palaeoclimatic significance of Late Quaternary loess-Palaeosol sequences of the Last Interglacial-Glacial cycle in central Alaska: *Quaternary Science Reviews*, v. 22, p. 1947-1986.
- Nagai, H., Tada, W., and Kobayashi, T., 2000, Production rates of  $^7\text{Be}$  and  $^{10}\text{Be}$  in the atmosphere: *Nuclear Instruments and Methods in Physics Research B*, v. 172, p. 796-801.

- Nagatsuka, S., and Maejima, Y., 2001, Dating of soils on the raised coral reef terraces of Kikai Island in the Ryukyus, Southwest Japan: with special reference to the age of red-yellow soils: *Quaternary Research*, v. 40, p. 137-147.
- Ng, F.S.L., 2000, Canals under sediment-based ice sheets: *Annals of Glaciology*, v. 30, p. 146-152.
- Nishiizumi, K., Finkel, R.C., Ponganis, K.V., Graf, T., Kohl, C.P., and Marti, K., 1996, In situ produced cosmogenic nuclides in GISP2 rock core from Greenland summit: *Eos*, v. 77, p. OS41B-10.
- Nishiizumi, K., Imamura, M., Caffee, M., Southon, J.R., Finkel, R.C., and McAninch, J., 2007, Absolute calibration of  $^{10}\text{Be}$  standards: *Nuclear Instruments and Methods in Physics Research B*, v. 258, p. 403-413.
- Otto-Bliesner, B.L., Marshall, S.J., Overpeck, J.T., Miller, G.H., and Hu, A., 2006, Simulating arctic climate warmth and icefield retreat in the last interglacial: *Science*, v. 311, p. 1751-1753.
- Patrenko, V.V., Severinghaus, J.P., Brook, E.J., Reeh, N., and Schaefer, H., 2006, Gas records from the West Greenland ice margin covering the Last Glacial Termination: a horizontal ice core: *Quaternary Science Reviews*, v. 25, p. 865-875.
- Pavich, M., Vidic, N., and Lobnik, F., 1989, Geochemistry of soils on Quaternary terraces of the Sava River, Univerza Edvarda Kerdelja v Ljubljani.
- Pavich, M.J., Brown, L., Harden, J.W., Klein, J., and Middleton, R., 1986,  $^{10}\text{Be}$  distribution in soils from Merced River terraces, California: *Geochimica et Cosmochimica Acta*, v. 50, p. 1727-1735.
- Pavich, M.J., Brown, L., Klein, J., and Middleton, R., 1984,  $^{10}\text{Be}$  accumulation in a soil chronosequence: *Earth and Planetary Science Letters*, v. 68, p. 198-204.
- Pavich, M.J., Brown, L., Valette-Silver, J.N., Klein, J., and Middleton, R., 1985,  $^{10}\text{Be}$  analysis of a Quaternary weathering profile in the Virginia Piedmont: *Geology*, v. 13, p. 39-41.
- Pavich, M.J., and Vidic, N., 1993, Application of paleomagnetic and  $^{10}\text{Be}$  analyses to chronostratigraphy of alpine glacio-fluvial terraces, Sava River Valley, Slovenia: *Geophysical Monograph*, v. 78, p. 263-275.
- Pedro, J., van Ommen, T., Curran, M., Morgan, V., Smith, A., and McMorrow, A., 2006, Evidence for climate modulation of the  $^{10}\text{Be}$  solar activity proxy: *Journal of Geophysical Research*, v. 111, p. D21105.
- Phillips, W.M., Hall, A.M., Mottram, R., Fifield, L.K., and Sugden, D.E., 2006, Cosmogenic  $^{10}\text{Be}$  and  $^{26}\text{Al}$  exposure ages of tors and erratics, Cairngorm Mountains, Scotland: Timescales for the development of a classic landscape of selective linear glacial erosion: *Geomorphology*, v. 73, p. 222-245.
- Putkonen, J., and Swanson, T., 2003, Accuracy of cosmogenic ages for moraines: *Quaternary Research*, v. 59, p. 255-261.
- Raisbeck, G.M., Yiou, F., Jouzel, J., and Petit, J.R., 1990,  $^{10}\text{Be}$  and  $\delta^2\text{H}$  in polar ice cores as a probe of the solar variability influence on climate: *Philosophical Transactions of the Royal Society of London Series A*, v. 330, p. 463-470.

- Raisbeck, G.M., Yiou, F., Lieuvin, M., Ravel, J.C., Fruneau, M., and Loiseaux, J.M., 1981,  $^{10}\text{Be}$  in the environment: some recent results and their applications, *in* Henning, W., Ketchera, W., Smither, R.K., and Yntema, J.L., eds., Symposium on accelerator mass spectrometry: Argonne, Argonne National Lab, p. 228-243.
- Raynaud, D., Chappellaz, J., Ritz, C., and Martinerie, P., 1997, Air content along the Greenland Ice Core Project core: A record of surface climatic parameters and elevation in central Greenland: *Journal of Geophysical Research*, v. 102, p. 26607-26613.
- Rempel, A.W., 2008, A theory for ice-till interactions and sediment entrainment beneath glaciers: *Journal of Geophysical Research*, v. 113, p. F01013.
- Reusser, L.J., and Bierman, P.R., 2010, Using meteoric  $^{10}\text{Be}$  to track fluvial sand through the Waipaoa River Basin, New Zealand: *Geology*, v. 38, p. 47-50.
- Reusser, L.J., Graly, J.A., and Bierman, P.R., Submitted, A new approach for constraining long-term meteoric  $^{10}\text{Be}$  deposition rates: *Geophysical Research Letters*.
- Schiller, M., Dickinson, W., Ditchburn, R.G., Graham, I.J., and Zondervan, A., 2009, Atmospheric  $^{10}\text{Be}$  in an Antarctic soil: Implications for climate change: *Journal of Geophysical Research*, v. 114, p. F01033.
- Shen, C.D., Beer, J., Ivy-Ochs, S., Sun, Y., Yi, W., Kubik, P.W., Sutter, M., Li, Z., Peng, S., and Yang, Y., 2004a,  $^{10}\text{Be}$ ,  $^{14}\text{C}$  distribution, and soil production rate in a soil profile of a grassland slope at Heshan hilly land, Guangdong: *Radiocarbon*, v. 46.
- Shen, C.D., Beer, J., Kubik, P.W., Suter, M., Borkovec, M., and Liu, T.S., 2004b, Grain size distribution,  $^{10}\text{Be}$  content and magnetic susceptibility of micrometer-nanometer loess materials: *Nuclear Instruments and Methods in Physics Research B*, v. 223-224, p. 613-617.
- Socki, R.A., Karlsson, H.R., and Gibson, E.K., 1992, Extraction Technique of the Determination of Oxygen-18 In Water Preevacuated Glass Vials: *Analytical Chemistry*, v. 64, p. 829-831.
- Solomon, S., Qin, D., Manning, M., Marquis, M., Averyt, K., Tignor, M.M.B., Millier, H.L., and Chen, Z., 2007, *Climate Change 2007 the physical science basis*, Intergovernmental Panel on Climate Change.
- Somayajulu, B.L.K., Sharma, P., Beer, J., Bonani, G., Hofmann, H.J., Morezoni, E., Nessi, M., Suter, M., and Wölfli, W., 1984,  $^{10}\text{Be}$  annual fallout in rains in India: *Nuclear Instruments and Methods in Physics Research B*, v. 5, p. 398-403.
- Stanford, S.D., Seidl, M.A., and Ashley, G.M., 2000, Exposure age and erosional history of an upland planation surface in the US Atlantic Piedmont: *Earth Surface Processes and Landforms*, v. 25, p. 939-950.
- Steig, E.J., Polissar, P.J., Stuiver, M., Grootes, P.M., and Finkel, R.C., 1996, Large amplitude modulation cycles of  $^{10}\text{Be}$  in Antarctica: implications for atmospheric mixing processes and interpretation of the ice core record: *Geophysical Research Letters*, v. 23, p. 523-526.
- Stone, J., 1998, A rapid method for separation of beryllium-10 from soils and silicates: *Geochimica et Cosmochimica Acta*, v. 62, p. 555-561.

- Stroeven, A.P., Fabel, D., Harbor, J., Hätterstrand, C., and Kleman, J., 2002, Quantifying the erosional impact of the Fennoscandian ice sheet in the Torneträsk-Narvik corridor, northern Sweden, based on cosmogenic radionuclide data: *Geografiska Annaler*, v. 84 A, p. 275-287.
- Stuiver, M., and Grootes, P.M., 2000, GISP2 Oxygen Isotope Ratios: Quaternary Research, v. 53, p. 277-284.
- Sugden, D.E., P. G. Knight, Livesey, N., Lorrain, R.D., Souchez, R.A., Tison, J.L., and Jouzel, J., 1987, Evidence for two zones of debris entrainment beneath the Greenland Ice Sheet: *Nature*, v. 328, p. 238-241.
- Suwa, M., von Fischer, J.C., Bender, M.L., Landais, A., and Brook, E.J., 2006, Chronology reconstruction for the disturbed bottom section of the GISP2 and the GRIP ice cores: Implications for Termination II in Greenland: *Journal of Geophysical Research*, v. 111, p. D02101.
- Takahashi, Y., Minai, Y., Ambe, S., Makide, Y., and Ambe, F., 1999, Comparison of adsorption behavior of multiple inorganic ions on kaolinite and silica in the presence of humic acid using the multitracer technique: *Geochimica et Cosmochimica Acta*, v. 63, p. 815-836.
- Tarasov, L., and Peltier, W.R., 2003, Greenland glacial history, borehole constraints, and Eemian extent: *Journal of Geophysical Research*, v. 108.
- Thomason, J.F., and Iverson, N.R., 2008, A laboratory study of particle ploughing and pore-pressure feedback: a velocity-weakening mechanism for soft glacier beds: *Journal of Glaciology*, v. 54, p. 169-181.
- Tsai, H., Maejima, Y., and Hseu, Z.-Y., 2008, Meteoric  $^{10}\text{Be}$  dating of highly weathered soils from fluvial terraces in Taiwan: *Quaternary International*, v. 188, p. 185-196.
- Tulaczyk, S.M., Scherer, R.P., and Clark, C.D., 2001, A ploughing model for the origin of weak tills beneath ice streams: a qualitative treatment: *Quaternary International*, v. 86, p. 59-70.
- Usoskin, I.G., Alanko-Huotari, K., Kovaltsov, G.A., and Mursula, K., 2005, Heliospheric modulation of cosmic rays: Monthly reconstruction for 1951-2004: *Journal of Geophysical Research*, v. 110, p. A12108.
- Valero-Garcés, B.L., Laird, K.R., Fritz, S.C., Kelts, K., Ito, E., and Grimm, E.C., 1997, Holocene climate in the Northern Great Plains inferred from sediment stratigraphy, stable isotopes, carbonate geochemistry, diatoms, and pollen at Moon Lake, North Dakota: *Quaternary Research*, v. 48, p. 359-369.
- Valette-Silver, J.N., Tera, F., Klein, J., and Middleton, R., 1986,  $^{10}\text{Be}$  in geothermal systems: *Geothermal Resources Council, Transactions*, v. 10, p. 161-166.
- Vezina, J., Jones, B., and Ford, D., 1999, Sea-level highstands over the last 500,000 years: Evidence from the Ironshore formation on Grand Cayman, British West Indies: *Journal of Sedimentary Research*, v. 69, p. 317-327.
- Vidic, N.S., 1994, Pedogenesis and soil-age relationships of soils on glacial outwash terraces in the Ljubljana basin, University of Colorado.
- Vogt, P.R., Perry, R.K., Feden, R.H., Fleming, H.S., and Cherkis, N.Z., 1981, The Greenland - Norwegian Sea and Iceland environment: geology and geophysics, *in*

- Narin, A.E.M., Churkin, M., and Stehli, F.G., eds., *The ocean basins and margins Vol. 5 The Arctic Ocean*: New York, Plenum, p. 493-598.
- Walder, J.S., and Fowler, A., 1994, Channelized subglacial drainage over a deformable bed: *Journal of Glaciology*, v. 40, p. 3-15.
- Walling, D.E., and He, Q., 1999, Improved models for estimating erosion rates from Cesium-137 measurements: *Journal of Environmental Quality*, v. 28, p. 611-622.
- Wang, W.L., and Warner, R.C., 1999, Modelling of anisotropic ice flow in Law Dome, East Antarctica.
- Wang, W.L., Zwally, H.J., Abdalati, W., and Luo, S., 2002, Modeling of ice flow and internal layers along a flowline through Swiss Camp, West Greenland: *Annals of Glaciology*, v. 34, p. 303-308.
- Webber, W.R., Higgie, P.R., and McCracken, K.G., 2007, Production of the cosmogenic isotopes  $^3\text{H}$ ,  $^7\text{Be}$ ,  $^{10}\text{Be}$ , and  $^{36}\text{Cl}$  in the Earth's atmosphere by solar and galactic cosmic rays: *Journal of Geophysical Research*, v. 112, p. A10106.
- Weertman, J., 1957, On the sliding of glaciers: *Journal of Glaciology*, v. 3, p. 33-38.
- Weidick, A., Oerter, H., Reeh, N., Thomsen, H.H., and Thorning, L., 1990, The recession of the Inland Ice margin during the Holocene climatic optimum in Jakobshavn Isfjord area of West Greenland: *Palaeogeography, Palaeoclimatology, Palaeoecology*, v. 82, p. 389-399.
- White, W.A., 1988, More on deep erosion by continental ice sheets and their tongues of distributary ice: *Quaternary Research*, v. 30, p. 137-150.
- Willenbring, J.K., and von Blanckenburg, F., 2010, Meteoric cosmogenic Beryllium-10 adsorbed to river sediment and soil: applications for Earth-surface dynamics: *Earth Science Reviews*, v. 98, p. 105-122.
- Willerslev, E., Cappellini, E., Boomsma, W., Rasmus, N., Hebsgaard, M.B., Brand, T.B., Hofreiter, M., Bunce, M., Poinar, H.N., Dahl-Jensen, D., Johnsen, S., Steffensen, J.P., Bennike, O., Schwenninger, J.-L., Nathan, R., Armitage, S., de Hoog, C.-J., Alfimov, V., Christl, M., Beer, J., Muscheler, R., Barker, J., Sharp, M., Penkman, K.E.H., Haile, J., Taberlet, P., Gilbert, M.T.P., Casoli, A., Campani, E., and Collins, M.J., 2007, Ancient biomolecules from deep ice cores reveal a forested southern Greenland: *Science*, v. 317, p. 112-116.
- Yiou, F., Raisbeck, G.M., Baumgartner, S., Beer, J., Hammer, C., Johnsen, S., Jouzel, J., Kubik, P.W., Lestringuez, J., Stievenard, M., Suter, M., and Yiou, P., 1997, Beryllium 10 in the Greenland Ice Core Project ice core at Summit, Greenland: *Journal of Geophysical Research*, v. 102, p. 26783-26794.
- You, C.-F., Lee, T., Brown, L., Shen, J.J., and Chen, J.-C., 1988,  $^{10}\text{Be}$  study of rapid erosion in Taiwan: *Geochimica et Cosmochimica Acta*, v. 52, p. 2687-2691.
- You, C.-F., Lee, T., and Li, Y.-H., 1989, The partition of Be between soil and water: *Chemical Geology*, v. 77, p. 105-118.
- Young, N., Briner, J., Axford, Y., Rood, D., Finkel, R., and Csatho, B., 2010, The Holocene history of Jakobshavn Isbrae inferred from  $^{10}\text{Be}$  surface exposure ages and lake sediments, Arctic Workshop.
- Zanis, P., Gerasopoulos, E., Priller, A., Schnabel, C., Stohl, A., Zerefos, C., Gäggeler, H.W., Tobler, L., Kubik, P.W., Kanter, H.J., Scheel, H.E., Luterbacher, J., and

- Berger, M., 2003, An estimate of the impact of stratosphere-to-troposphere transport (STT) on the lower free troposphere ozone over the Alps using  $^{10}\text{Be}$  and  $^7\text{Be}$  measurements: *Journal of Geophysical Research*, v. 108, p. 8520.
- Zhou, W., Priller, A., Beck, J.W., Zhengkun, W., Maobai, C., Zhisheng, A., Kutschera, W., Feng, X., Huagui, Y., and Lin, L., 2007, Disentangling geomagnetic and precipitation signals in an 80-kyr Chinese loess record of  $^{10}\text{Be}$ : *Radiocarbon*, v. 49, p. 139-160.
- Zwally, H.J., and Giovinetto, M.B., 2001, Balance mass flux and ice velocity across the equilibrium line in drainage systems of Greenland: *Journal of Geophysical Research*, v. 106, p. 33717-33728.